

**MUTUAL COUPLING COMPENSATION IN ARRAYS AND ITS  
IMPLEMENTATION ON SOFTWARE DEFINED RADIOS**

A DISSERTATION SUBMITTED TO  
THE GRADUATE SCHOOL OF  
ENGINEERING AND NATURAL SCIENCES  
OF ISTANBUL MEDIPOL UNIVERSITY  
IN PARTIAL FULFILLMENT OF THE REQUIREMENTS FOR  
THE DEGREE OF  
DOCTOR OF PHILOSOPHY  
IN  
ELECTRICAL, ELECTRONICS ENGINEERING AND CYBER SYSTEMS

By

Sana Khan

April, 2021

MUTUAL COUPLING COMPENSATION IN ARRAYS AND ITS  
IMPLEMENTATION ON SOFTWARE DEFINED RADIOS

By Sana Khan

5 April 2021

We certify that we have read this dissertation and that in our opinion it is fully adequate,  
in scope and in quality, as a dissertation for the degree of Doctor of Philosophy.

---

Prof. Dr. Ercümen Arvas (Advisor)

---

Assoc. Prof. Dr. Mehmet Kemal Özdemir (Co-Advisor)

---

Prof. Dr. Şehabeddin Taha İmeci

---

Prof. Dr. Selim Akyokuş

---

Prof. Dr. Cengiz Özzaim

---

Assoc. Prof. Dr. Hakan Doğan

Approved by the Graduate School of Engineering and Natural Sciences:

---

Assoc. Prof. Dr. Yasemin Yüksel Durmaz

Director of the Graduate School of Engineering and Natural Sciences



I hereby declare that all information in this document has been obtained and presented in accordance with the academic rules and ethical conduct. I also declare that, as required by these rules and conduct, I have fully cited and referenced all material and results that are not original to this work.

Signature :

Name, Surname: SANA KHAN

## ACKNOWLEDGEMENT

I begin by praising Allah swt for enabling me to achieve this milestone and for His countless bounties.

My profound gratitude to my advisor Prof. Dr. Ercümend Arvas whose mentorship, encouragement and support paved the way for my graduate studies at Istanbul Medipol University.

The inspiration and zeal of my co-advisor Dr. Mehmet Kemal Özdemir, that empowered me to work at the forefronts of modern day technology. I am grateful to both my mentors for providing me with an atmosphere where I could freely work and continue my reasearch experiments.

I am grateful to Burak Gökay, Secretary at IMU Engineering Department, for managing all the procurement relentlessly.

I am indebted to Prof. Dr. Talip Alp for the motivational talks and support that would revitalize and help me focus towards my goal.

The wonderful discussions with Dr. Zekâi Şen that would enable me to think in different realms.

My particular gratitude to Dr. Serhend Arvas for his mentorship and always ready to answer any question.

I am grateful to Dr. Hakan Doğan and Prof. Dr. Selim Akyokuş for taking out time and serving on my committee.

I would like to thank my parents for their unflinching support, encouragement and prayers without which this would never be possible. I am grateful to my siblings who were always there to buck me up, non stop prayers of my in-laws, and supporting friends.

Last but not the least, I would like to thank my husband, Hassan Sajjad, for being by my side and supporting me through thick and thin to realize this milestone.

Sana Khan  
April, 2021

# CONTENTS

	<u>Page</u>
<b>ACKNOWLEDGEMENT</b> .....	iv
<b>CONTENTS</b> .....	v
<b>LIST OF FIGURES</b> .....	vii
<b>LIST OF TABLES</b> .....	xii
<b>LIST OF SYMBOLS</b> .....	xiii
<b>ABBREVIATIONS</b> .....	xiv
<b>ÖZET</b> .....	xvi
<b>ABSTRACT</b> .....	xvii
<b>1. INTRODUCTION</b> .....	<b>1</b>
1.1. Problem Statement.....	2
1.2. Motivation .....	3
1.3. Contribution of this Thesis .....	5
1.4. Thesis Organization .....	6
<b>2. THEORETICAL PART</b> .....	<b>9</b>
2.1. Background .....	9
2.2. Algorithm I: Received Mutual Impedance Method (RMIM).....	11
2.2.1. Theoretical verification .....	12
2.2.2. Direction of Arrival Estimation .....	15
2.2.3. Simulation verification.....	17
2.2.4. Limitations.....	21
2.3. Algorithm II: Mutual Coupling Compensation in Receiving Antenna Ar- rays .....	21
2.3.1. Formulation.....	22
2.3.2. Numerical examples .....	25
2.3.3. Contribution .....	35
2.4. Algorithm III: A New Algorithm for Mutual Coupling Compensation for Receiving Antenna Arrays.....	36
<b>3. EXPERIMENTAL PART</b> .....	<b>38</b>
3.1. Algorithm I: An Experimental Study of DoA Estimation with Mutual Coupling Compensation.....	38
3.1.1. Experimental procedure.....	38
3.2. Algorithm II: Mutual Coupling Compensation in Receiving Arrays and Its Implementation on Software Defined Radios for DoA Estimation Ap- plication .....	43
3.2.1. Introduction.....	43
3.2.2. Proposed system design.....	44
3.2.3. Mutual impedance measurements .....	46
3.2.4. Experimental procedure: DoA estimation .....	51
3.3. Algorithm III: An Experimental Setup for Mutual Coupling Compensa- tion in Receiving Antenna Arrays using Xilinx® Zynq®-Based FPGA and an Analog Devices™ FCOMMS5 Radio for DoA Application .....	54
3.3.1. Introduction.....	54
3.3.2. Experimental setup.....	55
3.3.3. Experimental procedure.....	63

3.4.	Algorithm III: IEEE 802.11a SIMO End-to-End Transceiver Implementation on Xilinx® Zynq® FPGA and an Analog Devices™ FMCOMMS5 radio with Mutual Coupling Compensation for Spectral Efficiency Application .....	68
3.4.1.	Introduction.....	68
3.4.2.	SIMO End-to-End transceiver hardware design .....	68
3.4.3.	Mutual Coupling Compensation Algorithm .....	75
<b>4.</b>	<b>RESULTS AND DISCUSSION .....</b>	<b>76</b>
4.1.	Algorithm I: An Experimental Study of DoA Estimation with Mutual Coupling Compensation.....	76
4.1.1.	Experimental Results.....	76
4.1.2.	Conclusion.....	79
4.2.	Algorithm II: Mutual Coupling Compensation in Receiving Arrays and Its Implementation on Software Defined Radios for DoA Estimation Application .....	81
4.2.1.	Experimental Results.....	81
4.2.2.	Conclusion.....	84
4.3.	Algorithm III: An Experimental Setup for Mutual Coupling Compensation in Receiving Antenna Arrays using Xilinx® Zynq®-Based FPGA and an Analog Devices™ FMCOMMS5 Radio for DoA Application .....	85
4.3.1.	Experiment I: Comparison of directional and omni-directional arrays with $0.24\lambda$ spacing for mutual coupling compensation and DoA estimation .....	86
4.3.2.	Experiment II: A study on DoA estimation vs spacing for a commercial quasi yagi array.....	94
4.3.3.	Conclusion.....	100
4.4.	Algorithm III: IEEE 802.11a SIMO End-to-End Transceiver Implementation on Xilinx® Zynq® FPGA and an Analog Devices™ FMCOMMS5 radio with Mutual Coupling Compensation for Spectral Efficiency Application .....	101
4.4.1.	Experimental Results.....	101
4.4.2.	Received WLAN waveform for a ULA with spacing $d=0.24\lambda$ .....	101
4.4.3.	Comparison of optimally spaced vs. coupled spaced ULA .....	113
4.4.4.	Comparison of optimally spaced ULA at low RSSI.....	114
4.4.5.	Different Array Setup Types.....	115
4.4.6.	UCA .....	119
4.4.7.	Conclusion.....	122
<b>5.</b>	<b>CONCLUSION AND FUTURE WORK.....</b>	<b>123</b>
5.1.	Future Work.....	124
	<b>BIBLIOGRAPHY.....</b>	<b>126</b>
	<b>CURRICULUM VITAE.....</b>	<b>134</b>

## LIST OF FIGURES

<b>Figure 1.1:</b> Examples of antenna arrays <b>a)</b> base station, <b>b)</b> reconfigurable intelligent surfaces (RIS) [1], <b>c)</b> military radar. ....	<b>1</b>
<b>Figure 1.2:</b> Problem statement. ....	<b>3</b>
<b>Figure 1.3:</b> Structural flow of this thesis. ....	<b>3</b>
<b>Figure 1.4:</b> (a) Circular array of four thin wire antennas with length $\lambda/2$ . (b) top view of the system. ....	<b>4</b>
<b>Figure 1.5:</b> Theoretical pattern obtained using the classical pattern multiplication method and the original sources ( <i>solid</i> ), the true practical pattern obtained using the original sources ( <i>square-dashed</i> ), and the compensated pattern obtained using the compensated voltages ( <i>dashed-dotted</i> ). ....	<b>4</b>
<b>Figure 1.6:</b> Flowchart of a complete RF system design. ....	<b>5</b>
<b>Figure 1.7:</b> Organization of this thesis. ....	<b>7</b>
<b>Figure 2.1:</b> Scenario of a typical mutual coupling problem in receiving antenna arrays. ....	<b>12</b>
<b>Figure 2.2:</b> Classification of DoA estimation techniques. ....	<b>16</b>
<b>Figure 2.3:</b> Four element monopole ULA in FEKO with $l = 0.24\lambda$ , $l/a = 100$ , $Z_L = 50 \Omega$ at 2.4 GHz. The incident plane wave is shown from $\phi = -90^\circ$ to $90^\circ$ and $\theta = 90^\circ$ . ....	<b>17</b>
<b>Figure 2.4:</b> Spatial spectrum of the MUSIC algorithm for DoA detection of two coherent signals from $\phi_1 = 30^\circ$ , $\phi_2 = 57^\circ$ and $\theta = 90^\circ$ for four-element ULA with $d = 0.5\lambda$ . ....	<b>18</b>
<b>Figure 2.5:</b> Spatial spectrum of the MUSIC algorithm for DoA detection of two coherent signals from $\phi_1 = 30^\circ$ , $\phi_2 = 57^\circ$ and $\theta = 90^\circ$ for four-element ULA with $d = 0.25\lambda$ . ....	<b>19</b>
<b>Figure 2.6:</b> Spatial spectrum of the MUSIC algorithm for DoA detection of two coherent signals from $\phi_1 = 5^\circ$ , $\phi_2 = -11^\circ$ and $\theta = 90^\circ$ for four-element ULA with $d = 0.25\lambda$ . ....	<b>20</b>
<b>Figure 2.7:</b> 2D spatial spectrum of the MUSIC algorithm for DoA detection for an incident signal $\phi = 25^\circ$ and $\theta = 45^\circ$ for four-element ULA with $d = 0.25\lambda$ . ....	<b>20</b>
<b>Figure 2.8:</b> Problem statement. ....	<b>22</b>
<b>Figure 2.9:</b> Four element thin wire dipole array with $d = 0.2\lambda$ being excited by a plane wave with $\theta = 90^\circ$ and $\phi = 90^\circ$ . ....	<b>26</b>
<b>Figure 2.10:</b> Four element ULA of thin wire antennas with $d = 0.2\lambda$ under different plane-wave excitation. ....	<b>26</b>
<b>Figure 2.11:</b> Real part of the mutual impedance matrix for four element ULA with $d = 0.2\lambda$ , for all elevation angles. ....	<b>27</b>
<b>Figure 2.12:</b> Imaginary part of the mutual impedance matrix for four element ULA with $d = 0.2\lambda$ , for all elevation angles. ....	<b>27</b>
<b>Figure 2.13:</b> Received voltages for a four element ULA $\phi$ variation, $\theta = 90^\circ$ <b>a)</b> magnitude, <b>b)</b> phase, <b>c)</b> legend. ....	<b>30</b>
<b>Figure 2.14:</b> Received voltages for a four element ULA $\theta$ variation, $\phi = 90^\circ$ <b>a)</b> magnitude, <b>b)</b> phase, <b>c)</b> legend. ....	<b>31</b>
<b>Figure 2.15:</b> DoA estimation of two coherent sources for a fixed azimuth $\phi = 90^\circ$ and two different elevation angles, $\theta_1 = 45^\circ$ and $\theta_2 = 75^\circ$ . ....	<b>32</b>

<b>Figure 2.16:</b> Spatial spectrum of MUSIC algorithm for DoA detection of two coherent signals from $\phi = 90^\circ$ , $\theta_1 = 45^\circ$ , $\theta_2 = 75^\circ$ .	33
<b>Figure 2.17:</b> DoA estimation of two coherent sources for a fixed elevation $\theta = 90^\circ$ and two different azimuth angles, $\phi_1 = 45^\circ$ and $\phi_2 = 75^\circ$ .	33
<b>Figure 2.18:</b> Spatial spectrum of MUSIC algorithm for DoA detection of two coherent signals from $\theta = 90^\circ$ , $\phi_1 = 45^\circ$ , $\phi_2 = 75^\circ$ .	34
<b>Figure 2.19:</b> Four element UCA with radius $\lambda/8$ excited by two coherent sources from $\theta = 90^\circ$ and $\phi_1 = 35^\circ$ and $\phi_2 = 45^\circ$ .	34
<b>Figure 2.20:</b> Algorithm III general statement.	36
<b>Figure 3.1:</b> A seven-element monopole ULA <b>a)</b> designed and simulated in CST, <b>b)</b> fabricated isolated monopole and monopole array.	39
<b>Figure 3.2:</b> Measurement of a seven-element monopole array in an anechoic chamber under an external plane-wave using a horn antenna for DoA estimation.	40
<b>Figure 3.3:</b> The fabricated seven-element monopole ULA as proposed in	40
<b>Figure 3.4:</b> Measurement of an isolated monopole in an anechoic chamber under an external plane-wave using a horn antenna.	41
<b>Figure 3.5:</b> Multiple coherent source DoA estimation for seven-element monopole ULA.	41
<b>Figure 3.6:</b> Multiple coherent source DoA estimation for seven-element monopole ULA for different source separation.	42
<b>Figure 3.7:</b> Block diagram of DoA estimation system.	44
<b>Figure 3.8:</b> Initial experimental test-bed for DoA estimation (a) complete setup (b) zoomed in.	47
<b>Figure 3.9:</b> Final experimental mobile setup for DoA estimation (a) frontside (b) backside.	48
<b>Figure 3.10:</b> Setup for measuring the isolated voltages <b>a)</b> antenna 1, <b>b)</b> antenna 2, <b>c)</b> antenna 3, <b>d)</b> antenna 4.	49
<b>Figure 3.11:</b> Setup for measuring the coupled array voltages <b>a)</b> antenna 1, <b>b)</b> antenna 2, <b>c)</b> antenna 3, <b>d)</b> antenna 4.	50
<b>Figure 3.12:</b> The complete experimental setup for DoA estimation.	51
<b>Figure 3.13:</b> Receiver part of the experimental setup for DoA estimation.	52
<b>Figure 3.14:</b> Received signal amplitude after calibration.	53
<b>Figure 3.15:</b> Received signal. (a) before phase calibration (b) after phase calibration.	53
<b>Figure 3.16:</b> SDR <b>a)</b> Adalm-Pluto, <b>b)</b> block diagram.	55
<b>Figure 3.17:</b> Transmitting setup consisting of Pluto SDR and quasi yagi antenna.	56
<b>Figure 3.18:</b> DoA testing setup consisting of the transmitter placed on a semi-circle with angles from $-90^\circ$ to $+90^\circ$ with $5^\circ$ spacing and origin defined at $0^\circ$ .	58
<b>Figure 3.19:</b> The receiving setup consists of a four element quasi yagi array with $0.2479\lambda$ spacing connected to Xilinx Zynq ZC706 FPGA with Analog Devices FMCOMMS5 RFFE Module.	60
<b>Figure 3.20:</b> Xilinx Zynq ZC706 FPGA with Analog Devices FMCOMMS5 RFFE Module.	60
<b>Figure 3.21:</b> Setup for the initial calibration of the FMCOMMS5 SDR.	61
<b>Figure 3.22:</b> IIO Scope by Analog Devices showing the cross correlation of the receiving channels LO phase after calibration.	62
<b>Figure 3.23:</b> After phase calibration of the four channel receiver showing the IQ signals.	63



<b>Figure 3.24:</b> Received signal at $0^\circ$ showing the calibration being set at origin.....	<b>64</b>
<b>Figure 3.25:</b> Setup for measuring the isolated voltages for the quasi yagi antenna array.....	<b>64</b>
<b>Figure 3.26:</b> Comparison of the power pattern of a single quasi yagi antenna. ....	<b>65</b>
<b>Figure 3.27:</b> Comparison of measured and simulated power pattern of quasi yagi array for $d=0.5\lambda$ . ....	<b>66</b>
<b>Figure 3.28:</b> Comparison of power pattern of quasi yagi array for $0.57\lambda$ and $0.24\lambda$ spacings.....	<b>67</b>
<b>Figure 3.29:</b> IEEE 802.11a OFDM frame structure.....	<b>69</b>
<b>Figure 3.30:</b> Generated preamble of WLAN OFDM packet. ....	<b>70</b>
<b>Figure 3.31:</b> Generated Non-HT data format of WLAN OFDM packet. ....	<b>70</b>
<b>Figure 3.32:</b> Transmitted image using Pluto SDR. ....	<b>71</b>
<b>Figure 3.33:</b> Time and frequency domain representation of the transmitted image of the WLAN packets. ....	<b>72</b>
<b>Figure 3.34:</b> The receiving setup consists of a four-element Quasi Yagi array with $0.24\lambda$ spacing connected to Xilinx Zynq ZC706 FPGA with Analog Devices FMCOMMS5 RFFE Module. The transmitter is an ADALM-PLUTO SDR connected to a TPLink WiFi antenna. ....	<b>73</b>
<b>Figure 4.1:</b> Spatial spectrum of the MUSIC algorithm for DoA detection of a single source signal $\phi = 0^\circ$ and $\theta = 90^\circ$ for seven-element monopole ULA with $d = 0.2\lambda$ .....	<b>76</b>
<b>Figure 4.2:</b> Spatial spectrum of the MUSIC algorithm for DoA detection of a single source signal $\phi = 10^\circ$ and $\theta = 90^\circ$ for seven-element monopole ULA with $d = 0.2\lambda$ .....	<b>77</b>
<b>Figure 4.3:</b> Spatial spectrum of the MUSIC algorithm for DoA detection of a single source signal $\phi = 50^\circ$ and $\theta = 90^\circ$ for seven-element monopole ULA with $d = 0.2\lambda$ .....	<b>77</b>
<b>Figure 4.4:</b> Estimated DoA vs Actual DoA for $\theta = 90^\circ$ . DoA estimation for a four element ULA with $d=\lambda/2$ and $d=\lambda/4$ (with and without mutual coupling compensation). ....	<b>82</b>
<b>Figure 4.5:</b> DoA estimation for a four element ULA with $d = \lambda/2$ and $d = \lambda/4$ (with and without mutual coupling compensation). Spatial spectrum of MUSIC algorithm for DoA detection of signal from $\theta = 90^\circ$ , $\phi = 60^\circ$ . ....	<b>82</b>
<b>Figure 4.6:</b> Estimated DoA using Labview for the incident angle (a) $45^\circ$ for $d = \lambda/2$ in the presence of coupling (b) $60^\circ$ for $d=\lambda/4$ after compensation. ....	<b>83</b>
<b>Figure 4.7:</b> Omni-directional four element ULA using TPLink WiFi antennas with spacing $0.24\lambda$ with a directional antenna as transmitter. ....	<b>85</b>
<b>Figure 4.8:</b> Received coupled (top) , compensated (center) and isolated (bottom) voltages for quasi yagi array from $\phi = 40^\circ$ . ....	<b>86</b>
<b>Figure 4.9:</b> Magnitude and phase of received coupled (top) , compensated (center) and isolated (bottom) voltages for quasi yagi array from $\phi = 40^\circ$ . .	<b>87</b>
<b>Figure 4.10:</b> Spectrum of coupled (top) and compensated (bottom) received signal for quasi yagi array from $\phi = 40^\circ$ . ....	<b>88</b>
<b>Figure 4.11:</b> Real time DoA estimation App showing results for four element quasi yagi array with $0.24\lambda$ spacing with incident angle from $\phi = 40^\circ$ . ....	<b>89</b>
<b>Figure 4.12:</b> Received Coupled (top), Compensated (center) and Isolated (bottom) voltages for TPLink dipole array from $\phi = -20^\circ$ . ....	<b>90</b>

<b>Figure 4.13:</b> Magnitude and phase of received coupled (top), compensated (center) and isolated (bottom) voltages for TPLink dipole array from $\phi = -20^\circ$ .	<b>91</b>
<b>Figure 4.14:</b> Spectrum of coupled (top) and compensated (bottom) received signal for TPLink dipole array from $\phi = -20^\circ$ .	<b>92</b>
<b>Figure 4.15:</b> Real time DoA estimation App showing results for four element TPLink dipole array with $0.24\lambda$ spacing with incident angle from $\phi = -20^\circ$ .	<b>93</b>
<b>Figure 4.16:</b> Real time DoA estimation App showing results for four element TPLink dipole array with $0.24\lambda$ spacing with incident angle from $\phi = -40^\circ$ .	<b>93</b>
<b>Figure 4.17:</b> Real time DoA estimation App showing results for four element quasi yagi array with $0.24\lambda$ spacing with incident angle from $\phi = 20^\circ$ .	<b>94</b>
<b>Figure 4.18:</b> A commercial quasi yagi ULA of four-elements with different spacing.	<b>95</b>
<b>Figure 4.19:</b> A commercial quasi yagi array for estimating DoA for different spacings.	<b>96</b>
<b>Figure 4.20:</b> Estimated DoA in the presence of coupling for 3 different spacings $0.6\lambda$ , $0.5\lambda$ and $0.4\lambda$ for commercial quasi yagi ULA.	<b>97</b>
<b>Figure 4.21:</b> Error plot for estimated DoA in the presence of coupling for 3 different spacings $0.6\lambda$ , $0.5\lambda$ and $0.4\lambda$ for quasi yagi array.	<b>97</b>
<b>Figure 4.22:</b> Estimated DoA in the presence of coupling for two different spacings $0.24\lambda$ and $0.57\lambda$ for TPLink dipole array.	<b>98</b>
<b>Figure 4.23:</b> Estimated DoA in the presence of coupling for two different spacings $0.24\lambda$ and $0.57\lambda$ for printed quasi yagi array.	<b>99</b>
<b>Figure 4.24:</b> Received WLAN packet in the presence of coupling for four-element Quasi Yagi ULA with spacing $d=0.24\lambda$ .	<b>102</b>
<b>Figure 4.25:</b> Received WLAN packet after compensation for four-element Quasi Yagi ULA with spacing $d=0.24\lambda$ .	<b>102</b>
<b>Figure 4.26:</b> SNR comparison of received coupled and compensated WLAN packets.	<b>104</b>
<b>Figure 4.27:</b> PER comparison of received coupled and compensated WLAN packets.	<b>105</b>
<b>Figure 4.28:</b> Received decoded Image <b>a)</b> after compensation, <b>b)</b> in presence of coupling.	<b>106</b>
<b>Figure 4.29:</b> EVM vs subcarriers comparison of received coupled and compensated WLAN packets.	<b>107</b>
<b>Figure 4.30:</b> EVM vs symbols comparison of received coupled and compensated WLAN packets.	<b>108</b>
<b>Figure 4.31:</b> Channel capacity comparison of received coupled and compensated WLAN packets.	<b>109</b>
<b>Figure 4.32:</b> Theoretical channel capacity for SISO, MISO, SIMO and MIMO systems.	<b>109</b>
<b>Figure 4.33:</b> Time domain burst of received packet no. 33: <b>a)</b> coupled, <b>b)</b> compensated.	<b>110</b>
<b>Figure 4.34:</b> Power spectrum of received packet no. 33: <b>(a)</b> coupled, <b>(b)</b> compensated.	<b>111</b>
<b>Figure 4.35:</b> Constellation of received packet no. 33: <b>a)</b> coupled, <b>b)</b> compensated.	<b>112</b>
<b>Figure 4.36:</b> Comparison of received images <b>a)</b> compensated case, <b>b)</b> coupled case for $d = 0.5\lambda$ ULA with low RSSI.	<b>114</b>

<b>Figure 4.37:</b> Different antenna arrays used for this experiment <b>a)</b> fractal antennas at $f=1$ GHz and $d = 0.33\lambda$ , <b>b)</b> vivaldi antennas at $f=3.7$ GHz and $d = 0.28\lambda$ , <b>c)</b> circular patch antennas at $f=4.55$ GHz and $d = 0.37\lambda$ , <b>d)</b> wideband vivaldi antenna at $f=5.95$ GHz and $d = 0.4\lambda$ ULA.....	<b>117</b>
<b>Figure 4.38:</b> Different transmitting antennas used for this experiment <b>a)</b> log periodic, <b>b)</b> tear drop, <b>c)</b> vivaldi. ....	<b>118</b>
<b>Figure 4.39:</b> UCA of quasi yagi antennas arranged at radius $\lambda/4$ <b>a)</b> top view, <b>b)</b> bottom view, <b>c)</b> complete setup.....	<b>120</b>
<b>Figure 4.40:</b> Received signal for an IEEE 802.11a SIMO transceiver implementation for a UCA of quasi yagi antennas arranged at radius $\lambda/4$ . (a) in presence of coupling, (b) after compensation. ....	<b>121</b>



## LIST OF TABLES

<b>Table 2.1:</b> Received mutual impedance for a four element ULA. ....	<b>28</b>
<b>Table 2.2:</b> Received mutual impedance for a four element UCA. ....	<b>35</b>
<b>Table 2.3:</b> Isolated, coupled and compensated voltages for a four element UCA. ....	<b>35</b>
<b>Table 3.1:</b> Setup details for experimental test-bed for DoA application. ....	<b>45</b>
<b>Table 3.2:</b> System specifications for the transmitter. ....	<b>57</b>
<b>Table 3.3:</b> System specifications for the receiver. ....	<b>59</b>
<b>Table 3.4:</b> System specifications for SIMO transceiver system. ....	<b>74</b>
<b>Table 4.1:</b> Measured results for DoA estimation of a single source using a seven-element monopole array in an anechoic chamber. ....	<b>78</b>
<b>Table 4.2:</b> Measured results for DoA estimation of multiple coherent sources using a seven-element monopole array in an anechoic chamber. ....	<b>79</b>
<b>Table 4.3:</b> System specifications for the receiver array for study of DoA vs. different antenna spacing. ....	<b>99</b>
<b>Table 4.4:</b> Comparison of $d = 0.5\lambda$ and $d = 0.24\lambda$ spaced ULA in presence of coupling with Tx power $-15$ dB. ....	<b>113</b>
<b>Table 4.5:</b> Comparison of $d = 0.5\lambda$ ULA with low RSSI and Tx power $-20$ dB. ....	<b>115</b>

## LIST OF SYMBOLS

$\theta$	:Elevation angle in degrees
$\phi_i$	:Incident Azimuth angle in degrees
$d$	:Inter-element spacing between antennas
$\lambda$	:Free-space wavelength
$B$	:Bandwidth
$(\cdot)^T$	:Transpose
$\sigma$	:Noise standard deviation
$V_c$	:Received coupled voltage
$S_i$	:Received isolated voltage
$Z$	:Received mutual impedance matrix
$Z_L$	:Load impedance
$C$	:Induced coupled voltage
$N$	:Number of antennas
$P$	:Number of incident azimuth angles
$V_c$	:Coupled voltage
$a$	:Radius
$l$	:Electrical length

## ABBREVIATIONS

<b>1-D</b>	: One Dimensional
<b>2-D</b>	: Two Dimensional
<b>3-D</b>	: Three Dimensional
<b>ADC</b>	: Analog to Digital Converter
<b>AGC</b>	: Automatic Gain Control
<b>AM</b>	: Amplitude Modulation
<b>BCC</b>	: Binary Convolutional Code
<b>BPSK</b>	: Binary Phase Shift Keying
<b>BS</b>	: Base Station
<b>CRC</b>	: Cyclic Redundancy Check
<b>DoA</b>	: Direction of Arrival
<b>EM</b>	: Electromagnetic
<b>ESPRIT</b>	: Estimation of Signal Parameters via Rotational Invariant Techniques
<b>EVM</b>	: Error Vector Magnitude
<b>EW</b>	: Electronic Warfare
<b>FDTD</b>	: Finite Difference Time Domain
<b>FPGA</b>	: Field Programmable Gate Array
<b>GPSDO</b>	: GPS Disciplined Oscillator
<b>GbE</b>	: Gigabit Ethernet
<b>HD</b>	: High Definition
<b>HT</b>	: High Throughput
<b>IMU</b>	: Istanbul Medipol University
<b>IRR</b>	: Image Rejection Ratio
<b>L-LTF</b>	: Legacy Long Training Field
<b>L-STF</b>	: Legacy Short Training Field
<b>LLS</b>	: LO Leakage Suppression
<b>LNA</b>	: Low Noise Amplifier
<b>LOS</b>	: Line of Sight
<b>MAC</b>	: Media Access Control
<b>MCC</b>	: Mutual Coupling Compensation
<b>MCS</b>	: Multiple Chip Synchronization
<b>MC</b>	: Mutual Coupling
<b>MIMO</b>	: Multiple Input Multiple Output
<b>MPDU</b>	: MAC Protocol Data Unit
<b>MSDU</b>	: MAC Service Data Unit
<b>MSPS</b>	: Mega Samples Per Second
<b>MUSIC</b>	: Multiple Signal Classification
<b>MVDR</b>	: Minimum Variance Distortionless Response
<b>MoM</b>	: Method of Moments
<b>OFDM</b>	: Orthogonal Frequency Division Multiplexing
<b>PAPR</b>	: Peak to Average Power Ratio
<b>PER</b>	: Packet Error Rate
<b>PHY</b>	: Physical Layer
<b>PLCP</b>	: Physical Layer Convergence Protocol

<b>PL</b>	: Programmable Logic
<b>PPDU</b>	: Physical Layer Protocol Data Unit
<b>PPS</b>	: Pulse Per Second
<b>PSDU</b>	: PLCP Service Data Unit
<b>PSD</b>	: Power Spectral Density
<b>PS</b>	: Processing System
<b>QAM</b>	: Quadrature Amplitude Modulation
<b>RFFE</b>	: Radio Frequency Front End
<b>Rx</b>	: Receiver
<b>SA</b>	: Spectrum Analyzer
<b>SDR</b>	: Software Defined Radio
<b>SIMO</b>	: Single Input Single Output
<b>SNR</b>	: Signal to Noise Ratio
<b>SSB-SC</b>	: Single-SideBand Suppressed-Carrier Modulation
<b>Tx</b>	: Transmitter
<b>UCA</b>	: Uniform Circular Array
<b>ULA</b>	: Uniform Linear Array
<b>USRP</b>	: Universal Software Radio Peripheral
<b>VNA</b>	: Vector Network Analyzer

# DİZİLERDE KARŞILIKLI KUPLAJ KOMPANZASYONU VE YAZILIM TABANLI TELSİZLERDEKİ UYGULAMASI

## ÖZET

Sana Khan

Elektrik-Elektronik Mühendisliği ve Siber Sistemler, Doktora

Tez Danışmanı: Prof. Dr. Ercümend Arvas

Nisan, 2021

Anten dizilerinde karşılıklı kuplaj, on yıllardır araştırılan klasik bir sorundur. Bu tez, SDR'leri kullanarak anten dizilerini almak için iki farklı test yatağı geliştirilerek deneysel doğrulamalarıyla birlikte iki farklı algoritma sunar. Anten dizileri izotropik veya çok yönlü olabilir ve ULA, UCA'da düzenlenebilir veya herhangi bir geometriye genişletilebilir. DoA'nın etkisi,  $0.24\lambda$  ile  $0.6\lambda$  arasında değişen aralık değerleriyle ve gerçek zamanlı karşılıklı kuplaj telafisi ile ULA için incelendi. Sonuçlar, DoA'nın kuplaj kaldırıldıktan sonra yankısız bir oda kullanılmadan, kapalı bir ortamda çevrimiçi veya çevrimdışı yöntemlerle hesaplanabilen bir dekuplaj matrisi kullanılarak tam doğrulukla tahmin edilebileceğini gösterdi. Kuplajın veri hızlarındaki etkisini gerçek zamanlı olarak incelemek için, Zynq Radio ve Xilinx FPGA kullanılarak SIMO alıcı-verici için bir IEEE 802.11a standardı uygulandı. Verici, 802.11a standardını kullanarak bir HD resim gönderir ve alıcı karşılıklı kuplaj varlığında verilerin kodunu zamandan kompanzasyonundan sonra çözer. SNR, PER, EVM, kanal kapasitesi gibi performans ölçümleri, karşılıklı kuplajın etkilerinin hem zaman hem de frekans alanındaki kompanzasyonu ile birlikte görselleştirilmesiyle analiz edilir. Sonuçlar, düşük RSSI'da alınan sinyalin kompanzasyon sonrasında 10 dB SNR kazancına ve kanal kapasitesinde 4 bps / Hz artışa sahip olabileceğini göstermektedir. Dekuplaj matrisi için kapalı form denklemini kullanan matematiksel bir model, ULA ve UCA geometrileri için geliştirilmiştir ve dizideki anten tipine bakılmaksızın önceden hesaplanabilen keyfi geometrilere kolaylıkla genişletilebilir. Hesaplama karmaşıklığı yalnızca tek bir matris çarpımıdır. Ayrıca, algoritma olumlu sonuçların elde edildiği iletim durumunda da test edilmiştir.

Anahtar sözcükler: Anten Dizileri, Varış Yönü, Karşılıklı Kuplaj, Yazılım Tabanlı Telsizler, ULA, UCA, Momentler Yöntemi.



# MUTUAL COUPLING COMPENSATION IN ARRAYS AND ITS IMPLEMENTATION ON SOFTWARE DEFINED RADIOS

## ABSTRACT

Sana Khan

Ph.D. in Electrical, Electronics Engineering and Cyber Systems

Advisor: Prof. Dr. Ercümend Arvas

April, 2021

Mutual coupling in antenna arrays is a classical problem that has been researched for several decades. This thesis presents two different algorithms along with their experimental verification by developing two different test beds for mutual coupling compensation in receiving antenna arrays using SDRs. The antenna arrays can be directional or omnidirectional and arranged in ULA, UCA or extended to arbitrary geometry. The effect of DoA with spacing was studied for ULA with spacing varied from  $0.24\lambda$  to  $0.6\lambda$  with real-time coupling compensation. The results showed that DoA can be estimated with full accuracy in an indoor environment without the use of an anechoic chamber after compensation using a decoupling matrix which can be calculated by online or offline methods. In order to study the effect of coupling in real-time on data rates, an IEEE 802.11a standard was implemented for SIMO end-to-end transceiver using Zynq Radio and Xilinx FPGA. The transmitter sends an HD picture using the 802.11a standard and the receiver decodes the data in the presence of mutual coupling and after compensation in real-time. The performance metrics like SNR, PER, EVM, channel capacity are analyzed along with visualization of effects of mutual coupling and its compensation in both time and frequency domain. The results show that at low RSSI the received signal can have a 10 dB SNR gain after compensation and an increase of 4 bps/Hz in channel capacity. A mathematical model using a closed-form equation for the decoupling matrix has been developed for ULA and UCA geometries and can be easily extended to arbitrary geometries which can be precalculated irrespective of the antenna type in the array. The computational complexity is only a single matrix multiplication. Furthermore, the algorithm was also tested in the transmitting case where favourable results have been achieved.

Keywords: Antenna Arrays, Direction of Arrival, Mutual Coupling, Software Defined Radios, ULA, UCA, Method of Moments.

## CHAPTER 1

### 1. INTRODUCTION

Antenna arrays are indispensable when we talk about wireless communication systems. In fact, the first block of such a system always begins with an antenna in the transmit or receive chain. In modern day technology, phased arrays are the most important type of arrays that are deployed in various fronts such as Electronic Warfare (EW), Multiple Input Multiple Output (MIMO) Base Stations (BS) for 5G, MIMO radars, WiFi 6 deploying (Multi User) MU-MIMO, Military Radars, Satellite Communications (SatCom) etc. Some examples of antenna arrays can be seen in **Figure 1.1**.

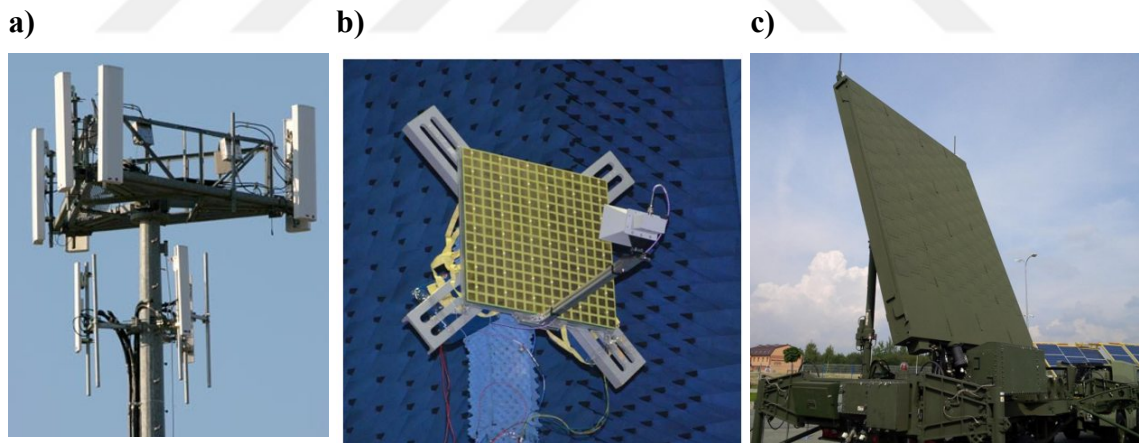


**Figure 1.1:** Examples of antenna arrays **a)** base station, **b)** reconfigurable intelligent surfaces (RIS) [1], **c)** military radar.

The advantage of using an array over a single antenna, results in high gain, high SNR, enhanced directivity, beam steering capability and spatial diversity. The size of an array is limited by the spacing between the antenna elements in the array. In order to design compact arrays, the need arises to decrease the spacing between the antenna elements. As an example, WiFi 6 based on IEEE 802.11ax protocol is expected to give 40% speed

increase with better performance in congested WiFi environments as compared to the current WiFi 5 (802.11ac). However, a major challenge is the RF system design due to the increasing number of antennas being incorporated in the Access Point (AP). This new MU-MIMO technology covers dual bands of 2.4 GHz and 5 GHz which requires upto 8 antennas for effective functionality on both uplink and downlink spatial streams. These 8 antennas can be embedded or external however due to the limited space the antennas need to be optimized to limit the interference or mutual coupling. Thus minimization of the antenna pattern correlation is a major challenge for small portable APs for successful WiFi 6 performance [2]. Mutual Coupling (MC) is a classical electromagnetic problem which effects the transmit and received signals in antennas if they are in an array or close to another antenna's near field. This EM interaction changes the current magnitude and phase on each of the antenna elements from their free space values. Due to the alteration in the radiation pattern, the gain, bandwidth and impedance of the antenna is effected which ultimately degrades the array performance. Although there are some cases where MC has been used as an advantage [3]–[6], but in majority cases there is a negative effect of MC. The optimal spacing of half a wavelength is the norm for majority of phased array systems by compromising with the affects of MC. Since our goal is to design compact array systems, going beyond this optimum spacing is of no use. However, if we go below this spacing, we suffer from high MC. In order to tackle this real-world challenge, it is imperative to come up with a Mutual Coupling Compensation (MCC) technique for both transmitting and receiving antenna arrays.

### **1.1. Problem Statement**

MCC can be broadly divided into two main categories as shown in **Figure 1.2**. In this thesis, we first verify the theory and develop an algorithm using numerical methods and EM simulations to compensate for the mutual coupling in receiving antenna arrays. The second part is the implementation of the developed algorithm by designing an experimental setup using Software Designed Radios (SDRs) to show the effect of MC as well as real time compensation. The structural flow of the thesis is shown in **Figure 1.3**.

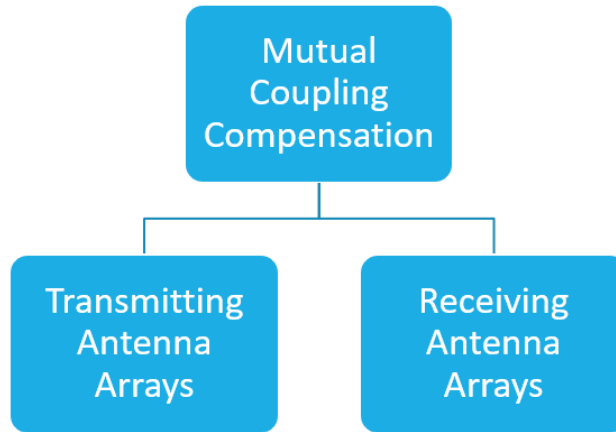


**Figure 1.2:** Problem statement.



**Figure 1.3:** Structural flow of this thesis.

## 1.2. Motivation

Consider a circular array of thin wire dipoles as shown in **Figure 1.4**. Assume that the antennas are excited with unit magnitude and phase progression of  $30^\circ$ . Given the excitation voltages, we can predict the radiation pattern of this array using array factor method. We call this the theoretical pattern. However, when we run an EM simulation for the same array with the same excitation voltages, we observe a totally different radiation pattern. This is called the practical pattern. The motivation of this thesis is to transform this practical pattern back to the theoretical pattern. This is called the compensated pattern. **Figure 1.5** shows the the three patterns respectively. Since theoretical pattern does not include MC therefore this is the solution we want to achieve. The real world includes MC and this is manifested by the practical pattern. After compensation of MC, we expect a pattern similar to the theoretical pattern which is shown by the compensated pattern [7].

In the above example we observed that MC is a notorious problem which is manifested both in transmitting and receiving antenna arrays. It is a real world problem that needs to be addressed. Understanding a problem and then developing its theory and then verifying it via simulations is one major contribution. But experimental verification and designing

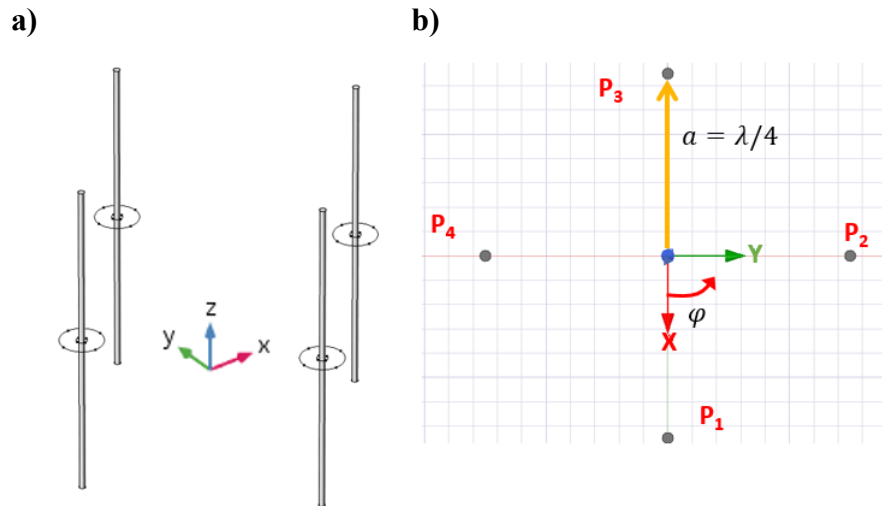


**Figure 1.4:** (a) Circular array of four thin wire antennas with length  $\lambda/2$ . (b) top view of the system.

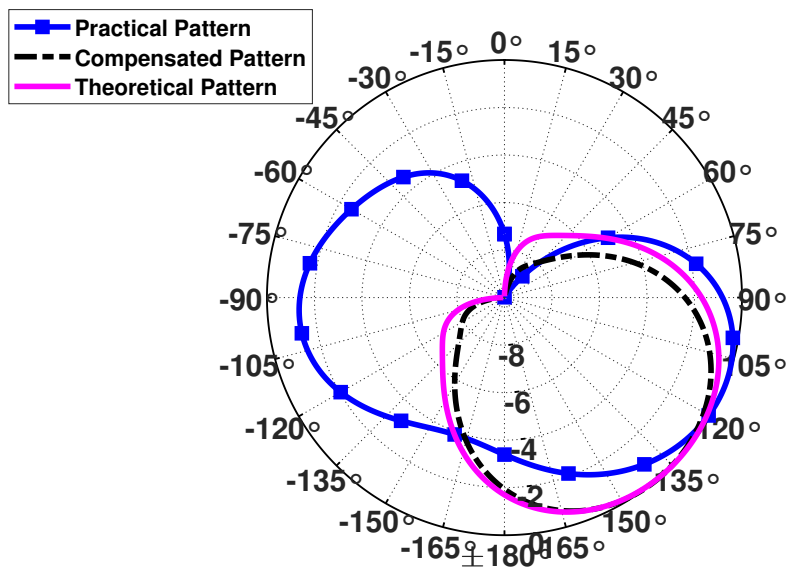


**Figure 1.5:** Theoretical pattern obtained using the classical pattern multiplication method and the original sources (*solid*), the true practical pattern obtained using the original sources (*square-dashed*), and the compensated pattern obtained using the compensated voltages (*dashed-dotted*).

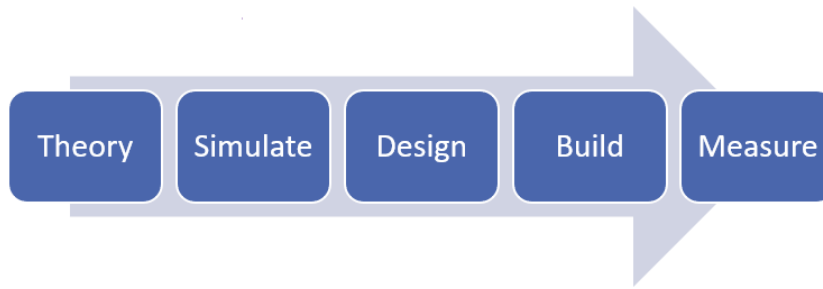


**Figure 1.6:** Flowchart of a complete RF system design.

a stand-alone system completes the entire scientific process. The complete system design process can be depicted in **Figure 1.6**.

Hence, the motivation for this thesis is to develop a system that verifies the theory developed above.

### **1.3. Contribution Of This Thesis**

This is an experimental thesis which provides an insight in dealing with MC effects due to different antenna types (directional or omni-directional) and when they are arranged in different configurations (Uniform Linear Array (ULA) and Uniform Circular Array (UCA) and can be easily extended to arbitrary geometries). Two different experimental test-beds and two different algorithms were devised in order to verify MCC in real-time. Different applications were demonstrated like DoA and effect of MC on data rates and channel capacity. A mathematical model has been developed to calculate the coupling matrices offline or online which reduces the complexity to a single matrix multiplication. There are many techniques for MCC that were developed in the past decade but all of them require tedious measurements and high computational complexity. The technique developed in this thesis provides real-time MCC with least measurements and the ability to precalculate the decoupling matrix with minimum complexity that can be implemented easily on any digital receiver.

## 1.4. Thesis Organization

The organization of this thesis can be explained using **Figure 1.7**. The problem of MCC in receiving antenna arrays can be broadly divided under three categories of theoretical verification, simulation verification and experimental verification. Three different algorithms are discussed under each of the above categories. Algorithm I is already available in the literature and a detailed study of this algorithm and its underlying limitations are discussed by performing the simulation and experimental verification. After modifying Algorithm I, we derive Algorithm II and again we verify the simulation results and then design an experimental test-bed based on SDRs to test the algorithm using Direction of Arrival (DoA) as an application. Finally, we develop Algorithm III, which is based on a new approach and a different hardware setup is realized to test the algorithm using two different applications namely DoA and IEEE 802.11a SIMO end-to-end transceiver implementation on a Xilinx® Zynq® FPGA and an Analog Devices™ FMCOMMS5 radio.

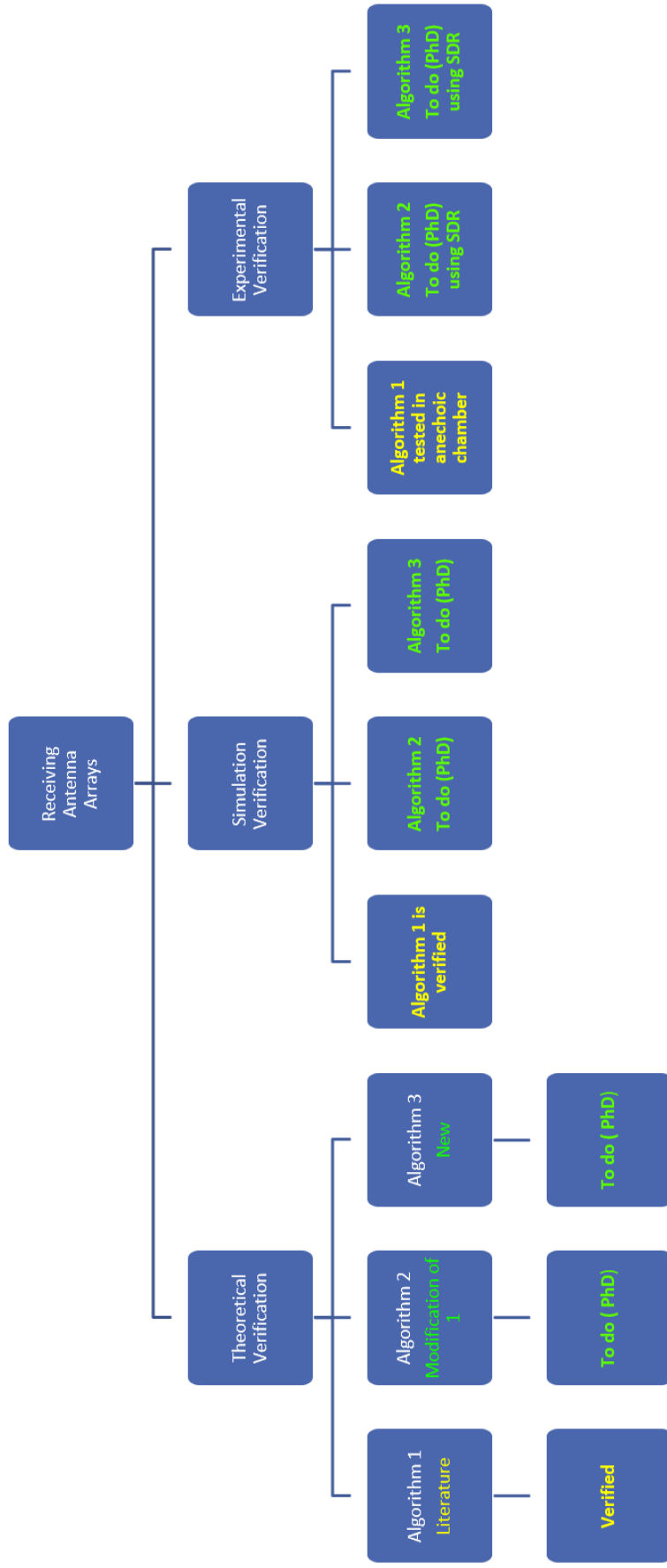


**Figure 1.7:** Organization of this thesis.



In Chapter 2, we present the theoretical foundations and background with thorough literature review of the different methods and techniques available for MCC and their limitations. The baseline theory is developed using one of the methods available in literature which is denoted as Algorithm I, followed by simulation results for DoA applications. After studying the limitations of this algorithm we try to improve it and develop Algorithm II which is a modified version of Algorithm I. Detailed analysis from theoretical and simulation aspects are presented. In order to deal with the limitations of Algorithm II, a novel method to compensate for mutual coupling is developed which is presented as Algorithm III. Chapter 3 deals with the experimental verification of all the three algorithms. An experimental study for Direction Finding (DF) is presented for Algorithm I for a seven-element monopole array in an anechoic chamber for single and multiple coherent sources. An experimental test-bed based on SDR is built for real-time DoA estimation and MCC based on Algorithm II. A second experimental test-bed was developed for testing Algorithm III in order to account for the limitations and challenges faced in the first hardware setup. Two different applications were demonstrated for MCC using the new setup and new algorithm which includes DoA estimation and spectral efficiency performance. Directional and omni-directional ULAs and UCAs were used during these experiments for studying real-time DoA estimation and DoA vs inter-element spacing with and without MCC. For spectral efficiency performance gauging, an End-to-End SIMO transceiver using IEEE 802.11a WiFi standard was implemented on SDR for reception of an HD image with and without MCC. Chapter 4 discusses the results and conclusions of all the different experiments as discussed in the previous chapter with detailed analysis and conclusions. Finally the summary and future work is discussed in Chapter 5.

## CHAPTER 2

### 2. THEORETICAL PART

#### 2.1. Background

Over the past 25 years, various MCC techniques have been developed based on the applications and the type of arrays under consideration. The effectiveness of each method varies and depends on the type of antenna used and the array configuration. They can broadly be divided into online and offline calibration techniques [8]. Offline methods include open circuit method, calibration method, full wave method and Received Mutual Impedance Method (RMIM). Online methods include signal processing techniques to estimate the coupling matrix.

First, Gupta and Ksienski in [9] and followed by other researchers [10]–[18] worked on the open-circuit voltage method to study the effect of MC in antenna arrays. The MC between two antennas is manifested by mutual impedance, i.e., the  $Z$  parameters. The antenna terminal voltage are related to open circuit voltages using the impedance matrix. However, in later studies it was observed that the open-circuit voltages (decoupled voltages) are not completely free from MC and errors are expected [19]–[25].

An S-Parameter method [26]–[28] was introduced in which the antenna array, receiving or transmitting, was modelled by an N-port network and the MC between the elements was modelled by the scattering parameters. After computing the scattering parameters, the decoupled signals were computed from the coupled measured terminal signals. However, this method suffered from the same problems as the open-circuit voltage method, especially in the receiving antenna arrays.

The full-wave (Moment) method suggested in [29]–[31] solves a boundary value problem

for the whole antenna array by method of moments. It uses the measurable terminal voltages and currents (mutually coupled) to calculate the incident field on the array (coupling free). However, this method results in under-determined system of equations since the voltages or current are known only on the terminals not on the whole antenna. To solve such an under-determined system, some approximations must be made, e.g., a known incident angle, current distribution assumption, etc. Hence, the performance of this method is limited by the approximation which may not be realistic at times. The main advantage of the full-wave method is that the coupling matrix estimate is very accurate. However, the a priori knowledge of the elevation angle of incoming signals is required to compute the decoupling matrix. Extending the work of Adve and Sarkar, Henault and Antar developed Multiple Antenna Induced EMF Method (MAIEM) [32]–[36] to generalize the full-wave method without using MoM. Although this method is extended to arbitrary geometries, the accuracy in real-time experimental calibration can be significantly diminished due to the use of theoretical evaluation of coupling using numerical analysis where required computational resources can rapidly become huge and significant differences between theory and experiments remain.

In 1990 isolated element pattern method was proposed by Steyskal and Herd [37] and was pursued by other researchers [38]–[41]. Here, the coupled voltage, at the antenna terminal, was expressed as a sum of two parts. One part was due to the response of a particular element due to the incident signal and the other part contained a linear combinations of all the other array elements due to the incoming signal. Determining the coupling coefficients was a major problem in this technique. Another method known as the coupled element pattern method was used by researchers as well [42]–[44]. The aim here was to predict the received coupled voltages from the coupled radiation patterns of the antenna elements. Coupled pattern is the pattern of an array element in the presence of the other elements when they are not excited. This method required huge memory to store the coupled patterns.

Another method known as the calibration method [5], [45]–[48] was suggested in which, first, the coupling matrix is formed. This matrix is similar to the impedance matrix in the open circuit voltage method and it relates the uncoupled and the coupled signals. The matrix is determined by experiments or by calculations based on known initial conditions. Obviously this method is only accurate as the experiments or calculations which can be

difficult at times. These experiments must be performed again if the array configuration changes therefore making this method tedious.

Decoupling can also be achieved by proper antenna design as discussed in [49], [50]. Although this method is simple and does not require additional processing, it is only applicable to certain types of antenna elements.

RMIM, initially proposed by [19] and further discussed in [20]–[25] was implemented to solve the problem of open-circuit voltage method. As opposed to the open-circuit voltage the decoupled voltages are obtained at load terminals of the antenna. This overcomes the problems faced in the open-circuit voltage method. In this method the antenna array is modeled as N-port circuit. The coupled and uncoupled voltages are related through an impedance matrix with receiving mutual impedances (RMI). The measurement, computation, and definition for the RMI are different from the conventional mutual impedance. The RMIM outperformed the open-circuit voltage method in direction finding [19], [23], [24]. RMIM is easy to implement and computational complexity is the same as the open-circuit voltage method.

Apart from these techniques some invasive methods have been used to reduce the mutual coupling between the array elements [51]–[57]. In such methods, Electromagnetic Band Gap (EBG) structures, decoupling networks, neutralization lines, and metamaterials are used to increase isolation between antenna elements. However, these techniques are not used here as the proposed method is based on non-invasive techniques.

## **2.2. Algorithm I: Received Mutual Impedance Method (RMIM)**

Algorithm I is referred in the literature as RMIM [58]–[67]. The RMI are calculated differently than the conventional mutual impedance which is based on an open-circuit assumption with the antenna array in the transmitting mode [9]. The following conditions are satisfied when using Algorithm I:

1. All antenna elements are terminated with a known impedance,  $Z_L$ .
2. The antenna elements are in receiving mode under an external plane-wave excitation.

### 2.2.1. Theoretical verification

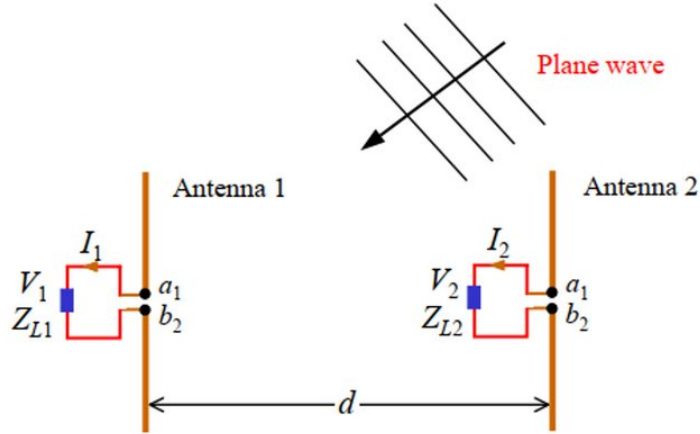


**Figure 2.1:** Scenario of a typical mutual coupling problem in receiving antenna arrays.

Consider a simple antenna array of two elements in the receiving case illuminated by an external plane wave as shown in **Figure 2.1**. The received voltage  $V_1$  at Antenna 1 is the sum of isolated voltage (due to the plane wave alone) and the coupled voltage (due to Antenna 2).

Therefore,

$$V_1 = S_1 + C_1 \quad (2.1)$$

Where,  $S_1$  denotes isolated voltage received by Antenna 1 when Antenna 2 is removed and  $C_1$  denotes coupled voltage induced on Antenna 1 due to the current  $I_2$  of Antenna 2. Hence,

$$C_1 = Z^{1,2} I_2 \quad (2.2)$$

$$I_2 = \frac{V_2}{Z_L} \quad (2.3)$$

Assuming that the all antennas are uniformly loaded which is  $50 \Omega$  for RF systems,

$$Z_{L1} = Z_{L2} = Z_L$$

Using (2.2) and (2.3) in (2.1) we get,

$$V_1 - Z^{1,2} \frac{V_2}{Z_L} = S_1 \quad (2.4)$$

Similarly,

$$V_2 - Z^{2,1} \frac{V_1}{Z_L} = S_2 \quad (2.5)$$

In matrix form (2.4) and (2.5) can be expressed as,

$$\begin{bmatrix} 1 & -\frac{Z^{1,2}}{Z_L} \\ -\frac{Z^{2,1}}{Z_L} & 1 \end{bmatrix} \begin{bmatrix} V_1 \\ V_2 \end{bmatrix} = \begin{bmatrix} S_1 \\ S_2 \end{bmatrix} \quad (2.6)$$

or

$$[\mathbf{Z}] [\mathbf{V}_c] = [\mathbf{S}_i] \quad (2.7)$$

The above formulation can be extended to an N element array. In this thesis,  $N = 4$  is fixed unless mentioned. Then the resultant equations can be written as below,

$$V_1 - Z^{1,2} \frac{V_2}{Z_L} - Z^{1,3} \frac{V_3}{Z_L} - Z^{1,4} \frac{V_4}{Z_L} = S_1 \quad (2.8)$$

$$V_2 - Z^{2,1} \frac{V_1}{Z_L} - Z^{2,3} \frac{V_3}{Z_L} - Z^{2,4} \frac{V_4}{Z_L} = S_2 \quad (2.9)$$

$$V_3 - Z^{3,1} \frac{V_1}{Z_L} - Z^{3,2} \frac{V_2}{Z_L} - Z^{3,4} \frac{V_4}{Z_L} = S_3 \quad (2.10)$$

$$V_4 - Z^{4,1} \frac{V_1}{Z_L} - Z^{4,2} \frac{V_2}{Z_L} - Z^{4,3} \frac{V_3}{Z_L} = S_4 \quad (2.11)$$

In matrix form, Eqs. (2.8) to (2.11) can be expressed as,

$$\begin{bmatrix} 1 & -\frac{Z^{1,2}}{Z_L} & -\frac{Z^{1,3}}{Z_L} & -\frac{Z^{1,4}}{Z_L} \\ -\frac{Z^{2,1}}{Z_L} & 1 & -\frac{Z^{2,3}}{Z_L} & -\frac{Z^{2,4}}{Z_L} \\ -\frac{Z^{3,1}}{Z_L} & -\frac{Z^{3,2}}{Z_L} & 1 & -\frac{Z^{3,4}}{Z_L} \\ -\frac{Z^{4,1}}{Z_L} & -\frac{Z^{4,2}}{Z_L} & -\frac{Z^{4,3}}{Z_L} & 1 \end{bmatrix} \begin{bmatrix} V_1 \\ V_2 \\ V_3 \\ V_4 \end{bmatrix} = \begin{bmatrix} S_1 \\ S_2 \\ S_3 \\ S_4 \end{bmatrix} \quad (2.12)$$

$$[\mathbf{Z}(\boldsymbol{\theta})] [\mathbf{V}_c(\boldsymbol{\theta}, \boldsymbol{\varphi})] = [\mathbf{S}_i(\boldsymbol{\theta}, \boldsymbol{\varphi})]$$

[Decoupling Matrix] [Received Voltages with Coupling] = [Isolated voltages]

From (2.12) it can be inferred that the isolated voltage received by the  $n_{th}$  antenna is equal to the received voltage in the presence of coupling by the  $n_{th}$  antenna after subtracting the coupled voltage due to the other  $n - 1$  antenna elements present in the array. It can be seen that (2.12) is an under-determined system where we have  $N$  equations and  $N(N - 1)$  unknowns. How can we solve the above equations for the unknown mutual impedances?

In [58], the author tries to solve the above set of equations by exciting the array from  $P$  different azimuth angles ( with fixed elevation  $\theta = 90^\circ$  ). This results in  $P$  sets of equations. Since in one equation there are only  $N - 1$  unknowns therefore to get a unique solution  $P \geq (N - 1)$ .

Consider (2.8), by exciting from  $P$  different angles, we can write the following,

$$\begin{bmatrix} I_2^{\phi_1} & I_3^{\phi_1} & I_4^{\phi_1} \\ I_2^{\phi_2} & I_3^{\phi_2} & I_4^{\phi_2} \\ \vdots & \vdots & \vdots \\ I_2^{\phi_{N-2}} & I_3^{\phi_{N-2}} & I_4^{\phi_{N-2}} \\ I_2^{\phi_{N-1}} & I_3^{\phi_{N-1}} & I_4^{\phi_{N-1}} \end{bmatrix}_{P \times (N-1)} \begin{bmatrix} Z^{1,2} \\ Z^{1,3} \\ Z^{1,4} \end{bmatrix}_{(N-1) \times 1} = \begin{bmatrix} V_1^{\phi_1} - S_1^{\phi_1} \\ V_1^{\phi_2} - S_1^{\phi_2} \\ \vdots \\ V_1^{\phi_{N-2}} - S_1^{\phi_{N-2}} \\ V_1^{\phi_{N-1}} - S_1^{\phi_{N-1}} \end{bmatrix}_{P \times 1} \quad (2.13)$$

$$\begin{bmatrix} \mathbf{A} \end{bmatrix} \begin{bmatrix} \mathbf{X} \end{bmatrix} = \begin{bmatrix} \mathbf{b} \end{bmatrix}$$

The above system can be solved by applying Least Squares (LS) solution.

$$\mathbf{X} = (\mathbf{A}^T \mathbf{A})^{-1} \mathbf{A}^T \mathbf{b} \quad (2.14)$$

The quantity  $(\mathbf{A}^T \mathbf{A})^{-1} \mathbf{A}^T$  denotes the Moore-Penrose pseudo-inverse.

The rest of the equations, (2.9) to (2.11), follow in the same fashion. Once the unknown impedances in (2.13) are found then using (2.12), the received voltages can be decoupled.

### 2.2.2. Direction of Arrival Estimation

An important application for receiving antenna arrays is DoA estimation. In receiving case, usually the direction of arrival is an important parameter that is being sought after in many applications such as MIMO and radar. DoA estimation can be broadly divided in two main categories namely classical methods and subspace methods as shown in **Figure 2.2**. Classical methods are based on beamforming where the received power is measured by forming a beam in a specific direction and scanning the space. The highest power received is the DoA. Subspace methods have super-resolution capabilities which can be further divided into noise and signal subspace methods. In the former case, only the signal subspace is retained which increases the SNR. This can be further divided into



search-based or algebraic methods. On the other hand, noise subspace methods assume that the array manifold vectors are in the signal subspace and are orthogonal to the noise subspace. Here it should be mentioned that search based algorithms can be applied to any array structure unlike algebraic algorithms which are dependent on the array geometry. As an example, MUSIC can be applied to any array structure however RootMusic is limited to ULA only. Different algorithms have been used for the estimation of DoA namely MUSIC [68], ESPRIT [69], Capon (MVDR) [70] [71], RootMusic [72], Beam-Scan, BeamSpaceEsprit [73]. The most robust amongst all these algorithms is MUSIC which always gives the best results. In order to display the DoA in real-time a MATLAB application was designed.

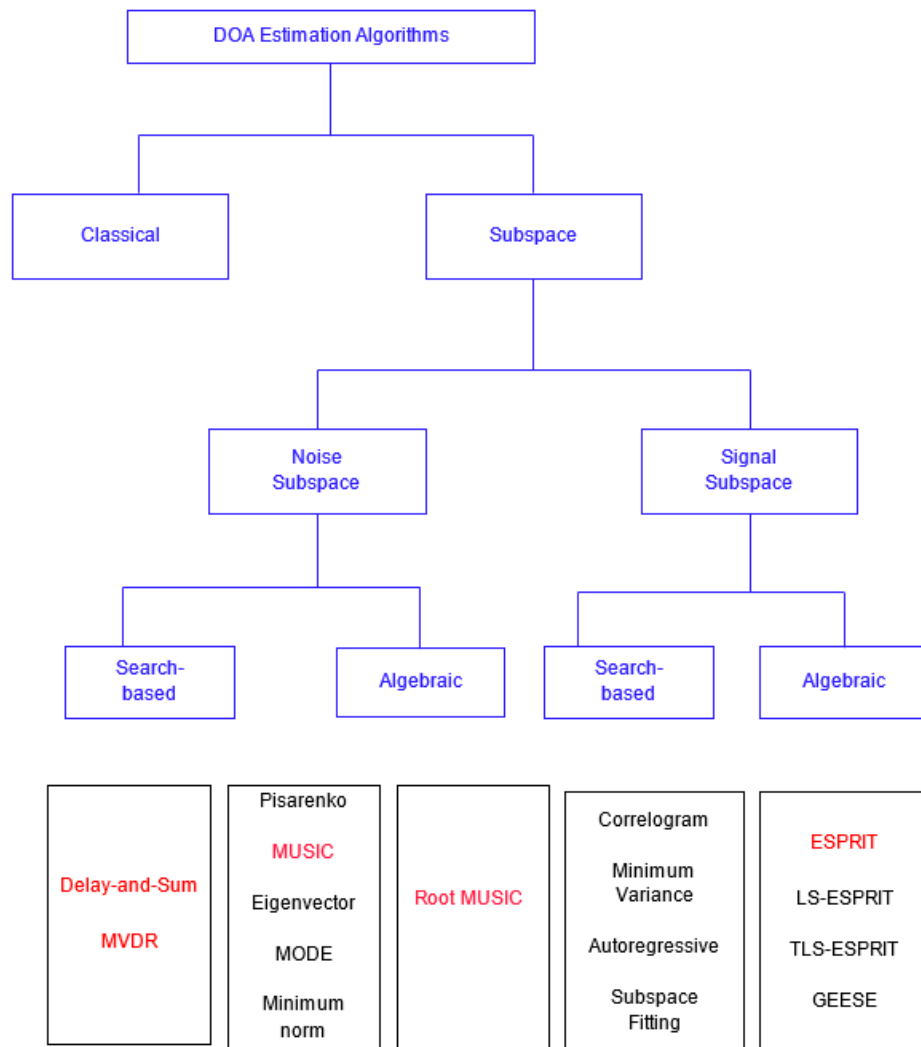


**Figure 2.2:** Classification of DoA estimation techniques.

### 2.2.3. Simulation verification

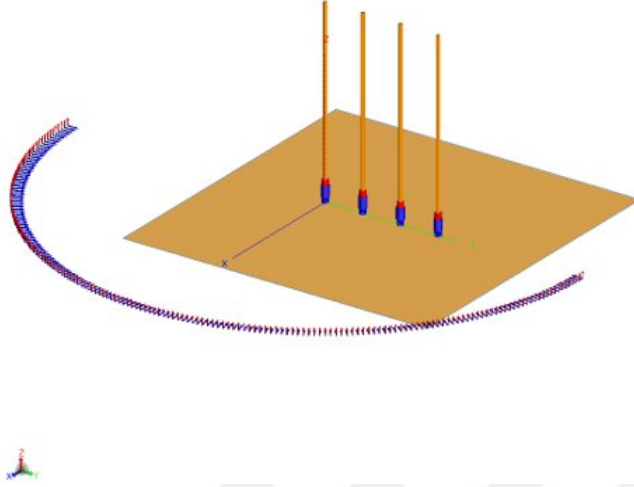


**Figure 2.3:** Four element monopole ULA in FEKO with  $l = 0.24\lambda$ ,  $l/a = 100$ ,  $Z_L = 50 \Omega$  at 2.4 GHz. The incident plane wave is shown from  $\phi = -90^\circ$  to  $90^\circ$  and  $\theta = 90^\circ$ .

In the presence of coupling, the received voltages are corrupted therefore the DoA estimation is erroneous. Therefore, we would like to first compensate for MC and then estimate DoA. There are a number of algorithms available for DoA estimation in which the most famous is Multiple Signal Classification (MUSIC) [68]. An in-house EM simulator based on MoM was developed for thin wire antennas in the transmitting case [7], [74], and was modified for receiving antenna arrays in MATLAB. A four element monopole ULA was simulated using FEKO as well as MATLAB in the receiving case as shown in **Figure 2.3**. The antenna elements are spaced at a fix distance  $d$ . This array can be excited in azimuth by  $\phi = -90^\circ$  to  $90^\circ$  and the elevation angle  $\theta = 90^\circ$  is fixed. The voltages received by this array from any incident angle is denoted as  $V_c$ , i.e, the received coupled voltages in the presence of coupling because of the presence of other antenna elements. The undesired EM interaction takes place between these elements which corrupt the received voltages.

In order to find the isolated voltages  $S_i$  for this array every antenna is placed at its array position by removing all other  $N - 1$  antennas and then simulating for the given incident angles. Thus by running the EM simulation for each of these single antennas we can get the isolated voltages for this array.

The compensated voltages are calculated using (2.12) by first computing the decoupling matrix  $Z$ . Therefore, we have three sets of voltages, namely, the coupled voltages, isolated

voltages and compensated voltages. These three sets of voltages can be given as an input to MUSIC in order to estimate the DoA.

In **Figure 2.4**, we can see the power spectrum for MUSIC for the three sets of received voltages. In the presence of coupling, the estimated DoA was off by  $6^\circ$  for the first incident angle  $\phi_1$  and  $5^\circ$  for  $\phi_2$ . However, after compensation the correct DoA was estimated. The isolated voltages correspond to the voltages when there is no coupling therefore it is the solution we want to achieve. Here, it should be noted that even though the spacing was  $d = 0.5\lambda$ , which is the common spacing used in many applications in the literature, the MC is manifested by the estimated DoAs.

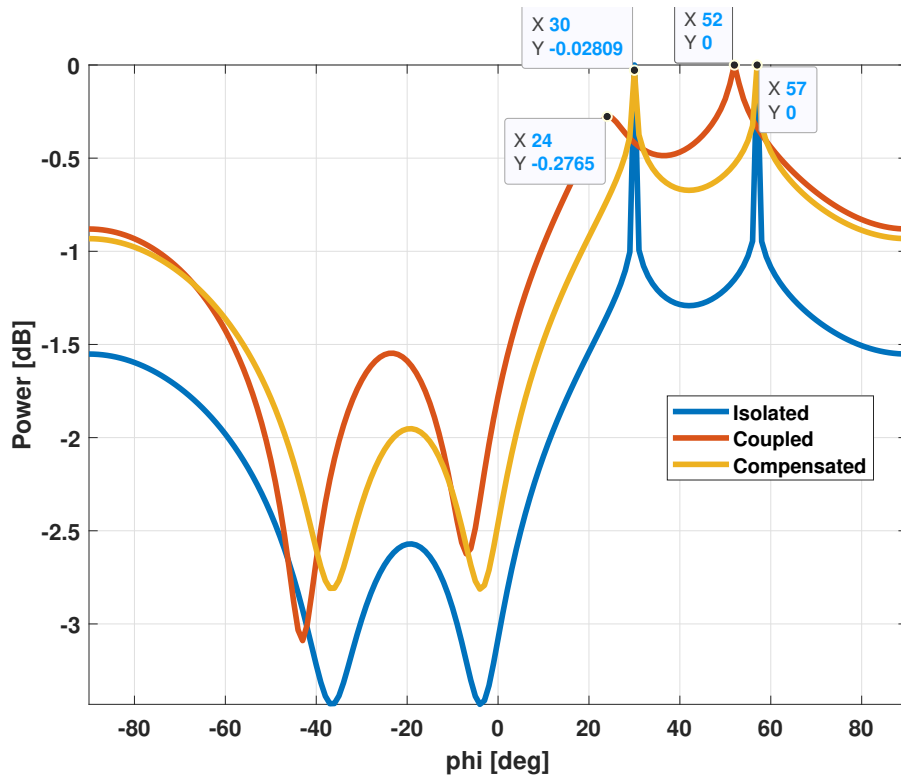


**Figure 2.4:** Spatial spectrum of the MUSIC algorithm for DoA detection of two coherent signals from  $\phi_1 = 30^\circ$ ,  $\phi_2 = 57^\circ$  and  $\theta = 90^\circ$  for four-element ULA with  $d = 0.5\lambda$ .

**Figure 2.5** and **Figure 2.6** show the estimated DoA for the case when  $d = 0.25\lambda$ . In the first case, the same incident angles were used as in **Figure 2.4** to show the effect of MC when spacing is decreased. It can be observed that in the presence of coupling there was no distinct peak whereas after compensation the correct DoA was estimated. As  $d$  was decreased, the same antenna array suffered from high MC thus resulting in corrupted voltages that result in the wrong DoA estimate. In the second case, the angular spacing

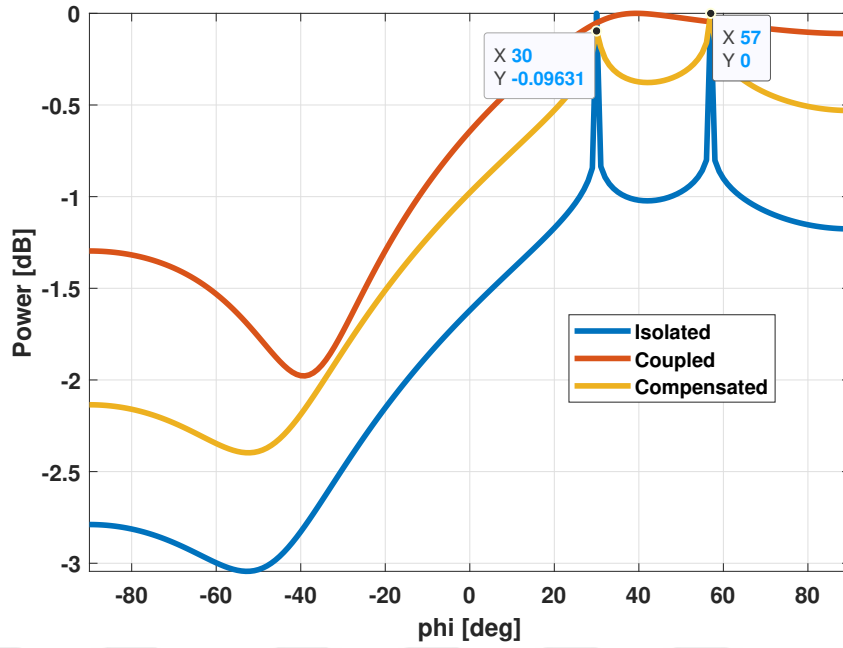


**Figure 2.5:** Spatial spectrum of the MUSIC algorithm for DoA detection of two coherent signals from  $\phi_1 = 30^\circ$ ,  $\phi_2 = 57^\circ$  and  $\theta = 90^\circ$  for four-element ULA with  $d = 0.25\lambda$ .

between the two incident sources was decreased such that  $\phi_1 = 5^\circ$  and  $\phi_2 = -11^\circ$ . The computed DoA got worse for the coupled case which shows only one peak at  $0^\circ$  whereas after compensation the exact DoA was estimated.

For theta detection, we used three different methods, brute force, iterative approach, and narrowing the search window by fixing a threshold. In Algorithm I, since  $Z$  is a function of  $\theta$ , therefore, we first calculate all the corresponding decoupling matrices and then apply the above algorithms to calculate the corresponding elevation angle. An example is shown in **Figure 2.7** where the 2D spectrum for all the detected angles are plotted. It is shown that false detection can occur when searching for the peak. In this case, the correct DoA is  $\phi = 25^\circ$ ,  $\theta = 45^\circ$  but 0.48 dB higher is another peak detected with the wrong DoA. This also shows the limitation of this technique since here  $Z$  is dependent on  $\theta$ .

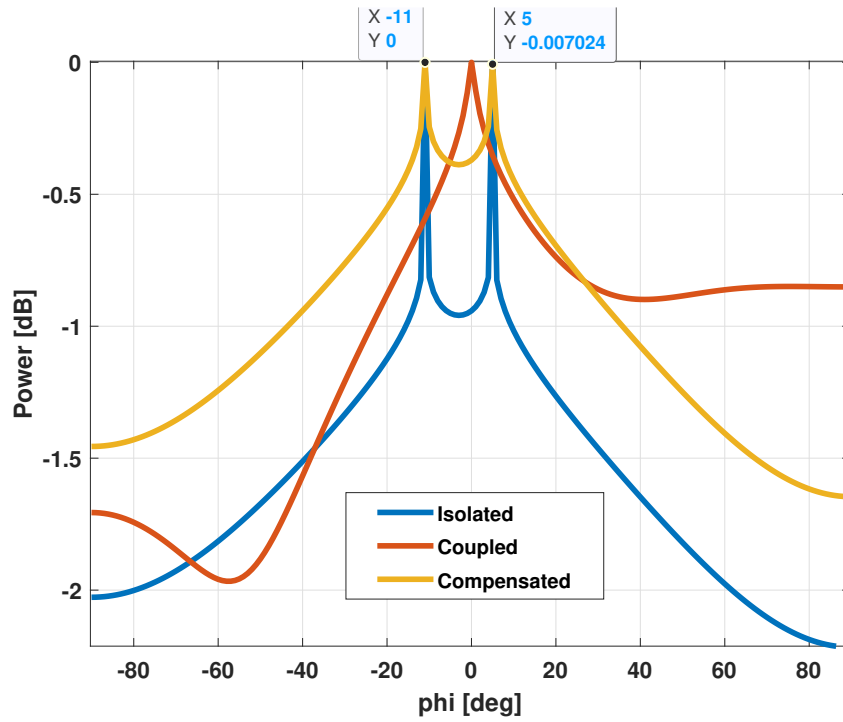


**Figure 2.6:** Spatial spectrum of the MUSIC algorithm for DoA detection of two coherent signals from  $\phi_1 = 5^\circ$ ,  $\phi_2 = -11^\circ$  and  $\theta = 90^\circ$  for four-element ULA with  $d = 0.25\lambda$ .

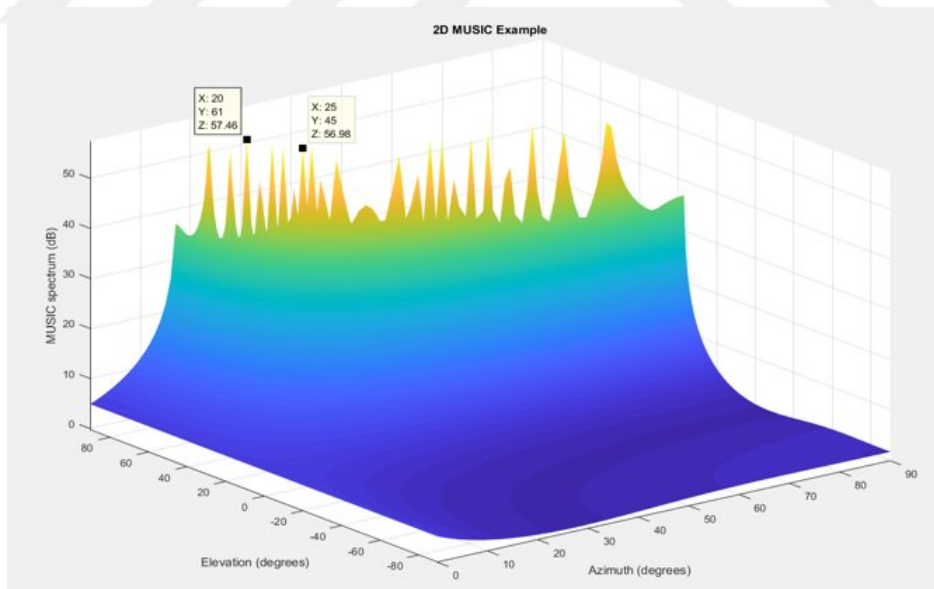


**Figure 2.7:** 2D spatial spectrum of the MUSIC algorithm for DoA detection for an incident signal  $\phi = 25^\circ$  and  $\theta = 45^\circ$  for four-element ULA with  $d = 0.25\lambda$ .

#### 2.2.4. Limitations

In [58]–[62], the author concludes the following:

1. This method works only for omni-directional antennas.
2. The  $Z$  matrix or decoupling matrix is independent of  $\phi$  (azimuth) but dependent on  $\theta$  (elevation).
3. From (2), it concludes that for every  $\theta$ , there is a different  $Z$  matrix.
4. For multiple incident sources that maybe coherent in nature e.g., DoA application, this method is limited by the angular spacing between the incident sources.
5. The author used  $P = 10$ , i.e., 10 different azimuth incident angles between  $\phi = 0^\circ$  to  $\phi = 180^\circ$  in order to solve for the unknown mutual impedances in (2.12). Thus, for every angle we need  $2N$  measurements hence in total we have  $P \times 2N$  which results in  $10 \times 2 \times 4 = 80$  measurements for a four element array which makes this method highly impractical.

It should be noted that in this method an over-determined system is solved.

#### 2.3. Algorithm II: Mutual Coupling Compensation In Receiving Antenna Arrays

In this section, we will address the limitations of Algorithm I by deriving Algorithm II which is a modified version of **Section 2.2**. The main problem of this thesis is defined by **Figure 2.8** in which a decoupling matrix  $Z$  needs to be computed such that after multiplication with the received coupled voltages the isolated voltages can be obtained. In order to compute this decoupling matrix, we need to solve for  $N(N - 1)$  unknowns. Multiple measurements are required from various incident angles in order to compute the mutual impedances. This may not be practical for experimental purposes since for every angle the coupled voltage as well as the isolated voltage needs to be measured resulting in  $P \times 2N$  measurements. In this section, we will present how the unknowns can be reduced from  $N(N - 1)$  to  $N - 1$  and solve for  $Z$  to get a unique solution which addresses the limitations of the previous algorithm. Furthermore, we show that the mutual impedance is constant for all angles and depends solely on the geometry of the antenna array. Since the mutual

impedance is independent of the angle of arrival, using only one measurement, we find the decoupling matrix which decouples any received voltage for all  $\theta$  and  $\phi$ . This reduces the computation complexity and the physical labour in the experiments without degrading the accuracy of MCC.

First, the formulation will be presented followed by numerical results for ULA and UCA of thin wire dipole arrays. MoM is used to find the currents and voltages on the single mode antennas for simulation verification. In the end, experimental results will be presented for this method by designing an experimental test-bed based on SDRs which will be presented in the following chapters.

$$[\mathbf{Z}] [\mathbf{V}_c(\theta, \phi)] = [\mathbf{S}_i(\theta, \phi)]$$

[Decoupling Matrix] [Received Voltages with Coupling] = [Isolated voltages]

Figure 2.8: Problem statement.

### 2.3.1. Formulation

Consider an  $N$  element array of thin wire dipoles where each element is terminated with a load  $Z_L$ . The received voltage at the antenna terminal  $V_i$  can be written as

$$V_i = I_i Z_L \quad (2.15)$$

The received voltage is the sum of two voltages,  $S_i$  and  $C_i$ .  $S_i$  is the voltage induced on the  $i^{th}$  isolated antenna and  $C_i$  is the coupling effect from other elements. Thus (2.15) can be rewritten as,

$$V_i = S_i + C_i \quad (2.16)$$

$C_i$  includes the re-radiation effects from all the other elements of the array on the  $i^{th}$  antenna as:

$$C_i = Z^{i,1} I_1 + Z^{i,2} I_2 + \dots + Z^{i,i-1} I_{i-1} + Z^{i,i+1} I_{i+1} + \dots + Z^{i,N} I_N \quad (2.17)$$

Here,  $Z^{i,j}$  is the mutual impedance between elements  $i$  and  $j$  and  $I_j$  is the current induced

at the  $j^{th}$  port, given by:

$$I_j = \frac{V_j}{Z_L} \quad \text{for } j = 1, 2, \dots, N. \quad (2.18)$$

$$V_i - \left[ Z^{i,1} \frac{V_1}{Z_L} + Z^{i,2} \frac{V_2}{Z_L} + \dots + Z^{i,i-1} \frac{V_{i-1}}{Z_L} + Z^{i,i+1} \frac{V_{i+1}}{Z_L} + \dots + Z^{i,N} \frac{V_N}{Z_L} \right] = S_i \quad (2.19)$$

Where,  $i = 1, 2, \dots, N$ . From (2.19), we have  $N(N-1)$  unknowns and  $N$  equations. Due to symmetry of the structure, the mutual impedance matrix is toeplitz in nature. Hence, the number of unknowns are reduced to  $N-1$  which can be solved by applying LS method to the over-determined system for a single incident angle. Equation (2.19) can be written as follows for  $N = 4$ . Then, from (2.16), (2.17) and (2.18) we get,

$$V_1 - Z^{1,2} \frac{V_2}{Z_L} - Z^{1,3} \frac{V_3}{Z_L} - Z^{1,4} \frac{V_4}{Z_L} = S_1 \quad (2.20)$$

$$V_2 - Z^{1,2} \frac{V_1}{Z_L} - Z^{1,2} \frac{V_3}{Z_L} - Z^{1,3} \frac{V_4}{Z_L} = S_2 \quad (2.21)$$

$$V_3 - Z^{1,3} \frac{V_1}{Z_L} - Z^{1,2} \frac{V_2}{Z_L} - Z^{1,2} \frac{V_4}{Z_L} = S_3 \quad (2.22)$$

$$V_4 - Z^{1,4} \frac{V_1}{Z_L} - Z^{1,3} \frac{V_2}{Z_L} - Z^{1,2} \frac{V_3}{Z_L} = S_4 \quad (2.23)$$

There are three unknowns,  $Z^{1,2}$ ,  $Z^{1,3}$  and  $Z^{1,4}$  which can be solved by applying LS method.

For the above case of  $N = 4$ , (2.20) to (2.23) can be written in LS form of

$$AX = b \quad (2.24)$$

Where,



$$A = \begin{bmatrix} I_2 & I_3 & I_4 \\ I_1 + I_3 & I_4 & 0 \\ I_2 + I_4 & I_1 & 0 \\ I_3 & I_2 & I_1 \end{bmatrix} \quad (2.25)$$

$$X = \begin{bmatrix} Z^{1,2} \\ Z^{1,3} \\ Z^{1,4} \end{bmatrix} \quad (2.26)$$

$$b = \begin{bmatrix} S_1 - V_1 \\ S_2 - V_2 \\ S_3 - V_3 \\ S_4 - V_4 \end{bmatrix} \quad (2.27)$$

Once the mutual impedances are found, the decoupling matrix can be used as follows:

$$\begin{bmatrix}
1 & -\frac{Z^{1,2}}{Z_L} & -\frac{Z^{1,3}}{Z_L} & -\frac{Z^{1,4}}{Z_L} \\
-\frac{Z^{1,2}}{Z_L} & 1 & -\frac{Z^{1,2}}{Z_L} & -\frac{Z^{1,3}}{Z_L} \\
-\frac{Z^{1,3}}{Z_L} & -\frac{Z^{1,2}}{Z_L} & 1 & -\frac{Z^{1,2}}{Z_L} \\
-\frac{Z^{1,4}}{Z_L} & -\frac{Z^{1,3}}{Z_L} & -\frac{Z^{1,2}}{Z_L} & 1
\end{bmatrix}
\begin{bmatrix}
V_1 \\
V_2 \\
V_3 \\
V_4
\end{bmatrix}
=
\begin{bmatrix}
S_1 \\
S_2 \\
S_3 \\
S_4
\end{bmatrix}
\quad (2.28)$$

### 2.3.2. Numerical examples

In this section, to show the MCC, examples of four-element ULA and UCA of thin wire dipole antennas are presented. The computations are done using MoM using the in-house EM simulator for the received case as mentioned in [7], [74] for computing the coupled voltages and the isolated voltages. The mutual impedances calculated by the proposed method are compared with Algorithm I in **Section 2.2** [58]. The coupled voltages are compensated for, by the developed compensation method. These are then fed into to the MUSIC algorithm, to estimate the DoA of an incident signal. The DoA is estimated for two-coherent sources using the decoupled voltages in the case of ULA. For UCA, the received voltages have been tabulated in order to show the accuracy of the algorithm. The mutual impedances are also presented as a function of all  $\theta$  and  $\phi$  to show that they are constant and are independent of the incident angles. Thus one unique matrix can decouple all the received voltages from any incident angle  $(\theta, \phi)$ .

#### 2.3.2.1. Four-element ULA

A ULA with four dipole antennas at 2.4 GHz is considered with spacing  $d = 0.2\lambda$ , length  $l = 0.48\lambda$  and  $l/a = 100$ , where  $a$  is the radius and  $\lambda$  is the free space wavelength. Each antenna is terminated with  $Z_L = 50 \Omega$  load impedance. The array as shown in **Figure 2.9** is excited by a plane wave with  $\theta = 90^\circ$  and  $\phi = 90^\circ$ , where  $\theta$  and  $\phi$  are measured from positive  $z$  and positive  $x$  directions, respectively. These angles are chosen because coupling effect is maximum for the ULA. Using MoM, we find the received voltages at each antenna terminal, which is the coupled voltage. Then, the isolated voltages are computed

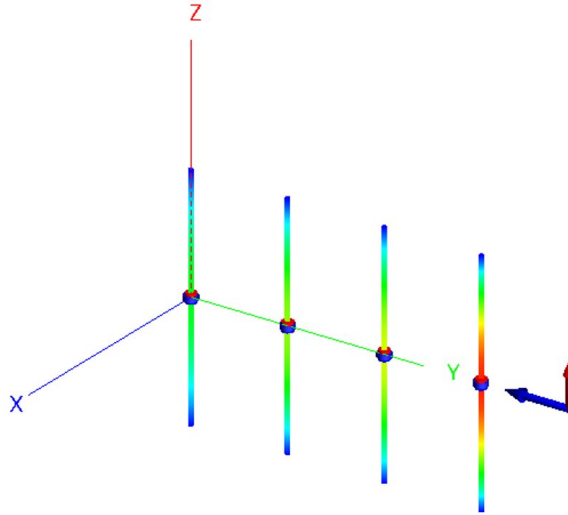


**Figure 2.9:** Four element thin wire dipole array with  $d=0.2\lambda$  being excited by a plane wave with  $\theta=90^\circ$  and  $\phi=90^\circ$ .

by considering one antenna at a time in the absence of all other elements at its respective position in the array. Solving (2.20) to (2.23), we find the mutual impedances which are shown in **Table 2.1**. Although the observed values are close in comparison for the two methods, however this is only one  $Z$  matrix for  $\theta = 90^\circ$  in case of Algorithm I. In other words, if we change the elevation angle we need to compute a different  $Z$  matrix. However, in Algorithm II only one unique matrix is sufficient for all incident angles  $(\theta, \phi)$ . It should be noted that in the proposed method, only one incident measurement angle  $(\theta, \phi)$  was used resulting in only  $2N$  measurements to compute the mutual impedances, whereas in [58] at least 10 angles were required to compute the same mutual impedances with  $20N$  measurements. It was observed that the mutual impedances found in the proposed method are more accurate than in [58]. Since mutual impedance is independent of the

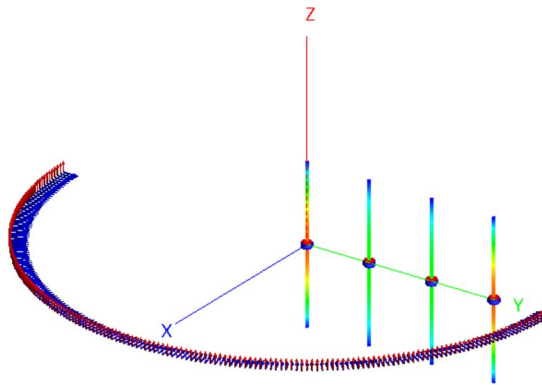


**Figure 2.10:** Four element ULA of thin wire antennas with  $d=0.2\lambda$  under different plane-wave excitation.

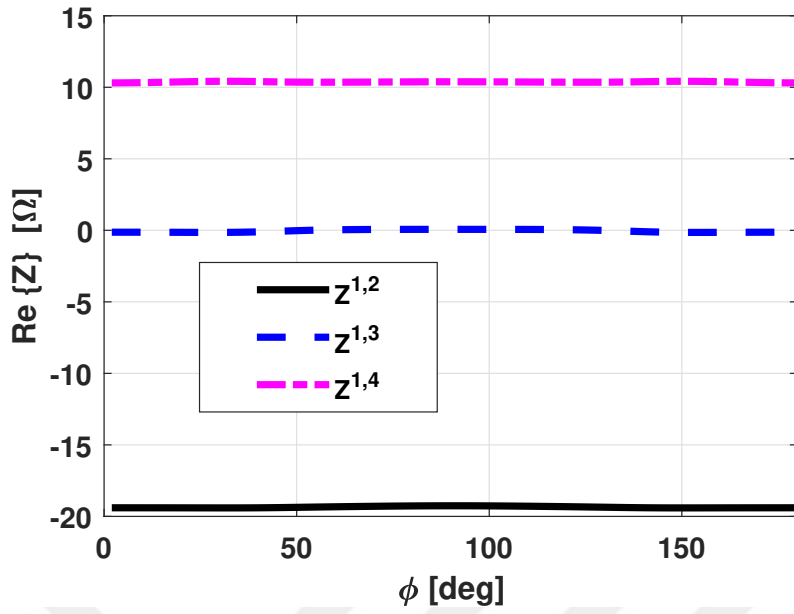


**Figure 2.11:** Real part of the mutual impedance matrix for four element ULA with  $d=0.2\lambda$ , for all elevation angles.

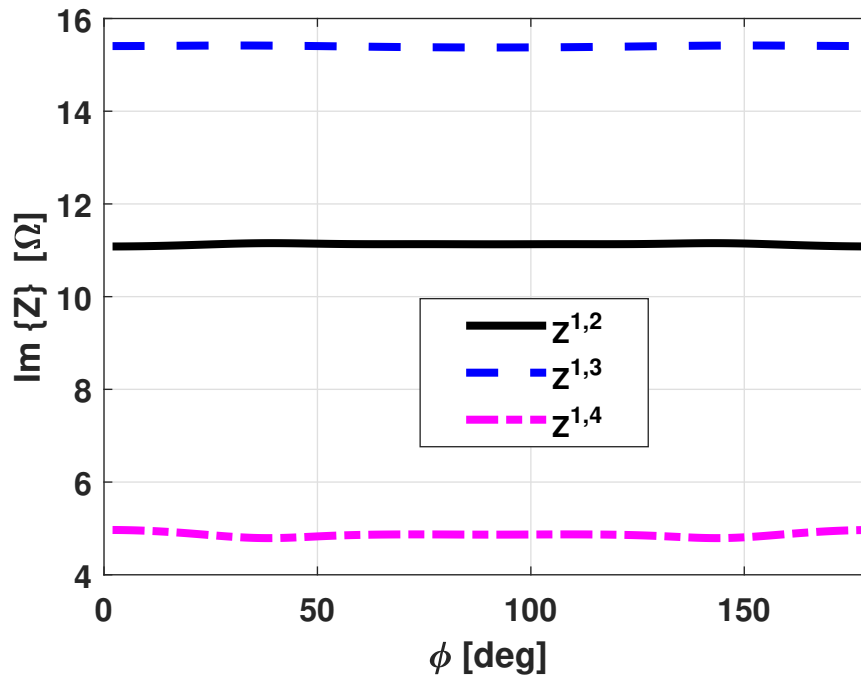


**Figure 2.12:** Imaginary part of the mutual impedance matrix for four element ULA with  $d=0.2\lambda$ , for all elevation angles.

angle of arrival, the decoupling matrix of the proposed method can decouple any voltage irrespective of the incident angle, whereas [58] considers  $Z$  a function of  $\theta$  which results in multiple decoupling matrices for different elevation angles. The real and imaginary mutual impedances are shown in **Figure 2.11** and **Figure 2.12** which are constant for all angles  $(\theta, \phi)$ . For the same setup shown in **Figure 2.10**, different incident azimuth angles that varied from  $\phi = -90^\circ$  to  $90^\circ$  while keeping the elevation angle fixed at  $\theta = 90^\circ$ , the real part of the impedance matrix,  $Z_{12}$ ,  $Z_{13}$ , and  $Z_{14}$  were found to be constant for the array. It was interesting to see that when the elevation angle was varied, the same result was obtained. This proved that the decoupling matrix is independent of both elevation and azimuth and is a constant thus ratifying the results and methodology at hand.

**Table 2.1:** Received mutual impedance for a four element ULA.

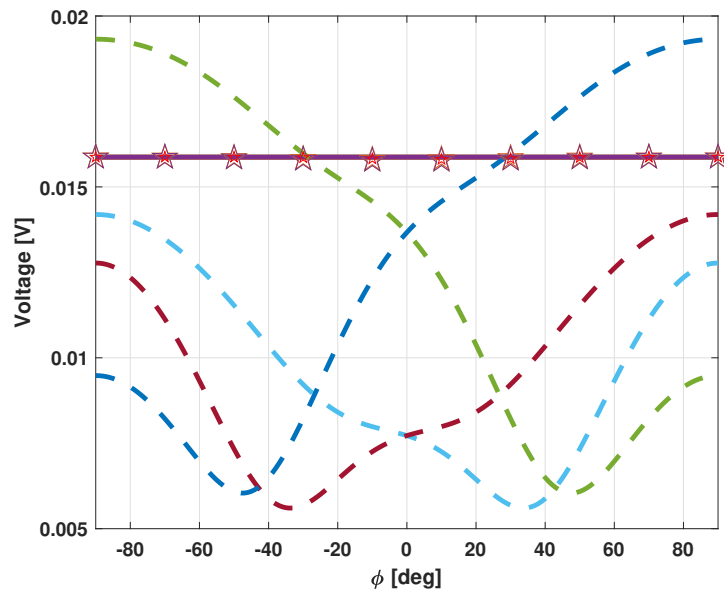
Comparison	ULA		
	$Z^{1,2}$	$Z^{1,3}$	$Z^{1,4}$
Algorithm II	$-19.26 + 11.13i$	$0.0675 + 15.38i$	$10.39 + 4.866i$
Algorithm I [58]	$-18.47 + 10.94i$	$0.0263 + 15.61i$	$10.72 + 4.732i$

In **Figure 2.13**, we see the magnitude and phase of the received voltages for a four-element ULA of thin wire dipole antennas with  $d=0.2\lambda$ . The elevation angle of the incident signal is set to  $\theta = 90^\circ$  and the azimuth angle is varied from  $\phi = -90^\circ$  to  $90^\circ$ . In these plots, we see three sets of voltages, the solid lines show the isolated voltages, the dashed lines show the coupled voltages, and the star markers show the compensated voltages. It should be noted that the compensated voltages for all the angles were calculated by the mutual impedances shown in **Table 2.1**. In other words, only one matrix multiplication resulted in the decoupling of all the 180 different incident azimuth angles for a fixed elevation. It is clear that the coupled voltages are very different from the isolated and compensated voltages. Similarly, the compensated phase plot shows excellent agreement with the isolated phase whereas the effect of MC is manifested by the coupled phases. A similar plot is shown in **Figure 2.14**, this time  $\theta$  is varied and the azimuth angle is fixed to  $\phi = 90^\circ$ . It can be observed that the magnitudes of the isolated and compensated voltages are exactly the same whereas the coupled magnitudes are all over the place. The phase plot shows that after MCC the isolated phases were retrieved exactly whereas in the presence of MC

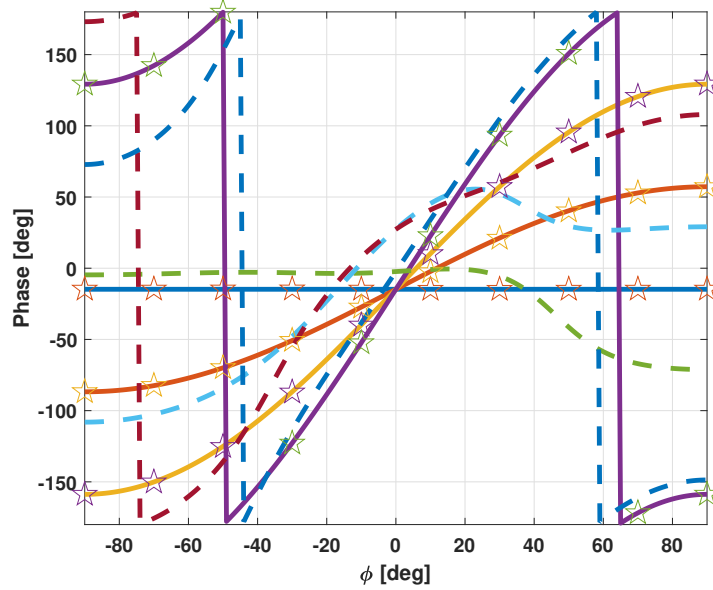
the phases were distorted. Again, it should be highlighted here that the compensation was done using the same mutual impedances shown in **Table 2.1**. Thus all  $\theta$  and  $\phi$  voltages were decoupled using a single unique square matrix and the complexity is only one matrix multiplication.



a)



b)



c)

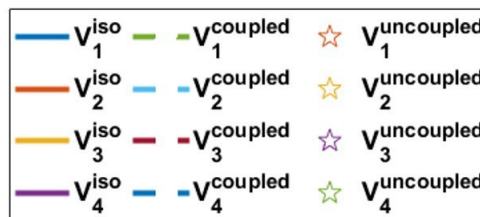
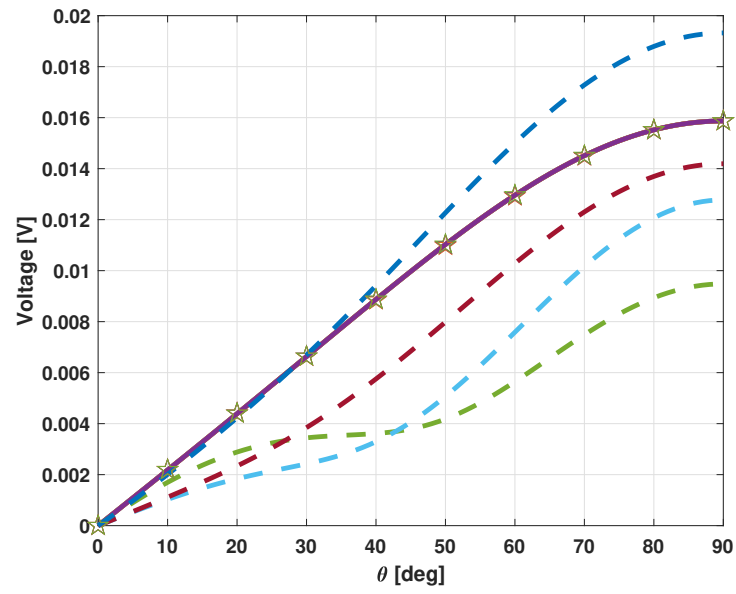
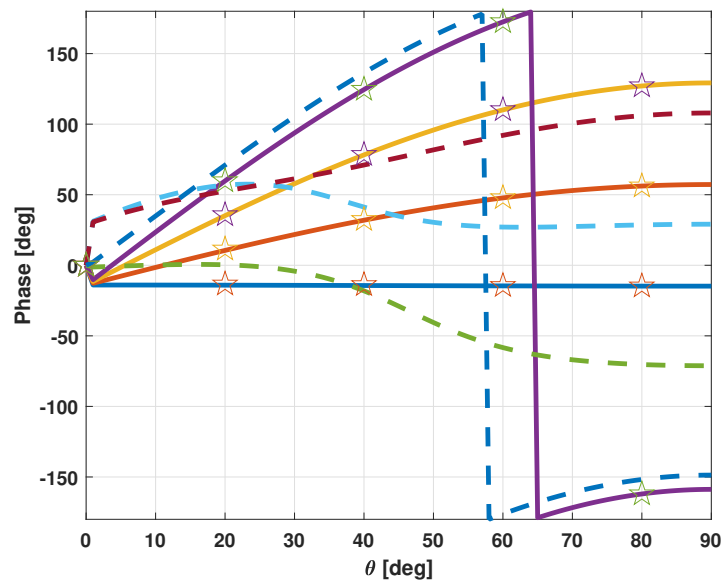


**Figure 2.13:** Received voltages for a four element ULA  $\phi$  variation,  $\theta = 90^\circ$  a) magnitude, b) phase, c) legend.

a)



b)



c)

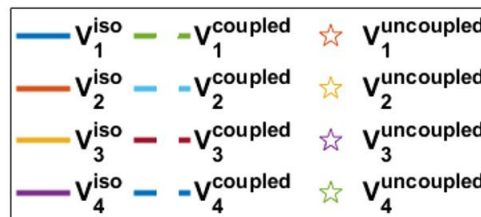


**Figure 2.14:** Received voltages for a four element ULA  $\theta$  variation,  $\phi = 90^\circ$  **a)** magnitude, **b)** phase, **c)** legend.



### 2.3.2.2. DoA estimation of two coherent sources

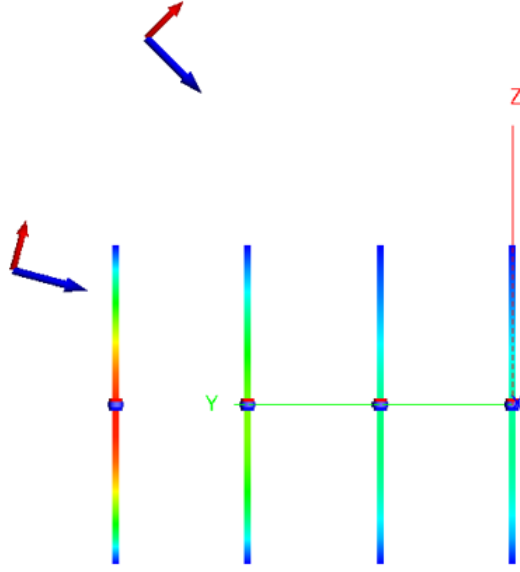


**Figure 2.15:** DoA estimation of two coherent sources for a fixed azimuth  $\phi = 90^\circ$  and two different elevation angles,  $\theta_1=45^\circ$  and  $\theta_2=75^\circ$ .

After MC compensation, we wanted to gauge our method so we applied it to DoA estimation of two coherent sources. Here, two cases for DoA estimation are discussed. In case I, the ULA was excited by two plane waves, with fixed  $\phi = 90^\circ$  and different elevation angles,  $\theta_1=45^\circ$  and  $\theta_2=75^\circ$  as shown in **Figure 2.15**. The uncoupled voltages were computed using the mutual impedances of **Table 2.1**. The isolated, coupled and uncoupled voltages were given as an input to MUSIC algorithm with forward-only spatial smoothing [68], [75] due to the coherent sources as plane wave.

The estimated DoA can be seen in **Figure 2.16** exactly by the isolated voltages which has no coupling. The other two line plots show the DoA estimation of the coupled and compensated voltages. It can be clearly observed that in the presence of coupling the two signals were not detected whereas after compensation the correct DoAs were estimated.

The setup for the second case is shown in **Figure 2.17**, the plane waves were incident from a fixed  $\theta = 90^\circ$  but different azimuth angles  $\phi_1 = 45^\circ$  and  $\phi_2 = 75^\circ$ . Again, we can see that the DoA was accurately estimated as shown in **Figure 2.18** in the compensated case whereas for the coupled case no particular peak was observed.

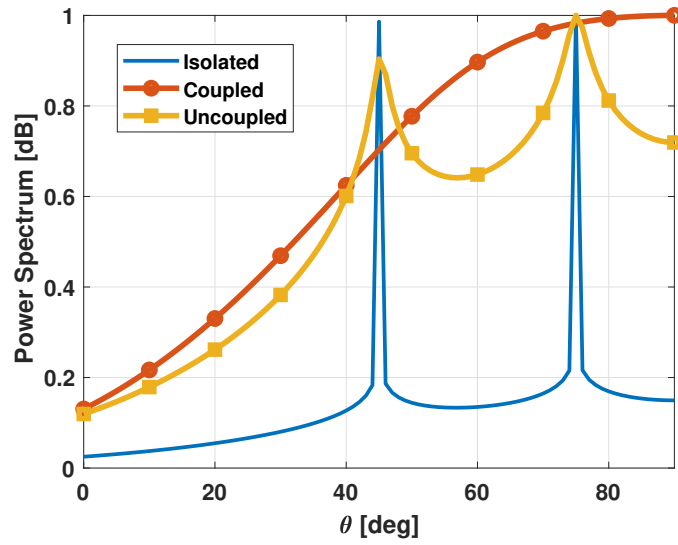


**Figure 2.16:** Spatial spectrum of MUSIC algorithm for DoA detection of two coherent signals from  $\phi = 90^\circ$ ,  $\theta_1 = 45^\circ$ ,  $\theta_2 = 75^\circ$ .

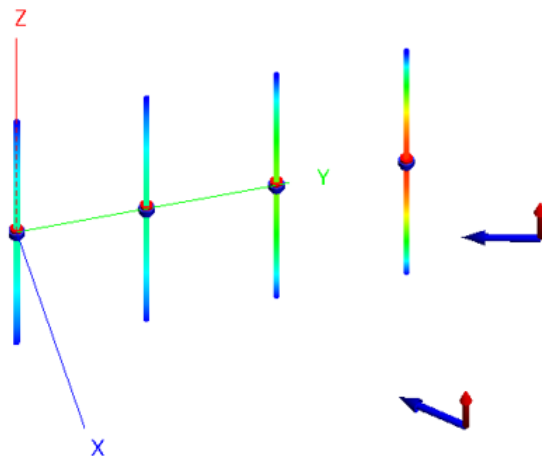


**Figure 2.17:** DoA estimation of two coherent sources for a fixed elevation  $\theta = 90^\circ$  and two different azimuth angles,  $\phi_1 = 45^\circ$  and  $\phi_2 = 75^\circ$ .

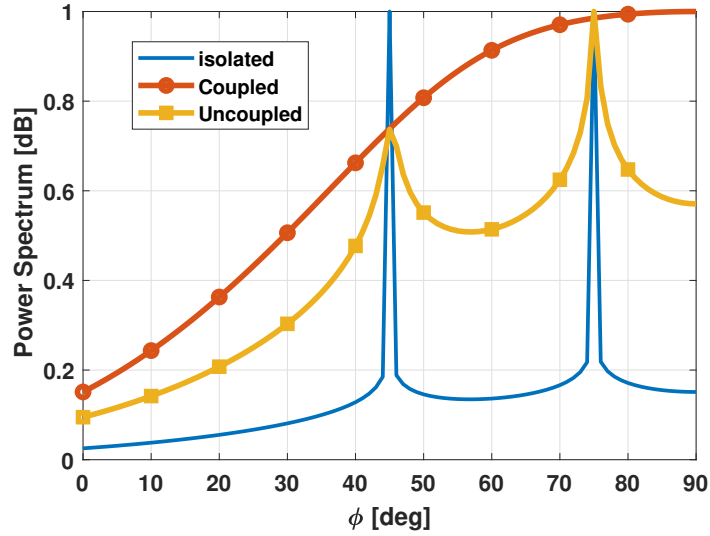


**Figure 2.18:** Spatial spectrum of MUSIC algorithm for DoA detection of two coherent signals from  $\theta = 90^\circ$ ,  $\phi_1 = 45^\circ$ ,  $\phi_2 = 75^\circ$ .

### 2.3.2.3. Four-element UCA

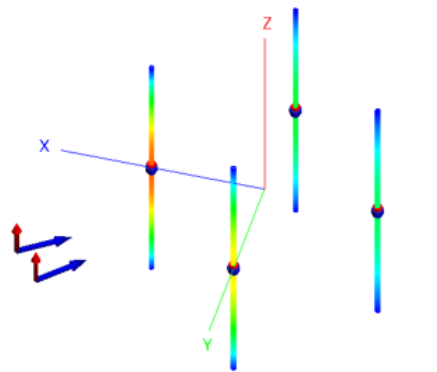


**Figure 2.19:** Four element UCA with radius  $\lambda/8$  excited by two coherent sources from  $\theta = 90^\circ$  and  $\phi_1 = 35^\circ$  and  $\phi_2 = 45^\circ$ .

In this example, the same dipole antennas were arranged in a UCA with a radius of  $\lambda/8$  and excited by a plane wave with  $\theta = 90^\circ$ ,  $\phi = 90^\circ$ . The coupled and isolated voltages were calculated and then the mutual impedances were computed which are compared in **Table 2.2** with [58]. It should be noted that the observed values are close in comparison however this is only one  $Z$  matrix for  $\theta = 90^\circ$  in case of Algorithm I. In other words, if we change the elevation angle we need to compute a different  $Z$  matrix. However, in Algorithm II only one matrix is required for all incident angles  $(\theta, \phi)$ . Also, these values were computed by using only one incident angle or  $2N$  measurements whereas in the previous algorithm at least 10 angles or  $20N$  measurements from different angles were

required.

**Table 2.2:** Received mutual impedance for a four element UCA.

Comparison	UCA		
	Algorithm II	$-19.36 + 12.32i$	$-11.4 + 15.69i$
Algorithm I [58]	$-19.16 + 12.35i$	$-11.39 + 15.73i$	$-19.08 + 12.00i$

**Table 2.3:** Isolated, coupled and compensated voltages for a four element UCA.

Ports	UCA		
	Isolated [mV]	Coupled [mV]	Uncoupled [mV]
$V_1$	$30.227 \angle 10.7^\circ$	$29.5 \angle 30.4^\circ$	$30.227 \angle 10.7^\circ$
$V_2$	$30.214 \angle 5.2^\circ$	$27.7 \angle 22.9^\circ$	$30.214 \angle 5.2^\circ$
$V_3$	$30.227 \angle -57.9^\circ$	$14.1 \angle -105.8^\circ$	$30.227 \angle -57.9^\circ$
$V_4$	$30.214 \angle -52.4^\circ$	$13.6 \angle -88.02^\circ$	$30.214 \angle -52.4^\circ$

As an example to show the accuracy of the decoupled voltages, the UCA was excited by two incident plane waves with  $\theta = 90^\circ$  and  $\phi_1 = 35^\circ$  and  $\phi_2 = 45^\circ$  as shown in **Figure 2.19**. The isolated, coupled and compensated voltages are shown in **Table 2.3**. It can be seen that mutual coupling has been successfully compensated since the isolated and compensated voltages are in very close agreement whereas the coupled voltages are very different in both magnitude and phase.

### 2.3.3. Contribution

Mutual coupling in receiving antenna arrays of thin wire dipoles has been compensated by using only one incident angle and  $2N$  measurements. It was observed that the mutual impedance depends only on the geometry of the structure and is independent of the incident angle

1. Mutual coupling in receiving antenna arrays of thin wire dipoles has been compensated for omni-directional antennas in ULA and UCA geometry and DoA was

computed as an example application.

2. There exists a unique  $Z$  matrix that can decouple the incident voltages for all  $(\theta, \phi)$ .
3. Only one incident angle i.e.,  $P = 1$  thus  $2N$  measurements are required to compute the decoupling matrix, whereas in previous works multiple measurements were required.
4. Mutual impedance is a property of the structure only and is independent of the incident angle of both  $\theta$  and  $\phi$ .
5. Unknowns reduced from  $N(N-1)$  to  $N-1$ .

**2.4. Algorithm III: A New Algorithm For Mutual Coupling Compensation For Receiving Antenna Arrays.**

$$\begin{bmatrix} \mathbf{Z}(\theta, \phi) \end{bmatrix} \begin{bmatrix} \mathbf{V}_c(\theta, \phi) \end{bmatrix} = \mathbf{K}(\theta, \phi) \begin{bmatrix} \mathbf{S}_i(\theta, \phi) \end{bmatrix}$$

[Decoupling Matrix] [Received Voltages with Coupling] = [Isolated voltages]

**Figure 2.20:** Algorithm III general statement.

The general form of Algorithm III is defined in **Figure 2.20**. The equation describes a direction dependent decoupling matrix which is a square matrix with dimensions  $N \times N$ , where  $N$  denotes the number of antennas in the array. The received coupled voltages and isolated voltages are a column vector of  $N \times 1$  dimensions. A complex constant  $K$  is defined which is also direction dependent. It was observed from experimental results that the decoupling matrix is dependant on the geometry of the array therefore, if a directional or omni-directional antenna is used the decoupling matrix will be the same if the spacing of the array is the same. Therefore, a general decoupling matrix for a ULA was mathematically modelled that can be pre-calculated provided the spacing  $d$  and number of antennas  $N$  is known. Similarly, in case of a UCA, a general decoupling matrix can be pre-calculated provided the radius of the circle and total number of antenna elements are known. This process can be extended to any arbitrary geometry. The elements of the decoupling matrix for three different cases were compared and it was observed that they are the same for all three cases. The experimental results for quasi yagi array, dipole array and simulation results for thin wire dipoles using MoM in MATLAB all result in the same decoupling

matrix. In other words, no measurement is required and the decoupling matrices can be computed beforehand for a received signal provided the incident angle is known. However, for other applications where angle information is not available, like DoA, then only a single isolated antenna measurement at the origin is required and its corresponding array measurements. Using a search based algorithm the DoA can be found easily using the constant  $K$  term. The decoupling matrix being direction dependent is in conformity with the latest research as mentioned by Friedlander [76]–[78], where it is clearly mentioned that the mutual impedance matrix of the antennas in the array derived by considering the array as a multiport network is a function only of the mutual impedances and the loads at the antenna terminals. This matrix is constant, i.e., independent of direction. In other words, given the array response for one particular loading (open-circuit, say), it is possible to calculate the response for any other loading using basic concepts from circuit theory. However, Mutual Coupling Matrix (MCM) or decoupling matrix in our case, which relates the analytic array manifold to the isolated manifold is direction dependant since it depends on the pattern of the array as well as the mutual impedances.

## CHAPTER 3

### 3. EXPERIMENTAL PART

#### 3.1. Algorithm I: An Experimental Study Of DoA Estimation With Mutual Coupling Compensation

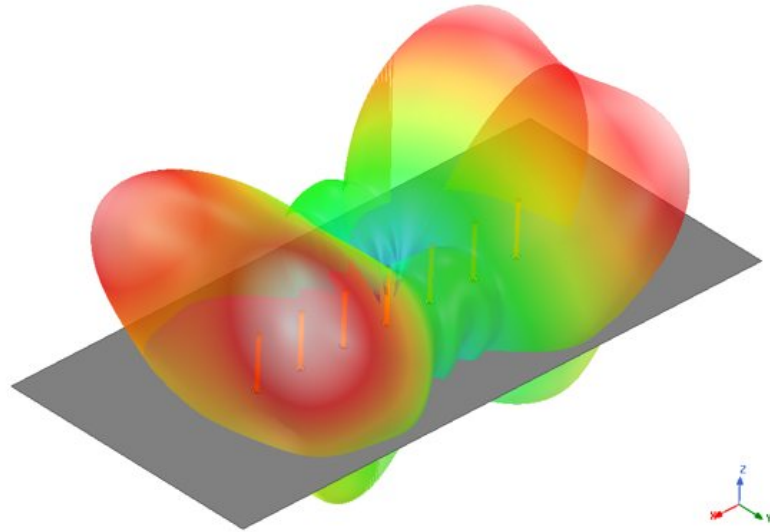
In this section, the measurement results of a seven-element ULA with monopole elements shown in **Figure 3.1** are presented as described in [59]. The monopole antenna is designed and optimized for 2.4 GHz. The individual array element length is  $0.24\lambda$  with diameter 1 mm and spacing between the individual elements is 25 mm ( $0.2\lambda$  at 2.4 GHz). An isolated monopole with these dimensions gave a return loss of  $-25$  dB. A wideband horn antenna was used (750 MHz to 18 GHz) as the transmitting source in the anechoic chamber. The DoA experiment was carried out using single and multiple incident sources for various angles in the azimuth in the xy-plane.

The horn source was placed a distance of 3 m away from the monopole array as shown in **Figure 3.2**. The array is shown in **Figure 3.3** and the isolated monopole is shown in **Figure 3.4**. Multiple isolated monopole antennas were constructed for the corresponding elements in the array in order to measure the isolated voltages. The experiment was carried out for a single incident source as well as multiple coherent sources with different angular separations as shown in **Figure 3.5** and **Figure 3.6**.

##### 3.1.1. Experimental procedure

The transmitting horn antenna and one of the monopole antenna elements of the seven-element monopole array were connected to Port 1 and Port 2 of the VNA respectively. The antenna array was placed inside the anechoic chamber. The measured S-parameter was related to the voltage as  $S_{21} = \beta/\alpha$ , where  $\alpha$  is the square root of the power emitted

a)



b)



**Figure 3.1:** A seven-element monopole ULA **a)** designed and simulated in CST, **b)** fabricated isolated monopole and monopole array.

by the transmitting horn and  $\beta = V/\sqrt{Z_o}$  is the square-root of the power received by a monopole element in which  $V$  is the terminal voltage of the monopole element and  $Z_o$  is the characteristic impedance of  $50 \Omega$ . The terminal voltage  $V$  can then be written as  $V = S_{21}\alpha\sqrt{Z_o}$ . As  $Z_o$  and  $\alpha$  are constants, it is clear that  $V$  is directly proportional to  $S_{21}$ .

Steps for measurement for single source DoA estimation:

1. A transmitting horn antenna and the monopole array are mounted inside an anechoic chamber. The horn antenna serves as the signal source. The position of the horn antenna is set at an angle with reference to the center of the monopole array. The horn simulates a signal source at 2.4 GHz coming from azimuth directions of  $\phi =$



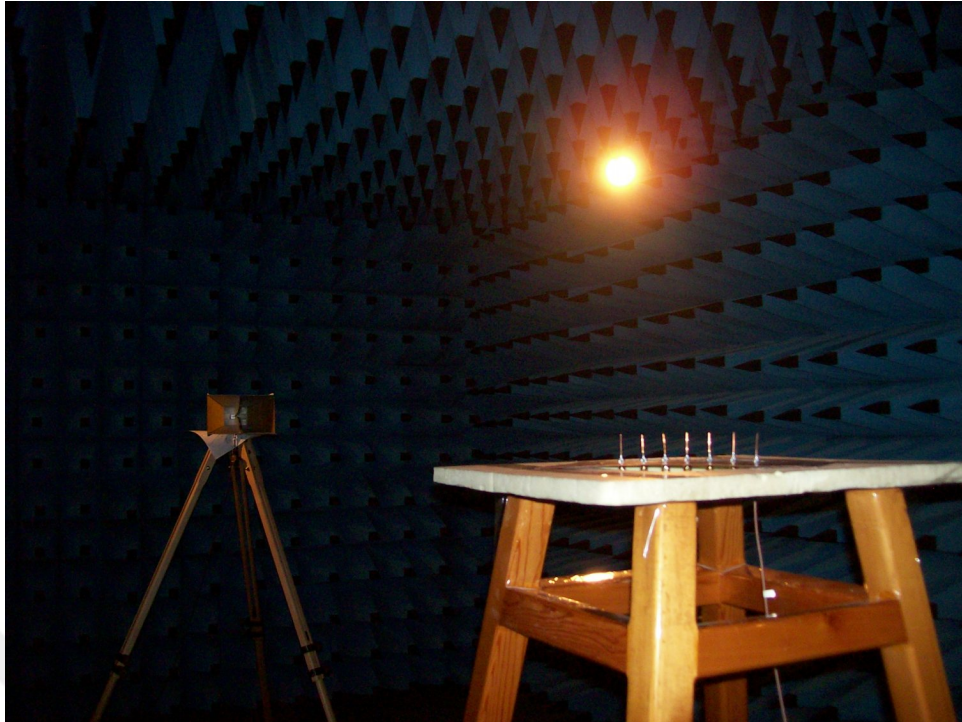


**Figure 3.2:** Measurement of a seven-element monopole array in an anechoic chamber under an external plane-wave using a horn antenna for DoA estimation.

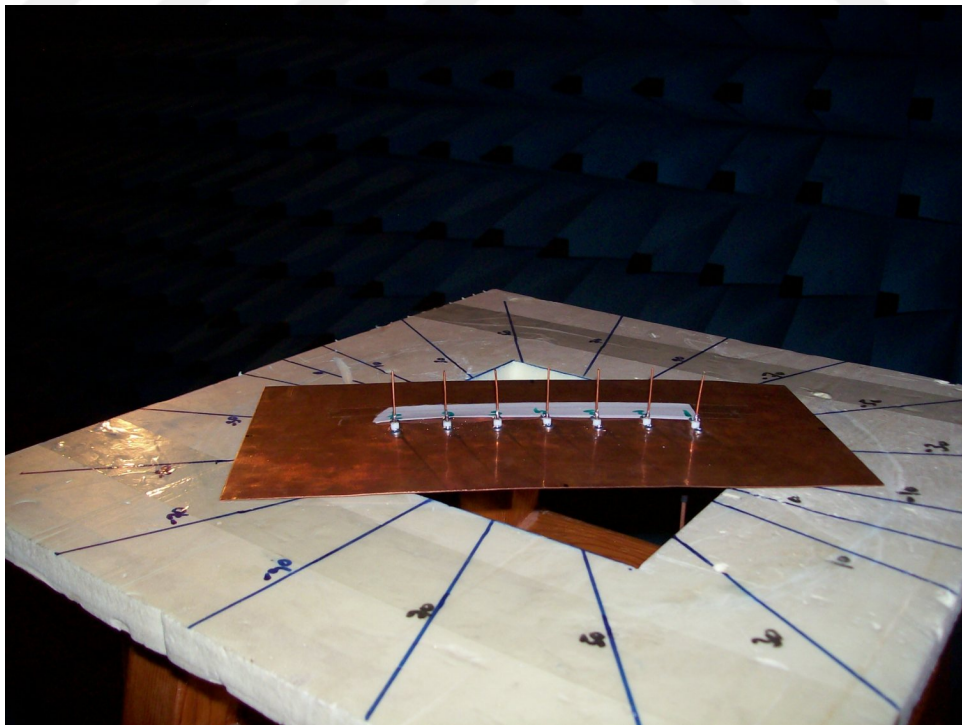


**Figure 3.3:** The fabricated seven-element monopole ULA as proposed in

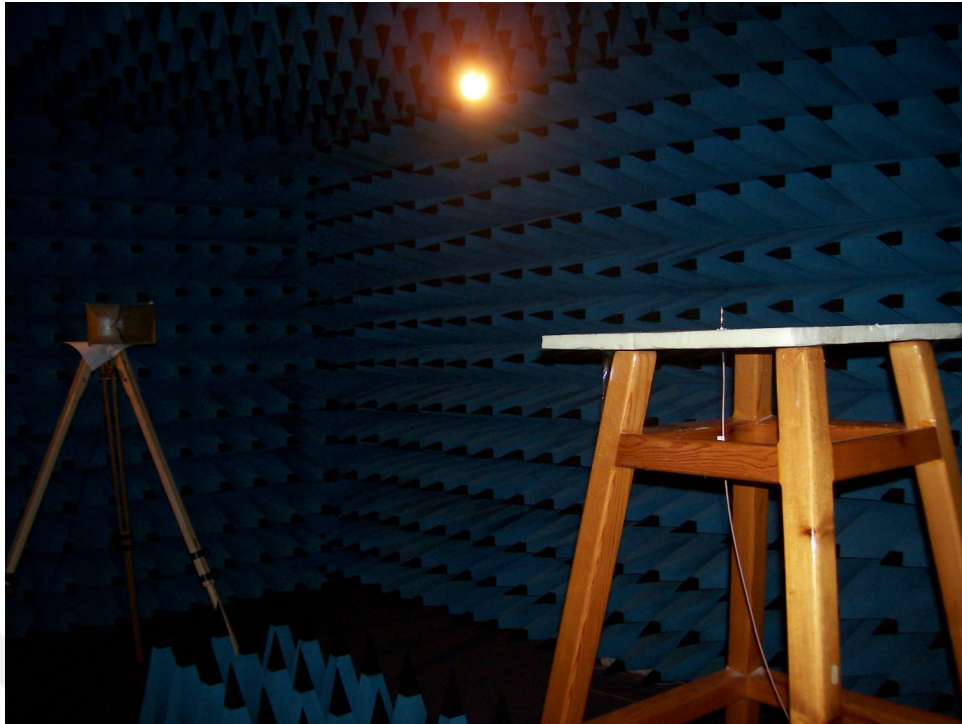


**Figure 3.4:** Measurement of an isolated monopole in an anechoic chamber under an external plane-wave using a horn antenna.



**Figure 3.5:** Multiple coherent source DoA estimation for seven-element monopole ULA.

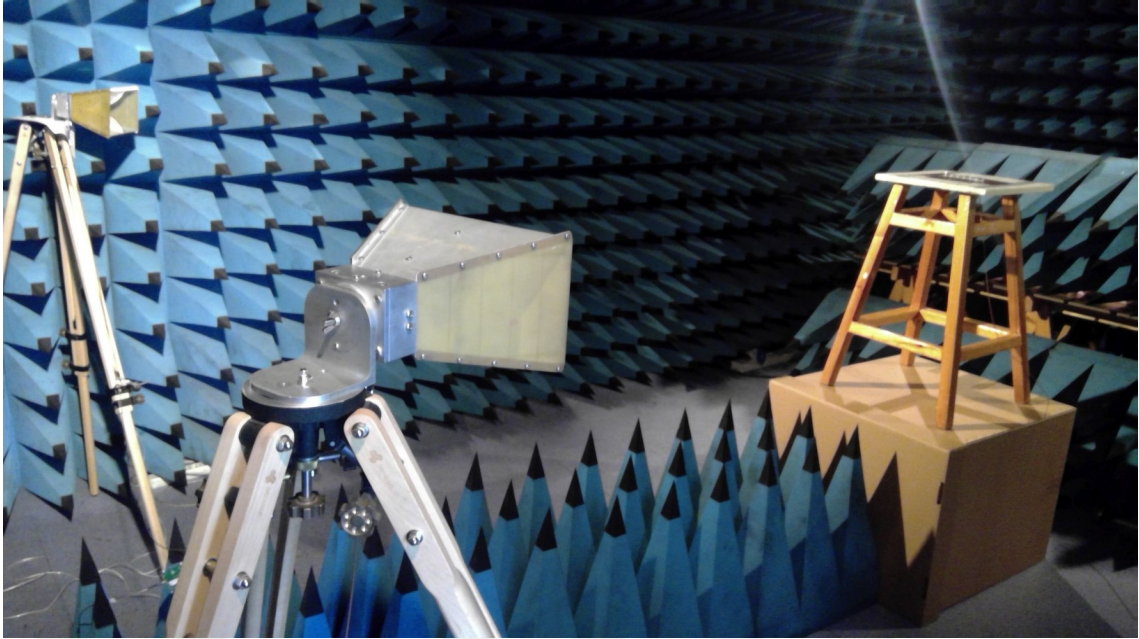


**Figure 3.6:** Multiple coherent source DoA estimation for seven-element monopole ULA for different source separation.

$-90^\circ$  to  $90^\circ$  and the elevation angle  $\theta = 90^\circ$  is fixed.

2. The horn antenna and the array are placed at the two ends of the anechoic chamber so as to ensure that the array is in the far-field region of the horn antenna. In our setup we kept the horn 3 m away from the antenna array at 2.4 GHz which corresponds to  $24\lambda$ .
3. Port 1 of the VNA is connected to the transmitting horn antenna.
4. Port 2 is connected to the antenna 1 of the antenna array while antenna 2 to 7 are terminated with a  $50 \Omega$  load.
5.  $S_{21}^{V_1}$  is equivalent to the voltage at antenna 1 in presence of mutual coupling. Next to measure is  $S_{21}^{V_2}$  when Port 2 is connected to antenna 2 while all others are terminated with a  $50 \Omega$  load. This process is repeated for all the seven antennas of the array.
6.  $S_{21}^{S_i}$  are the equivalent of the isolated voltages that are measured by using the single monopole antennas. We have four of them since our array is symmetric. The horn antenna and the array are connected from the outside of the anechoic chamber to the input and output ports of the VNA. The measured  $S_{21}$  parameter, which indicates the

relative power received by the monopoles, are then converted to a relative voltage quantity. In this way all the received voltages  $S_i$  ( $i= 1, 2, \dots, 7$ ) on the antenna elements are measured one by one by match terminating all other elements.

7. The above steps are repeated for all incident angles that were measured. The measured coupled and isolated voltages were then used to compute the  $Z$  matrix. The received voltages, the isolated voltages and the compensated voltages were given as an input to the MUSIC algorithm to find the DoA.

### **3.2. Algorithm II: Mutual Coupling Compensation In Receiving Arrays And Its Implementation On Software Defined Radios For DoA Estimation Application**

#### **3.2.1. Introduction**

In this section, an experimental verification of Algorithm II, as discussed in the previous chapter, is presented. The main application for this experiment is real-time DoA estimation with and without MCC considering receiving antenna arrays. Using Software Defined Radios (SDR), Direction Finding (DF) can be accomplished using the high-speed FPGA of the SDR or doing the computation offline on a host computer using Matlab, LabView or GNURadio [79]. SDR and Universal Software Radio Peripheral (USRP) are often used analogous, however, USRP paired with a host computer creates a complete SDR system. DoA estimation using SDR test-beds have been very popular in the past decade amongst researchers [79]–[85]. In DoA estimation using SDR, the receiving ULA are spaced  $\lambda/2$  or greater to avoid high coupling. The received voltages must be decoupled in order to estimate the accurate DoA. As shown in [79], [80] for a ULA of omni-directional antennas that are spaced  $\lambda/2$  apart the DoA can be estimated fairly accurately with an average deviation of  $1^\circ$ .

In this work, for the first time, mutual coupling has been compensated in real-time using SDRs for a four element ULA with inter-element spacing of  $\lambda/4$  in receiving case and DoA is estimated. First the decoupling matrix is computed using the method described in **Section 2.3**. The real-time received coupled voltages acquired by the SDRs are decoupled using this matrix. The compensated voltages are then given as an input to MUSIC algorithm to estimate the DoA. The implementation is done using NI USRP and LabView.

### 3.2.2. Proposed system design

The block diagram of the system is shown in **Figure 3.7**. A total of six USRPs are used along with OctoClock-G CDA-2990 and a Gigabit Ethernet Switch (GbE) connected to a host computer.

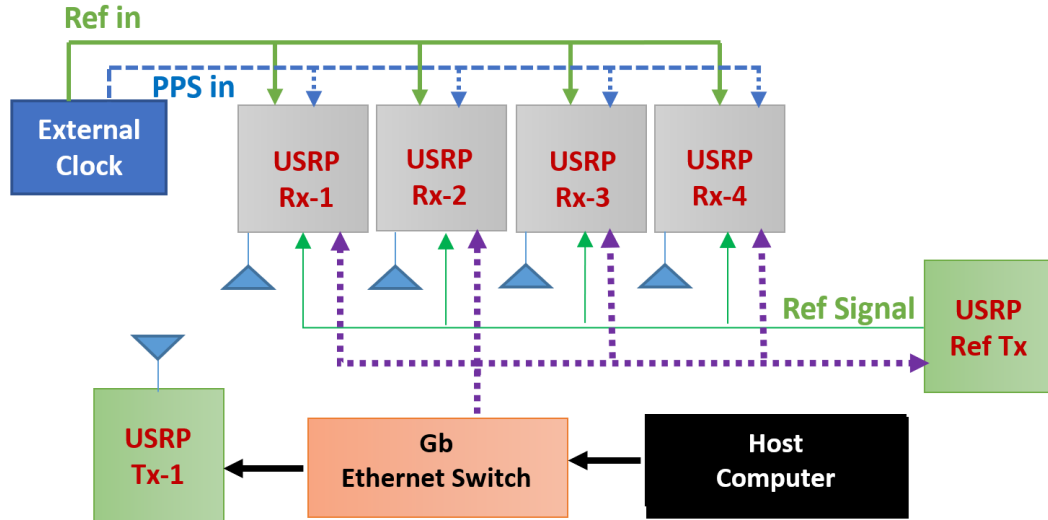


**Figure 3.7:** Block diagram of DoA estimation system.

Here, we use four NI USRP 2930 as RF receivers and NI-USRP 2932 and Ettus USRP B210 as RF transmitters. NI-USRP 2932 is used for calibration as Reference (Ref) signal in order to synchronize the phase of all the RF receivers. The phase is calibrated by physically wiring a 10 kHz tone Ref signal from the NI 2932 USRP TX1/RX1 port to each RX2 port of the four receiving USRPs using a four-way Wilkinson Power Divider. Phase synchronization is the most important part of the setup since this is the basic assumption for many DF algorithms. Four antennas are attached to each RX1/TX1 port of the four RF receivers. Furthermore, an external high accuracy time and frequency reference (Octoclock) is used for RF local oscillator synchronization and ADC timestamp alignment for the RF receivers. This can be achieved by connecting the 10 MHz reference clock and 1 PPS signal generated by the Octoclock to the RF receivers. Since, we have used the NI USRP 2930 which is a combination of (N210+WBX+GPSDO), therefore, the GPSDO must be manually disconnected in order to connect the external reference clock and external PPS ports of the four receiving USRPs with those of Octoclock, respectively. The second transmitting USRP B210 is used as the incident target source which transmits a tone of 100 kHz. The measurements were taken for a fixed elevation angle  $\theta = 90^\circ$  and

the distance between the transmitter (target) and receiving array was fixed at 1 m for optimum results [79]. The details of the equipment are mentioned in **Table 3.1**. We have

**Table 3.1:** Setup details for experimental test-bed for DoA application.

Item	Detail
SDR	NI USRP 2930 * 4, NI-USRP 2932*1, B210*1
Antenna	JCG401 GSM Antenna*4, LogPeriodic LP0965*1
Frequency-Time Module	OctoClock-G CDA-2990
Gigabit Ethernet Switch	Tplink TL-SG108
Carrier Frequency	2 GHz
Antenna Array Spacing	$\lambda/2$ , $\lambda/4$
MUSIC snapshot	3000
Sampling Rate	1 MHz
Platform	LabView

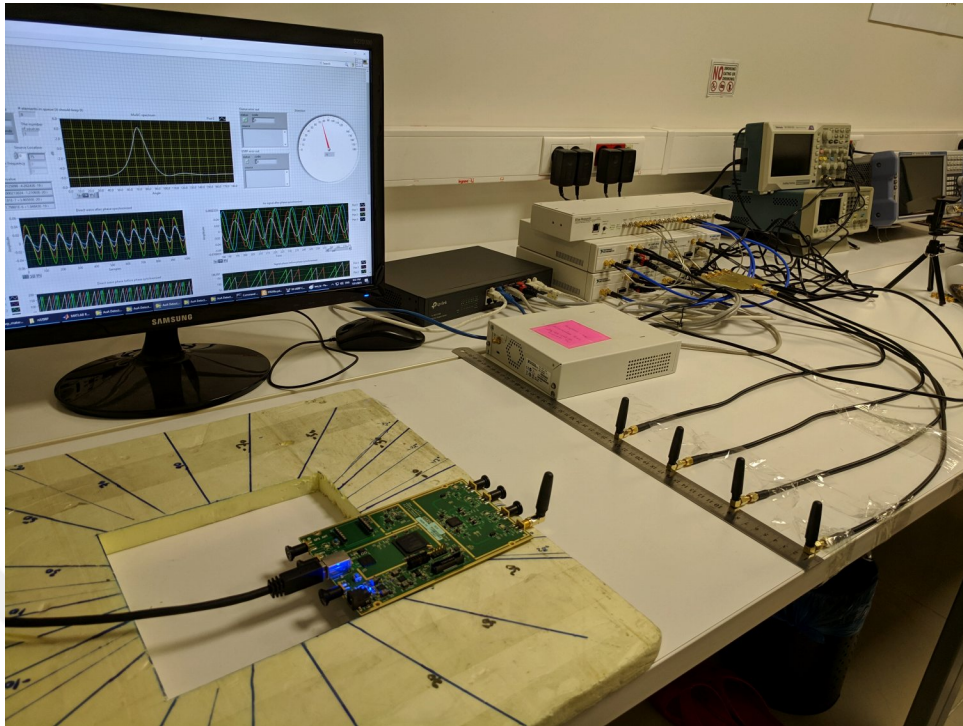
four receivers, NI USRP 2930, which have the WBX daughter boards whose frequency range is from 50 to 2200 MHz with a 40 MHz BW. The Ref Tx signal is generated by NI USRP 2932 which has SBX daughter board and its range is from 400 to 4000 MHz with BW of 40 MHz. The Tx USRP is Ettus B210 which is ranging from 70MHz to 6GHz with 56MHz BW. We used four GSM antennas for the receivers and Log Periodic as the transmitter antenna. The receiver gains were set to 30 dB and the transmitter gain was set to 60 dB for Ettus B210 whereas for the reference signal a gain of 10 dB was set and an attenuator was used before using the power splitter since this signal was sent directly over cable. The sampling frequency is 1 MHz and two arrays were used with spacing half and quarter wavelength. For DoA estimation using MUSIC, we were using a window of 3000 snapshots in LabView. The initial setup is shown in **Figure 3.8**. In order to make the setup mobile we came up with the setup shown in **Figure 3.9**. It should be noted that, all the measurements were taken indoors in the Istanbul Medipol University (IMU) campus

building corridor which is a noisy atmosphere with multi-paths, standing waves, and interference. Hence, the readings are more realistic and the compensation in such a scenario shows the robustness of the applied method.

### 3.2.3. Mutual impedance measurements

In this section, the decoupling matrix is measured for a ULA of four antennas at 2 GHz with a spacing  $d = \lambda/4$ . We first measure the isolated voltages received by the four element ULA using a VNA by measuring the S-parameters ( $S_{21}$ ) of each antenna by removing all other antennas for the isolated case. A Log Periodic antenna was placed 1 m away to act as a plane wave source with  $\theta = 90^\circ$  and  $\phi = 90^\circ$ . The setup is shown in **Figure 3.10**. For each of the array elements, the isolated voltage is measured using only one incident angle. Similarly, the received coupled voltages are measured for the array as shown in **Figure 3.11**. In this case, the voltage is measured when all other elements are match terminated in a  $50 \Omega$  load. In total,  $2N$  or 8 measurements are required for a single angle,  $\theta = 90^\circ$  and  $\phi = 90^\circ$ , four isolated measurements and four measurements in the array configuration. By applying the method explained in **Subsection 2.3.1**, we find the decoupling matrix, which was used in LabView to decouple the received voltages at the RF receivers. These measurements were performed separately but in the same noisy environment as in **Subsection 3.2.2**.

a)



b)

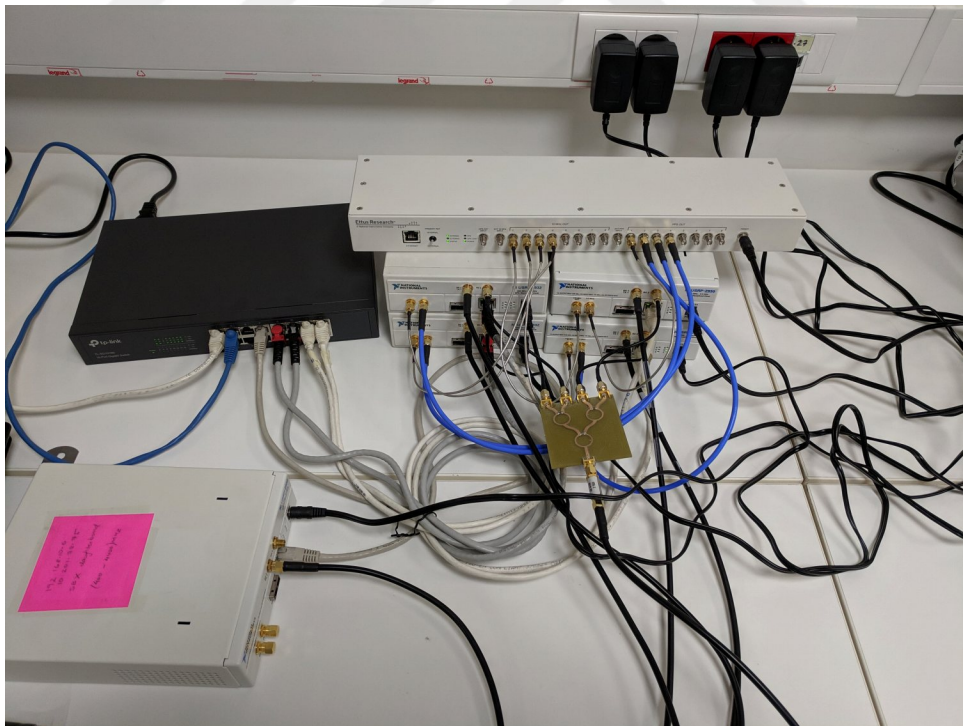


**Figure 3.8:** Initial experimental test-bed for DoA estimation (a) complete setup (b) zoomed in.



a)



b)

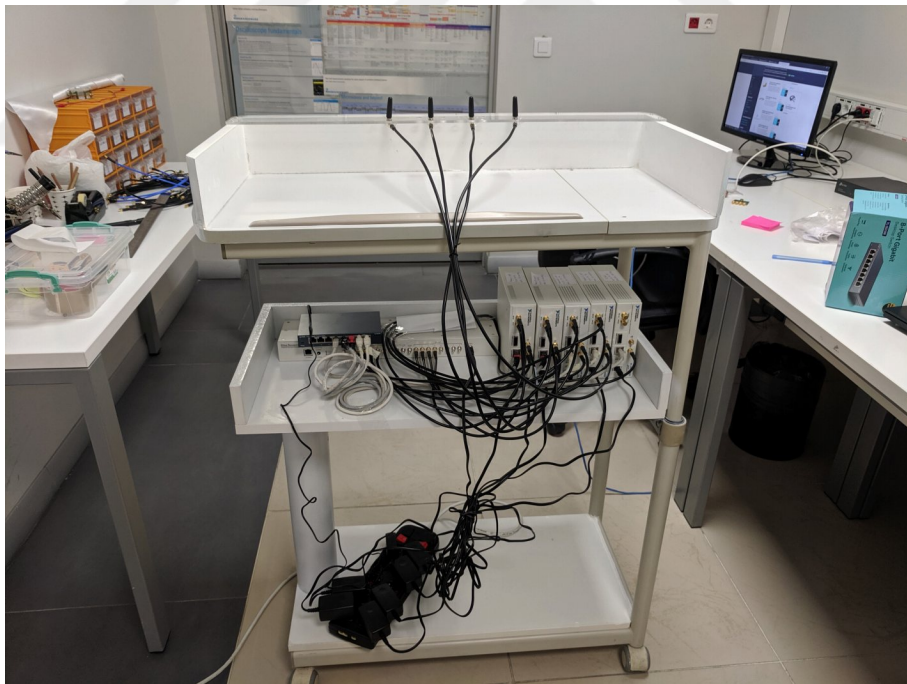
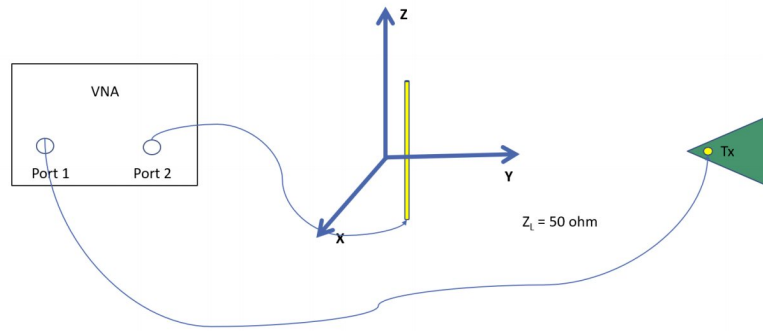
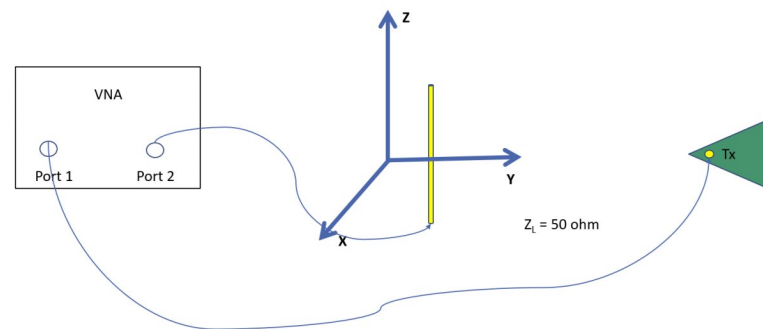


**Figure 3.9:** Final experimental mobile setup for DoA estimation (a) frontside (b) backside.

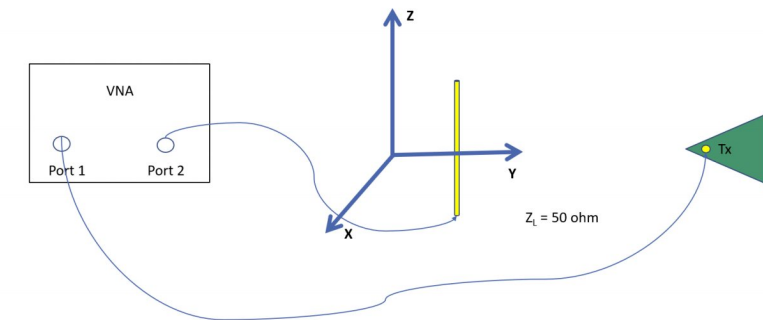
a)



b)



c)



d)

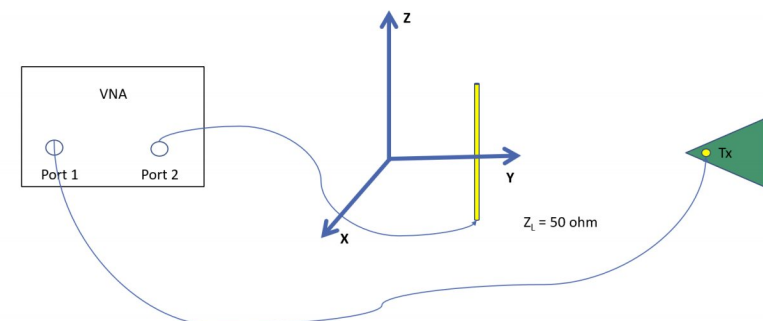


**Figure 3.10:** Setup for measuring the isolated voltages **a)** antenna 1, **b)** antenna 2, **c)** antenna 3, **d)** antenna 4.

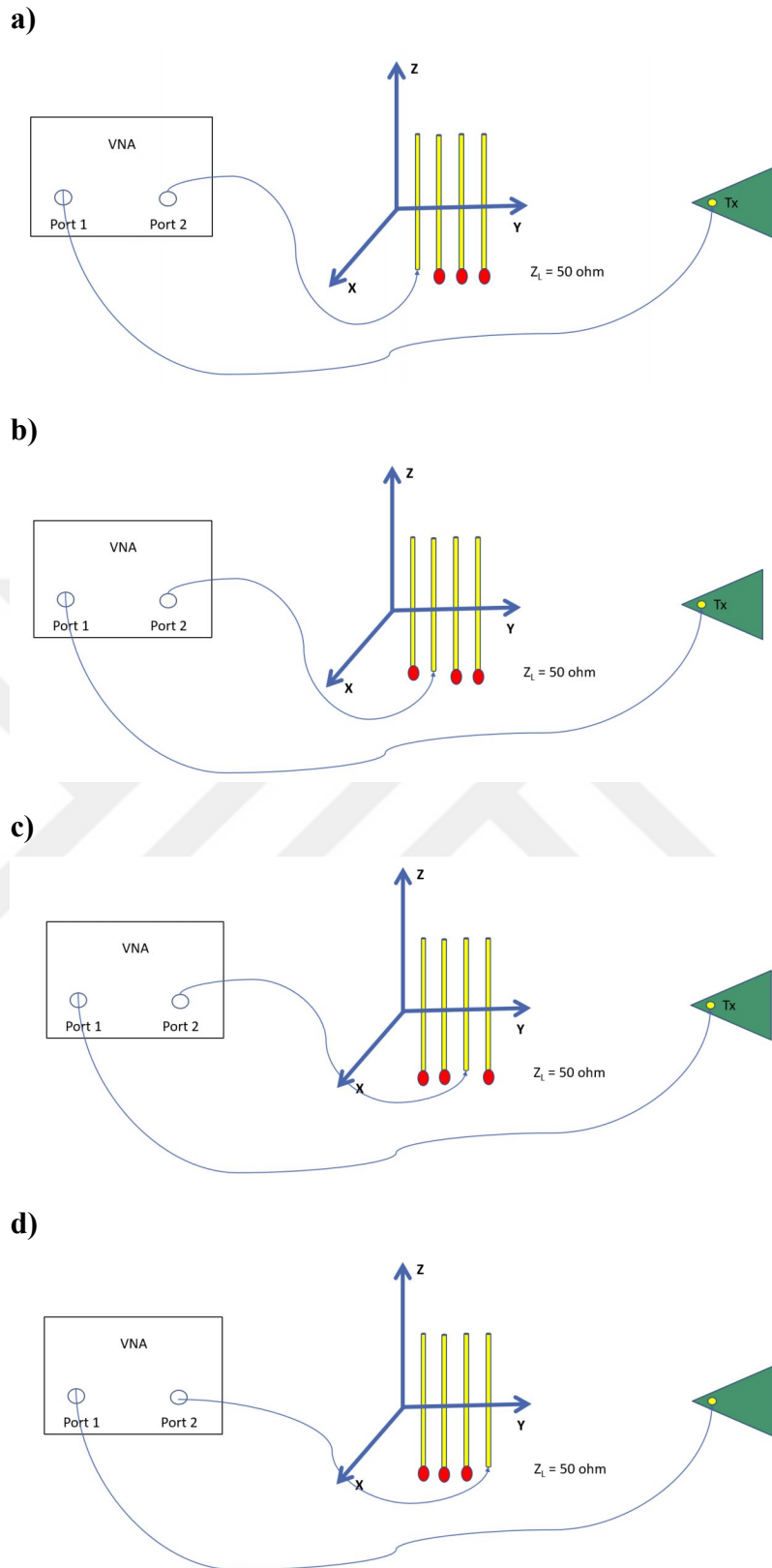


**Figure 3.11:** Setup for measuring the coupled array voltages **a)** antenna 1, **b)** antenna 2, **c)** antenna 3, **d)** antenna 4.

### 3.2.4. Experimental procedure: DoA estimation

The complete DoA experimental measurement test-bed can be seen in **Figure 3.12** and **Figure 3.13**. In **Figure 3.12**, we have a Log Periodic antenna as the Tx antenna which is connected to the Ettus B210 labeled as USRP Tx-1. The carrier frequency is 2 GHz and a 100 kHz tone frequency is transmitted. On the receiver side four GSM antennas in ULA are spaced half a wavelength in the first case and quarter wavelength apart for the second case. The angle is measured from the +ve x-axis with Antenna 1 as the reference antenna as shown in **Figure 3.13**. These four antennas are connected to four different USRPs labeled as RX 1 to Rx 4. The NI USRP 2930 which has been used for these four receivers has two ports that can be used for receiving. One port is connected to the antenna and the second port of all these USRPs are connected to a 10 kHz Ref signal which is generated by a 5th USRP 2932 labeled as Ref Tx using a 1 to 4 splitter. This signal

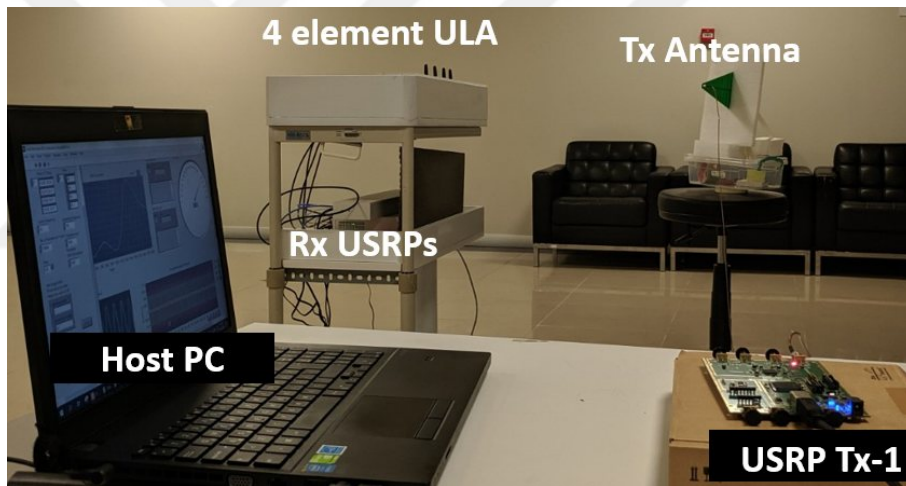


**Figure 3.12:** The complete experimental setup for DoA estimation.

is used to remove the phase ambiguity between the USRPs. The operation of any phased array system requires RF local oscillator synchronization and ADC timestamp alignment. In this experiment the local oscillator synchronization among the NI USRPs is achieved using external reference clock. Timestamp synchronization is achieved using external PPS signal. We have the OctoClock which provides the external ref clock as well as the PPS signal and all the four USRPs are connected to it. It should be mentioned that same length cables are required for the connections in this setup to mitigate the phase offset. All the five USRPs are connected to the host PC using Gigabit Ethernet. The Tx USRP is directly connected to the host PC since Ettus B210 is a USB based plug and play USRP. WBX RF

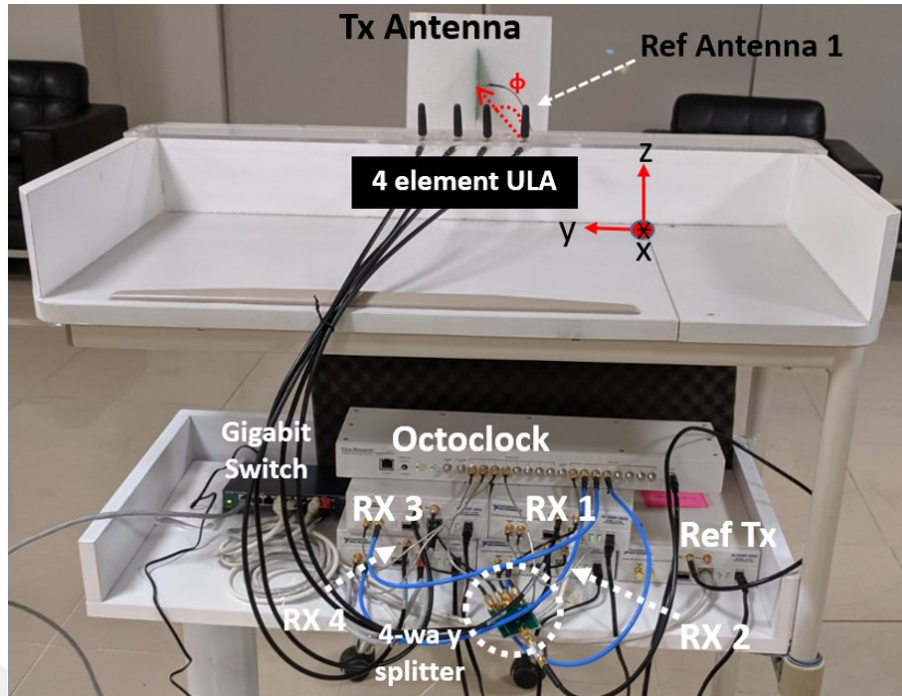


**Figure 3.13:** Receiver part of the experimental setup for DoA estimation.

daughterboards have a  $\pm 180^\circ$  phase offset for the LO. Synchronization works well in the NI USRPs in terms of effectively eliminating relative phase shift over time. However, every time a re-tune command is sent to the USRP by changing the carrier frequency or sampling rate there is a new phase ambiguity between the boards. Therefore a calibration procedure is required every time the system is restarted or any re-tune command is used. NI LabView is used as the software platform in this experiment. We apply two different tones ( using Single-SideBand Suppressed-Carrier AM modulation ) one for the Tx 1 B210 (100 kHz) and one for Ref Tx (10 kHz). One is received over the air whereas the other is received directly via cable. At the receiver we filter these two signals digitally using a high pass and low pass filter respectively. The Ref synchronization signal is used to evaluate the channel phase offset among different receive antennas. The phase difference w.r.t antenna 1 is then compensated for all receivers and we align the target signals in both phase and gain. This effectively eliminates gain and phase uncertainties between channels due to the NI USRP boards. The received signal before and after phase synchronization are shown in **Figure 3.14** and **Figure 3.15**. Here, we see gain and phase alignment after the calibration has been done. The most important calibration for phased array system is the phase calibration since all of the receivers need to receive the signal at the same timestamp. Therefore, before and after phase synchronization shows that the system has

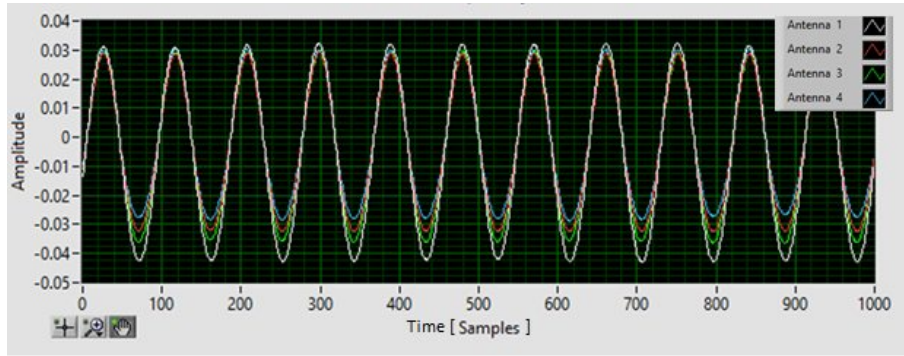


**Figure 3.14:** Received signal amplitude after calibration.

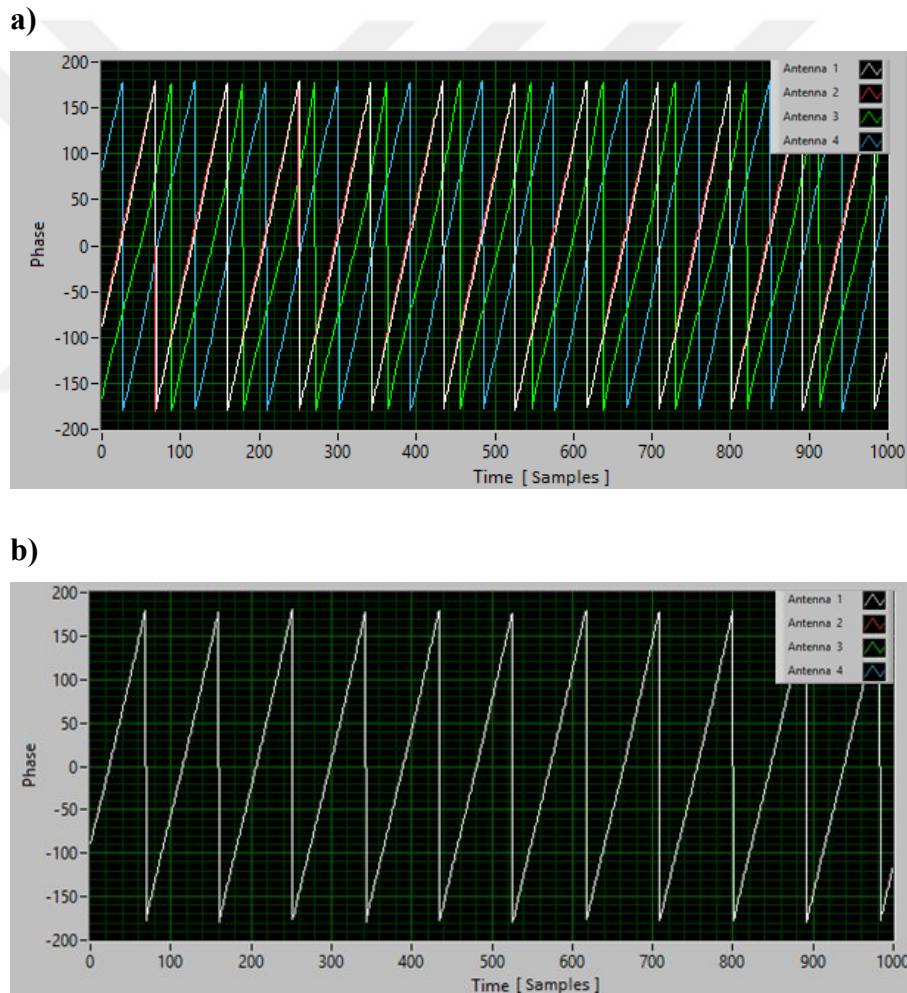


**Figure 3.15:** Received signal. (a) before phase calibration (b) after phase calibration.

been successfully synchronized and calibrated. Till this step we were trying to accomplish the calibration. After the NI USRPs are synchronized in terms of phase and gain, MUSIC algorithm is used for detecting the AoA of the received signal. For this, the received I/Q data is divided into different frames or snapshots of 3000. Each frame is then processed by MUSIC, and then the DoA is estimated. The input to MUSIC is the array setup, I/Q frame of 3000 samples, operating frequency and threshold. A threshold is set for the detection of the received signal strength which depends on the the distance of the receiver from the transmitter. After finding the covariance matrix for the received coupled signals for each frame and their corresponding eigenvalues the MUSIC spectrum can be easily obtained by taking the dot product of the array manifold vector with the noise eigenvalues. Since the signal subspace and noise subspace are orthogonal, we expect the value to be very close to zero. By taking the inverse of this a peak is resulted which gives us the DoA estimation. In the compensated case, the received frame, after filtering and synchronization process, is first multiplied by the decoupling matrix and then given as an input to the MUSIC algorithm.

### **3.3. Algorithm III: An Experimental Setup For Mutual Coupling Compensation In Receiving Antenna Arrays Using Xilinx® Zynq®-Based FPGA And An Analog Devices™ FMCOMMS5 Radio For DoA Application**

#### **3.3.1. Introduction**

In the previous section, an experimental test-bed was developed to test Algorithm II. The main limitation of this algorithm was that it was limited to omni-directional antennas and the experimental test-bed was costly and a lot of equipment was required in building it which made it less favorable for practical applications. In this section, using a completely new approach an algorithm has been developed which not only takes care of the limitation of a specific antenna array type but any arbitrary antenna array can be tackled using this algorithm. Furthermore, a mathematical model has been developed for the decoupling matrix which can help us predict the matrix just depending on the geometry of the array whether it is a ULA, UCA or arbitrary shaped array. The second contribution in this work is the development of a new and compact experimental test-bed for MCC. This setup can be used as a standalone system and can be reconfigured for different applications making

it suitable for developing customized solutions. The versatility of deploying open-source software adds further opportunities for realizing end-to-end complete system design.

### 3.3.2. Experimental setup

In this experiment we estimate the direction of arrival (DoA) of an incident signal using a new hardware setup based on software defined radios. Furthermore, we compensate the mutual coupling between the antennas and estimate the DoA using multiple estimation algorithms available in the literature. Directional and omni-directional antennas were deployed with different spacings ranging from  $0.24\lambda$  to  $0.6\lambda$ . A study was done on the effect of the array spacing and DoA estimation. This is the first time real-time DoA is computed indoors with full accuracy for both directional and omni-directional antenna arrays after mutual coupling compensation without using an anechoic chamber.

#### 3.3.2.1. Transmitter

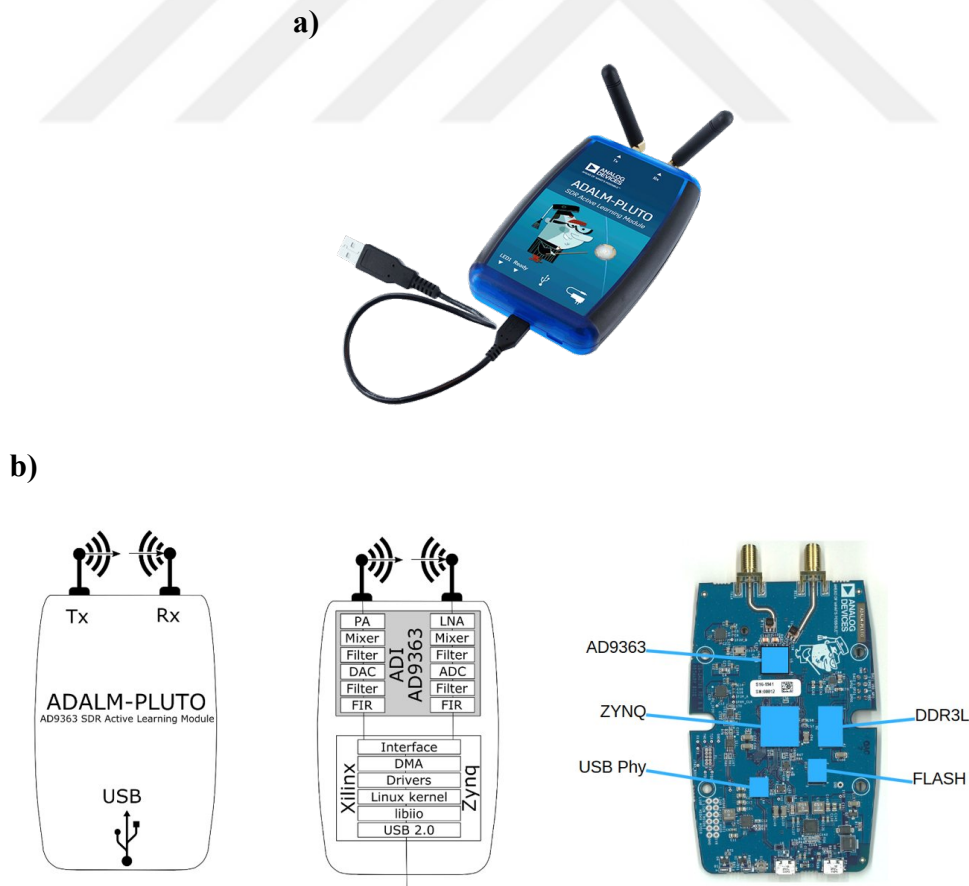


**Figure 3.16:** SDR a) Adalm-Pluto, b) block diagram.



The transmitter is an ADALM-Pluto SDR as shown in **Figure 3.16a**. ADALM-Pluto is based on the AD9363 IC by Analog Devices, it offers one receive channel and one transmit channel which can be operated in full duplex, capable of transmitting or receiving RF analog signals from 325 to 3800 MHz, at up to 61.44 Mega Samples per Second (MSPS) with a 20 MHz bandwidth. The detailed configuration of Pluto SDR is shown in **Figure 3.16b**. These are the default settings with which this is shipped with, however, these default settings can be easily changed. The AD9363 IC has a 2x2 transceiver however the second channel has not been enabled on the Pluto SDR board. Pluto SDR is based on the AD9363 which is identical to the higher end AD9364. The Pluto SDR can be tricked into seeing an AD9364 chip simply by changing some device strings by a simple hack via a USB serial connection. This increases the frequency range from 70 MHz to 6 GHz as well as the bandwidth is increased from 20 MHz to a range of 200kHz to 56 MHz. Pluto

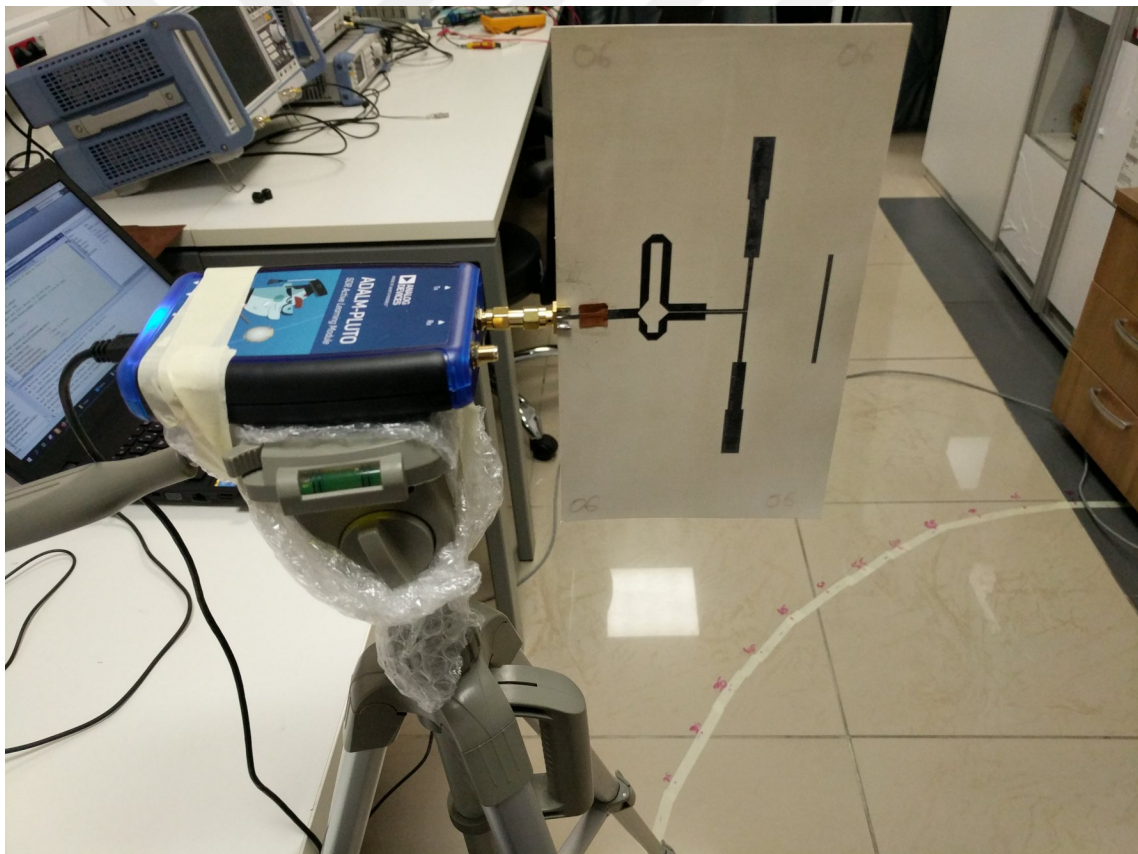


**Figure 3.17:** Transmitting setup consisting of Pluto SDR and quasi yagi antenna.

SDR is based on Zynq 7000 SoC and by default the second processor is locked which can also be unlocked by a simple hack just by establishing a Secure Shell Protocol (SSH) or serial connection to the Pluto SDR. Therefore, we end up with a dual core A9 Cortex

ARM processor as well as an increased RF range and bandwidth which is equal to an Ettus B200 with same specifications but four times less the price. This small portable plug and play SDR that fits in the palm of your hand can be easily modified both in hardware and software which leads to a great platform for open source customized development.

In this setup we have a quasi yagi antenna acting as the transmitter powered by an ADALM-Pluto SDR as shown in **Figure 3.17**. The transmitter specifications for the setup is shown in **Table 3.2**. A monotone sine wave with a frequency of 10kHz is transmitted at 2.468 GHz which acts as the source. The sampling rate is 1 MHz and the transmitted power is 0 dBm. The transmitter is mounted on a tripod stand with a printed quasi yagi Antenna attached to the Tx port of the SDR using a male-male SMA connector only. The transmitter is located on a semi-circle which has been calibrated from  $-90^\circ$  to  $+90^\circ$  with  $0^\circ$  at the origin as shown in **Figure 3.18**. There are a total of 18 angles in one quarter of the semicircle by using a  $5^\circ$  angle division. The radius of the semi-circle is  $20\lambda$ .

**Table 3.2:** System specifications for the transmitter.

Item	Details
SDR	ADALM-Pluto
Antenna	Quasi yagi
Center frequency	2.468 GHz
Tone frequency	10 kHz sinusoid
Sampling rate	1 MHz
Gain (Attenuation)	0 dB ~ +7 dBm Range = 0 to 89 dB
Platform	MATLAB USB 2.0



**Figure 3.18:** DoA testing setup consisting of the transmitter placed on a semi-circle with angles from  $-90^\circ$  to  $+90^\circ$  with  $5^\circ$  spacing and origin defined at  $0^\circ$ .

### 3.3.2.2. Receiver

At the receiver side as shown in **Figure 3.19**, we have a four element quasi yagi ULA which has a spacing  $d=0.2479\lambda$ . The receiver setup specifications are shown in **Table 3.3**. The four element array is connected to EBZ-FMCOMMS5 RF Front End (RFFE) board which is a 4x4 MIMO platform with two AD9361 ICs that contain two transmitters and two receivers each, ranging from 70 MHz to 6 GHz and has a channel bandwidth ranging from 200kHz to 56 MHz. The platform is connected to a Xilinx Zynq FPGA ZC706 using an FMC connector as shown in **Figure 3.20**. The Zynq®-7000 family is based on the Xilinx SoC architecture. This product integrates a dual-core ARM® Cortex™-A9 based processing system (PS) and 28 nm Xilinx programmable logic (PL) in a single device. The ARM Cortex-A9 CPUs are the heart of the PS and also include on-chip memory, external memory interfaces, and a rich set of peripheral connectivity interfaces.

**Table 3.3:** System specifications for the receiver.

Item	Details
SDR	AD FMCOMMS5 Radio + ZC706 Xilinx FPGA
Antenna array	Quasi yagi ULA N= 4
Array spacing	$0.24\lambda$
Samples per frame	4000
Frame time	4 ms
Total frames	1251
AGC Mode	Manual 30 dB Range = -10 to 76 dB
Platform	MATLAB GbE LAN

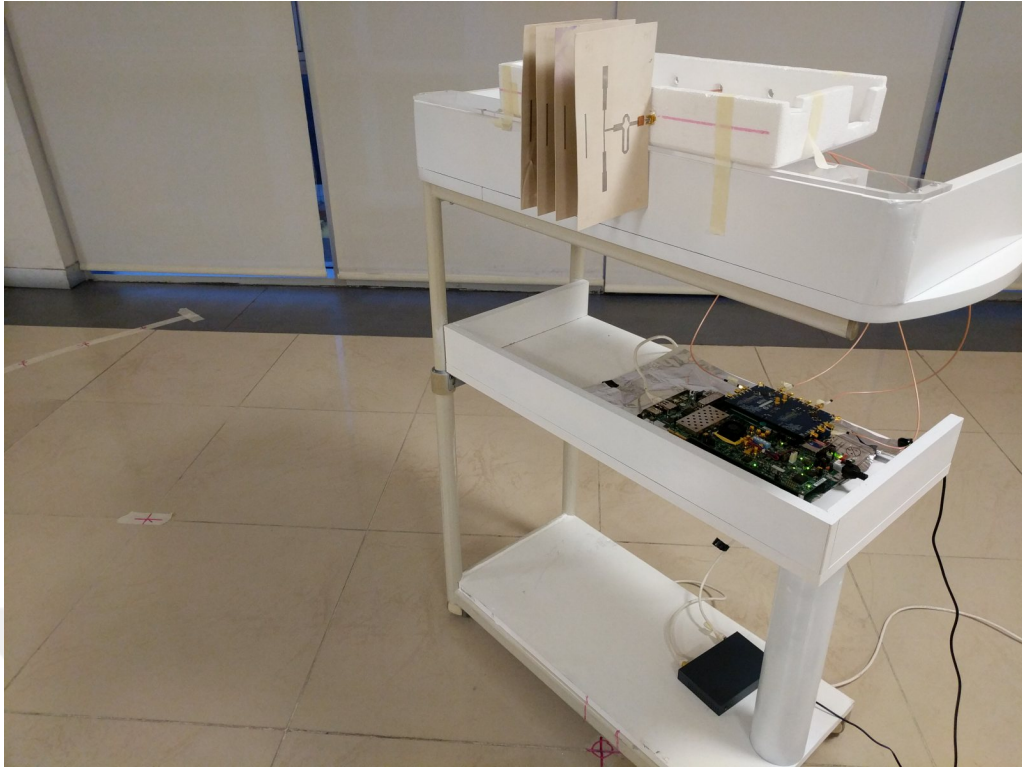


**Figure 3.19:** The receiving setup consists of a four element quasi yagi array with  $0.2479\lambda$  spacing connected to Xilinx Zynq ZC706 FPGA with Analog Devices FMCOMMS5 RFFE Module.

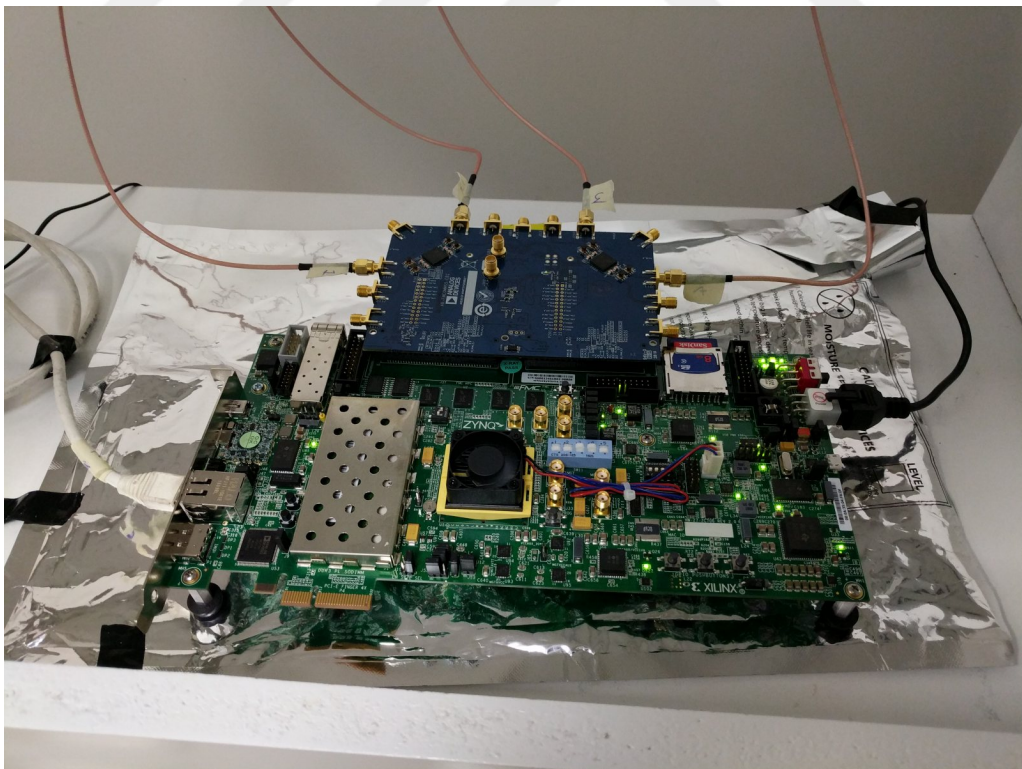


**Figure 3.20:** Xilinx Zynq ZC706 FPGA with Analog Devices FMCOMMS5 RFFE Module.

### 3.3.2.3. Calibration

In order for the Xilinx Zynq radio to interface with MATLAB, a bootable SD card with a linux distribution must be made and then booted using it. The RFFE card FMCOMMS5 is attached using an FMC connector. The radio is interfaced to MATLAB using LAN therefore an IP must be set first. This can be set by accessing the Zynq Radio via the serial port using an ssh terminal and then setting up a permanent IP. Before the experiment is

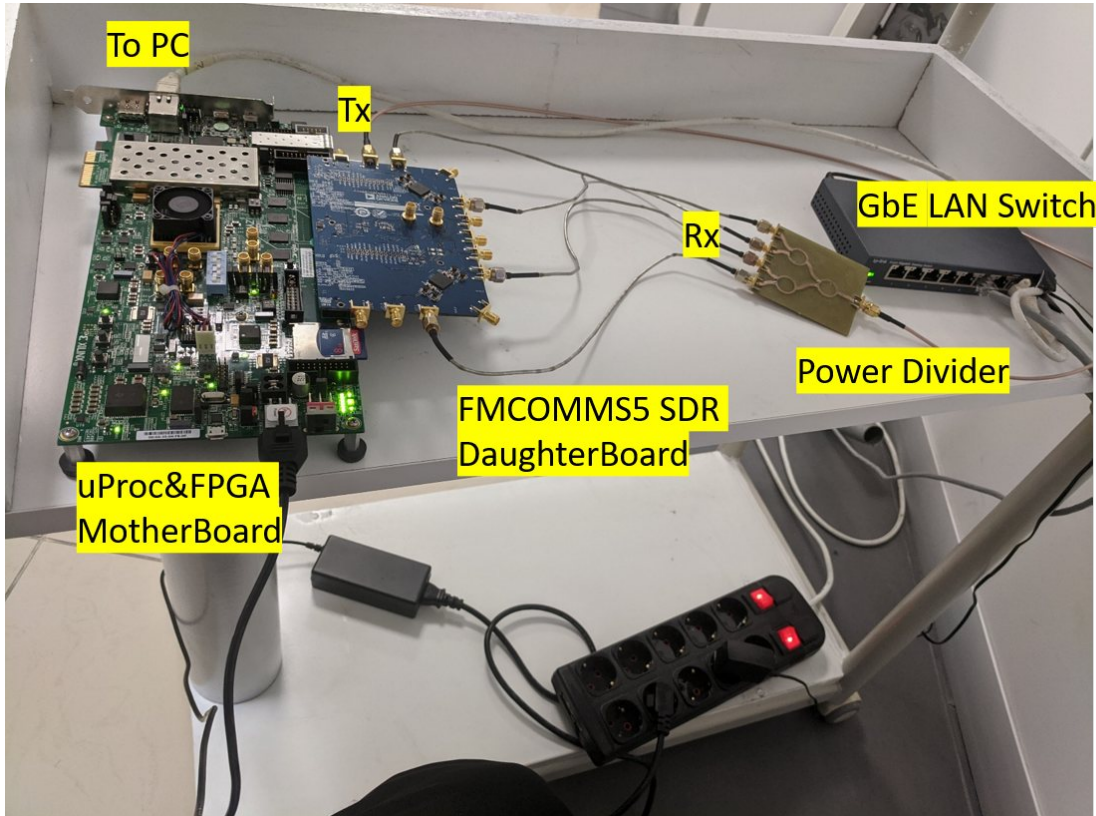


**Figure 3.21:** Setup for the initial calibration of the FMCOMMS5 SDR.

started, the RFFE FMCOMMS5 must be calibrated so that each of the four receivers are in-phase. For this purpose, a 1 to 4 power splitter is used with same length of cables. The input to the power splitter is taken from Tx1 port of the board and the four outputs of the splitter are connected to Rx1 to Rx4 ports. Using the IIO Scope, which is an open-source software by Analog Devices, the calibration is performed by doing a multi-chip synchronization (MCS). The details are provided in [86]. The calibration setup is shown in **Figure 3.21** where as the successful calibration of the four receivers LO is shown in **Figure 3.22** and **Figure 3.23**. Once the board is calibrated, another calibration step is further to be performed. The transmitter is placed at the origin at  $0^\circ$  and Pluto SDR starts transmitting using MATLAB to generate the sinusoidal signal in baseband which is then

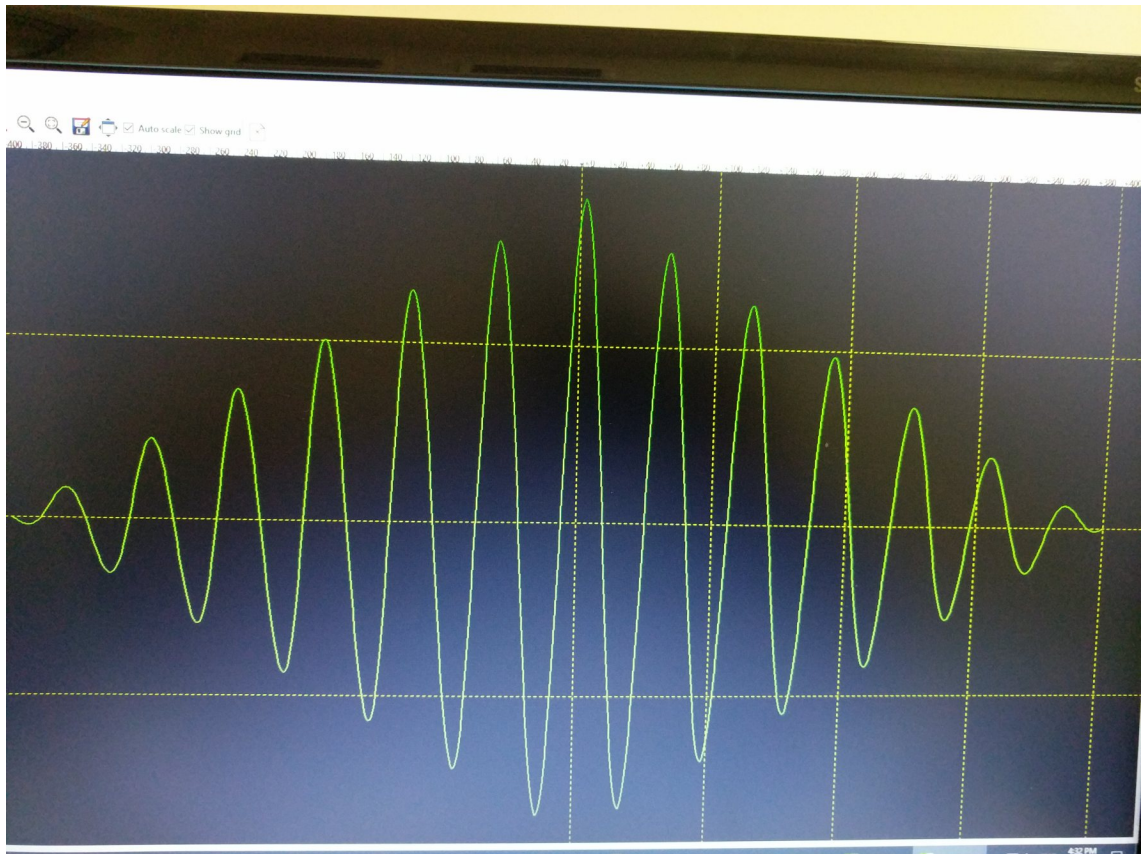


**Figure 3.22:** IIO Scope by Analog Devices showing the cross correlation of the receiving channels LO phase after calibration.

upconverted to RF via the Pluto SDR. By using a spectrum analyzer (SA) the received power is measured near the receiving array which was -35 dBm. After measuring and validating the 10kHz sinusoidal signal on the SA and making sure that the signal is not overlapped by the WiFi routers nearby, the receiver is setup to receive the transmitted signals. MATLAB is used for both the transmitter and receiver software interface. After the transmitter is setup and running, in the receiving side we configure the four receivers by setting the channel mapping w.r.t antenna positions in the array, the base band sampling rate, center frequency, gain level of each receiver, samples per frame and the data type. The sampling rate is kept the same as the transmitter to 1 MHz and 4000 samples per frame and the receiver gain is set to 30 dB manually. The second part of the calibration involves the receiver to set its origin which is why the transmitter is kept at  $0^\circ$  in the beginning of the experiment. First we estimate and correct the phase offset between all the receiver channels. This is accomplished by amplitude normalization for each channel followed by calculating the phase difference for channels 2, 3 and 4 w.r.t., channel 1. In order to phase sync all signals, IQ rotation is performed by calibrating the phase between

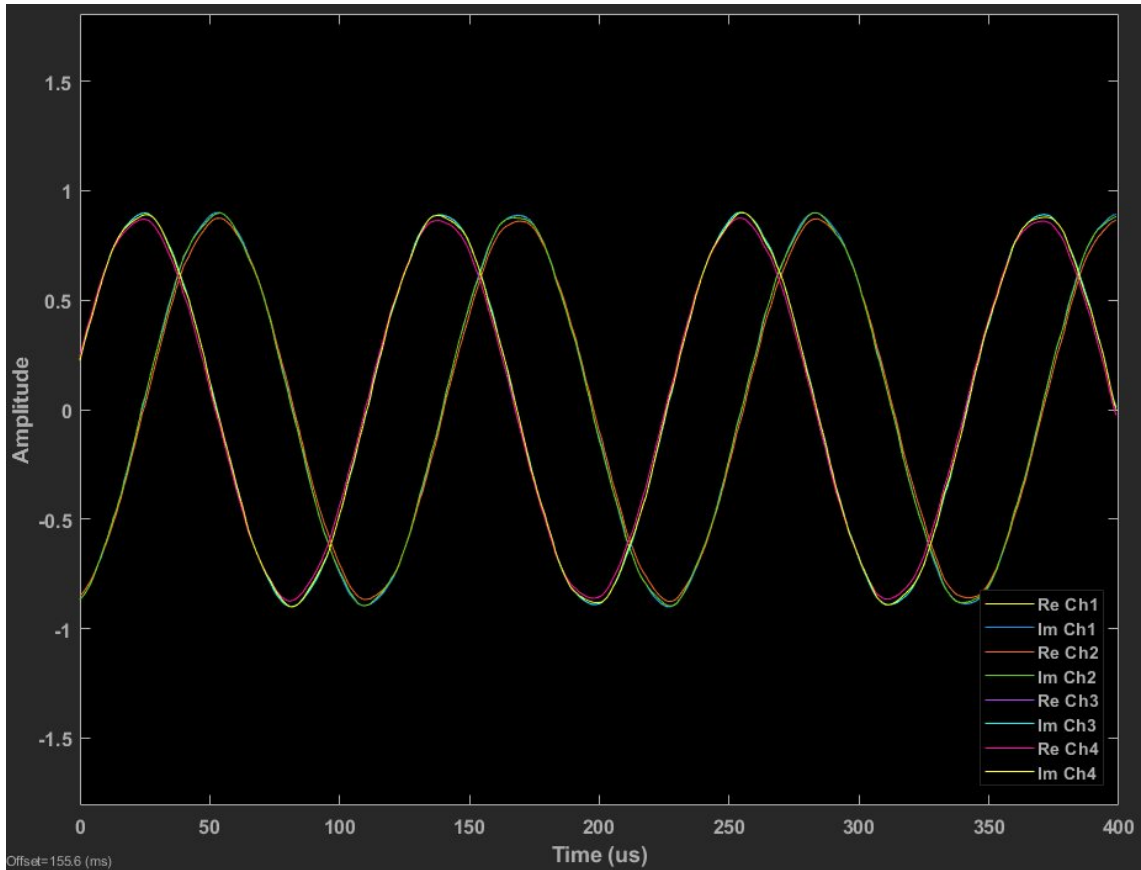


**Figure 3.23:** After phase calibration of the four channel receiver showing the IQ signals.

all channels, rotating the signals of channels 2,3,4 to synchronize with channel 1 [87]. The synchronized phase received at the four channels at the origin is shown in **Figure 3.24**. Amplitude normalization and the calculated phase offset is applied to every new frame received. Hence, the origin for the receiver is set and now the receiver can be set at different angles around the semi-circle. It should be noted that this process is done only once at the beginning and should be done if the SDR is rebooted or re-tuned. However, the MCS calibration is done only once and not required after reboot. The received data can be viewed in real time on the time and spectrum scopes as shown for  $0^\circ$  in **Figure 3.24**.

### 3.3.3. Experimental procedure

In order to calculate the decoupling matrix two sets of data are required. The coupled voltages which are the received voltages by the array and the isolated voltages which are the voltages received by only one of the antennas alone by removing all other elements. These two data sets are required for every angle of incidence under consideration.



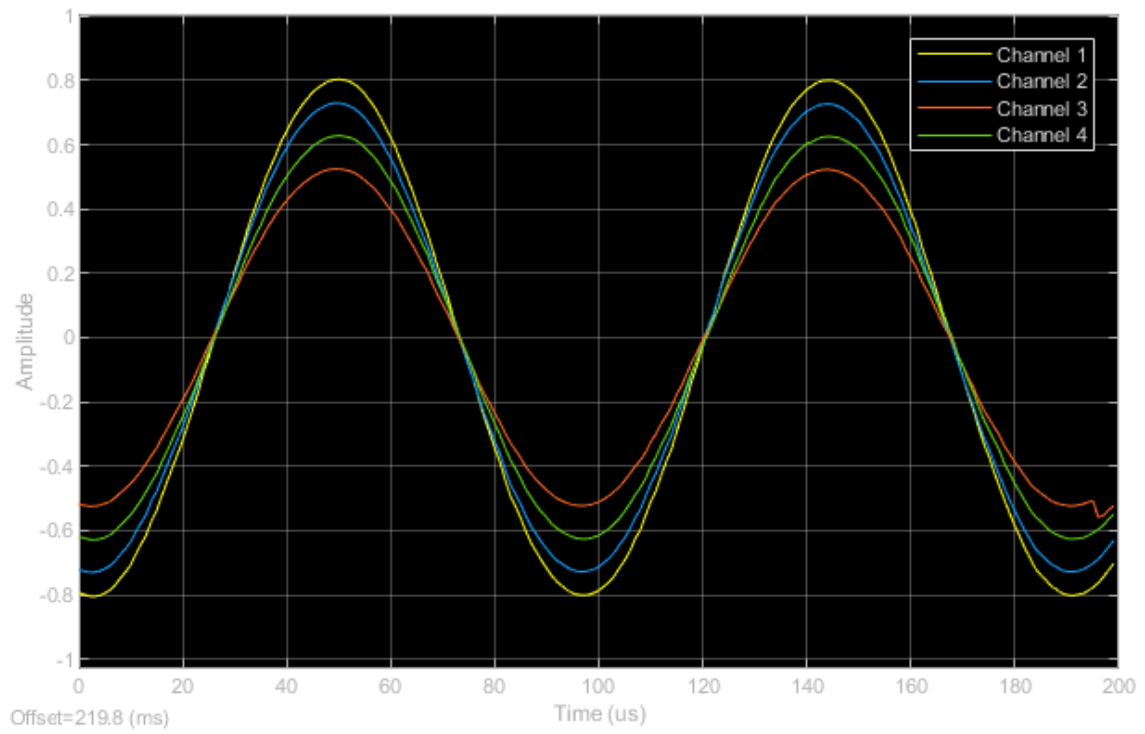


**Figure 3.24:** Received signal at  $0^\circ$  showing the calibration being set at origin.



**Figure 3.25:** Setup for measuring the isolated voltages for the quasi yagi antenna array.

### 3.3.3.1. Isolated case setup

For the quasi yagi antenna the isolated setup is shown in **Figure 3.25**. The power pattern is measured and compared with results from EM simulation as shown in **Figure 3.26** for the isolated antenna. The power pattern is in close proximity to the simulated results which

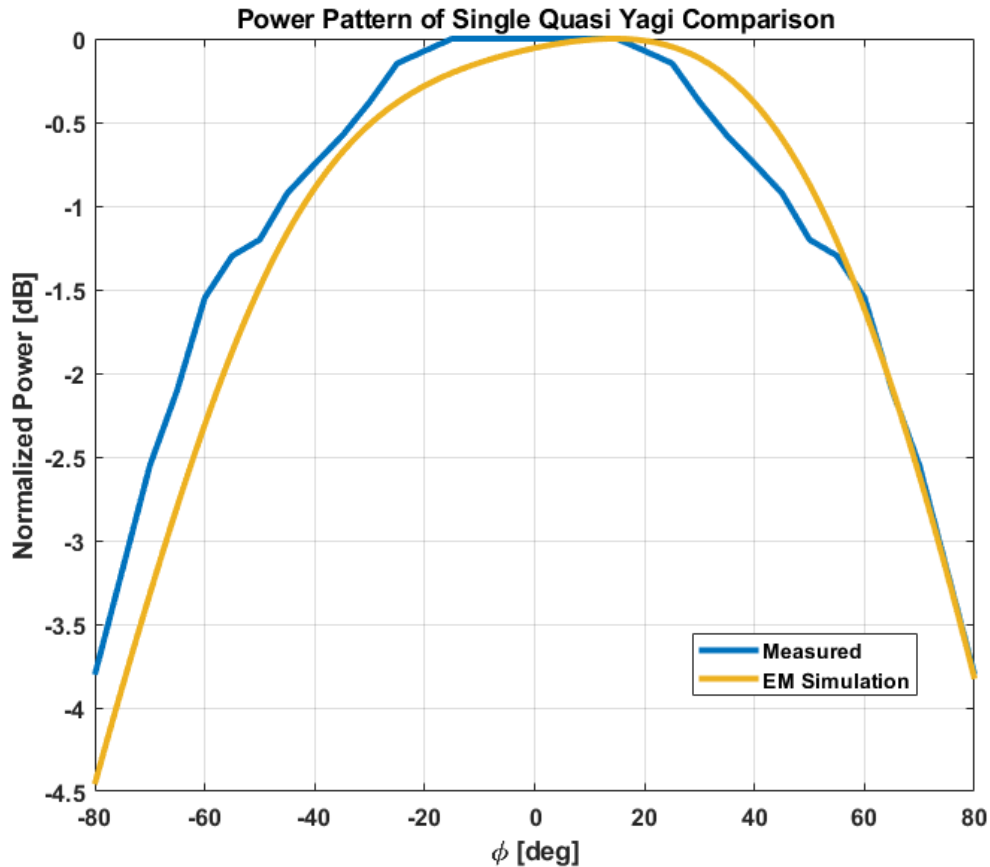


**Figure 3.26:** Comparison of the power pattern of a single quasi yagi antenna.

endorses the accuracy of the measurements involved. This experiment is a preliminary for massive MIMO mutual coupling compensation hence it is common to have above 100 antennas in an array in such a configuration. In order to calculate isolated voltages for such a structure would mean removing all antennas and placing one antenna at a time at all those 100 positions and then measuring for all angle of incidences which is highly impractical. Instead, it is proposed to calculate the isolated voltage for only one antenna at the origin. In order to calculate the isolated voltages, we remove all antennas and leave one antenna at channel 1 and measure from all the given angle of incidences and then give a phase shift to each measured angle separately to calculate the isolated voltages of the array. This method not only reduces the time and effort involved but makes measurements

for massive MIMO more practical and realistic. Infact, in simulation, this is exactly how isolated voltages differ from one element of the array to another in case of a ULA.

### 3.3.3.2. Array setup

The power pattern for the array is measured and compared with EM simulation results as shown in **Figure 3.27**. When the spacing of the array is varied from  $0.24\lambda$  to  $0.57\lambda$  for the quasi yagi array setup in **Figure 3.18**, the resulting power pattern is shown in **Figure 3.28**. When the antenna spacing is decreased from  $0.57\lambda$  to  $0.24\lambda$ , the main beam becomes more directive and the detection becomes worse with optimum detection range decreased from  $\pm 60^\circ$  to  $\pm 20^\circ$  as will be discussed in the upcoming **Subsection 4.3.2**.

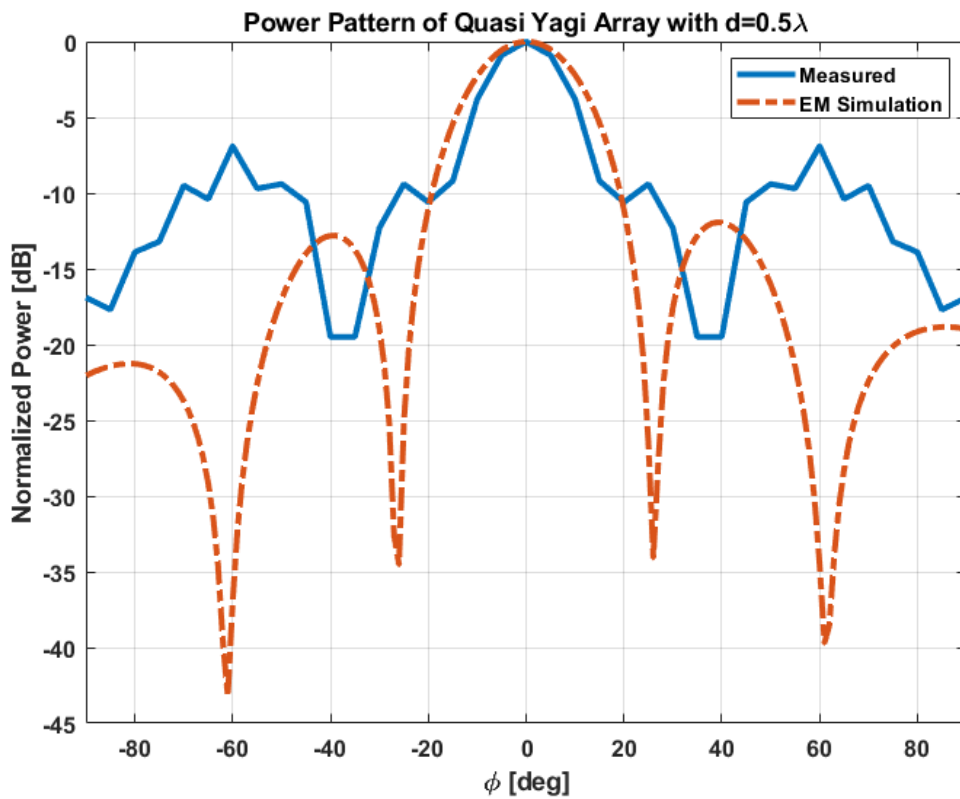


**Figure 3.27:** Comparison of measured and simulated power pattern of quasi yagi array for  $d=0.5\lambda$ .

Here it should be noted that 5 million IQ samples were measured for each angle both for the array and the isolated case which was then divided into 1251 frames with 4000 samples per frame. This amount of data was calculated just to have ample readings for studying and analyzing using different techniques e.g., Deep Learning (future prospects). Similarly, 6.5 GB of data was stored which consists of coupled voltages and isolated voltages for 13

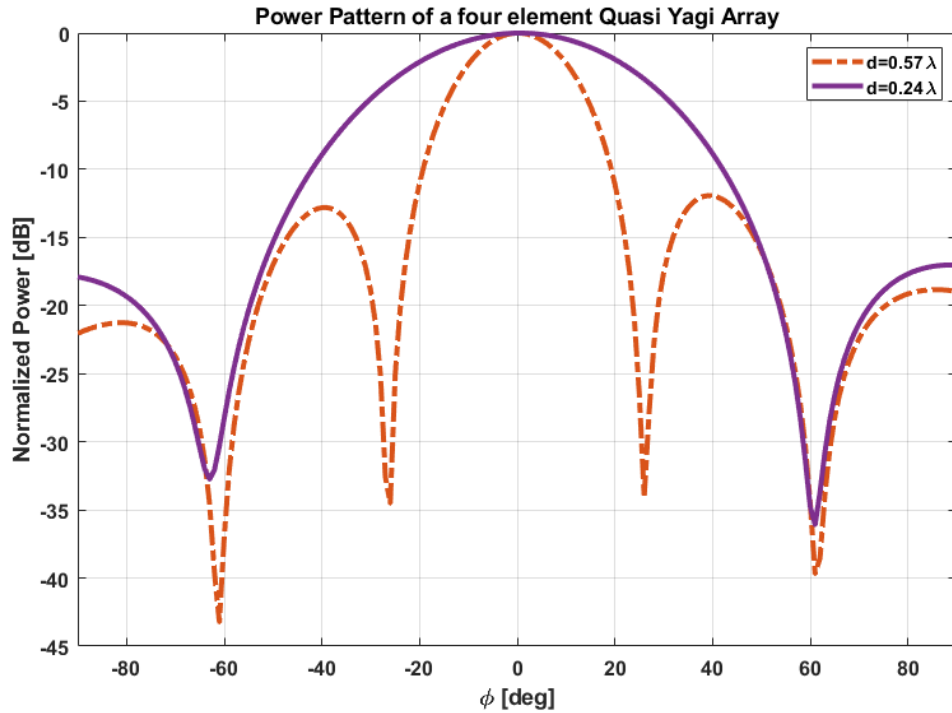


**Figure 3.28:** Comparison of power pattern of quasi yagi array for  $0.57\lambda$  and  $0.24\lambda$  spacings.

different angles ranging from  $0^\circ$  to  $60^\circ$  for this array setup. First, we estimate the DoA with the received coupled voltages then after MCC using the new algorithm we estimate the DoA. The results are shown in the following sections for coupled, compensated and isolated cases.

### 3.3.3.3. Decoupling matrix

As mentioned above, a huge amount of data has been recorded for each angle of incidence and each angle has 1251 frames which is compensated by a single matrix only. According to this method, every angle has a separate decoupling matrix however the decoupling matrix is constant for the same spacing even if different antenna arrays are involved. In other words, if a directional or omni-directional antenna is used the decoupling matrix will be the same if the spacing of the array is the same.

### **3.4. Algorithm III: IEEE 802.11a SIMO End-to-End Transceiver Implementation On Xilinx® Zynq® FPGA And An Analog Devices™ FCOMMS5 Radio With Mutual Coupling Compensation For Spectral Efficiency Application**

#### **3.4.1. Introduction**

One of the main features for deploying MIMO systems is to achieve high data rates and spectral efficiency. However, it has been shown in [88]–[90] that MC deteriorates the channel, increases the correlation, and reduces the achievable capacity. Some studies [91], [92] indicate that the effect of MC maybe positive or negative depending on the propagation environment spatial correlation properties. Further studies [93]–[95] show that by mitigating the effects of MC the radiation pattern as well as the overall system sum-rate is improved. In our work [95], using EM simulation for different array structures such as 1-D , 2-D and 3-D arrays, it was shown that the channel capacity is improved after compensation of MC in power-domain non-orthogonal multiple access (NOMA) system for both uplink (UL) and downlink (DL) transmissions.

In this section, an experimental study is performed for a Single Input Multiple Output (SIMO) end-to-end transceiver system using IEEE 802.11.a Orthogonal Frequency Division Multiplexing (OFDM). Using this modulation a high-speed serial information signal is divided into multiple lower-speed subsignals that are transmitted simultaneously at different frequencies in parallel over a 5 MHz channel located at 2.4 GHz frequency band. This parallel form of transmission over multiple subcarriers enables to obtain high data rates. However, it is observed that since the multiple receiver antennas are closely spaced and thus EM coupling is inevitable, resulting in a corrupted received signal. By analyzing different signal metrics such as constellation diagram, Signal to Noise Ratio (SNR), Error Vector Magnitude (EVM), channel capacity and visualizing signals in both time and frequency manifest these effects due to MC.

#### **3.4.2. SIMO End-to-End transceiver hardware design**

In this work Xilinx® Zynq-Based Radio is used to transmit and receive Wireless LAN (WLAN) with MATLAB® and real-time DSP. An image file is transmitted using IEEE 802.11a standard and baseband waveforms are generated. The waveforms are upconverted

and continuously transmitted using ADALM-PLUTO SDR with a single transmitter antenna. The received waveform is downconverted to baseband using a Xilinx® Zynq® (ZC706) FPGA and an Analog Devices™ FMCOMMS5 radio with four receiver channels and is decoded in real-time to recover the transmitted information.

### 3.4.2.1. IEEE 802.11a OFDM

IEEE® 802.11™ is a packet-based protocol. Each physical layer conformance procedure (PLCP) protocol data unit (PPDU) contains preamble and data fields. The preamble field contains the transmission vector format information. The data field contains the user payload and higher layer headers, such as medium access control (MAC) fields and cyclic redundancy check (CRC). The transmission vector format and the PPDU packet structure vary between 802.11 versions. In general, MAC Service Data Units (MSDUs) are generated from the image and then from each MSDU, a MAC Protocol Data Unit (MPDU) is made. The MPDUs are then passed to the PHY layer as PHY Layer Service Data Units (PSDUs). Each PSDU data is packed into a single Non-HT, 802.11a™ WLAN packet. These PSDUs are then formed into PPDU to generate the baseband WLAN waveform. This waveform is then upconverted and transmitted using a Xilinx Zynq radio. The 802.11a OFDM frame structure can be seen in **Figure 3.29** for a non-HT WLAN waveform. It consists of a preamble field followed by a SIGNAL field and multiple data fields. A preamble is transmitted at the start of a burst as shown in **Figure 3.30**. The preamble is used for synchronization and channel equalization. The SIGNAL field is transmitted using BPSK, which contains the length, modulation type, and data rate information. The burst is completed by appending multiple OFDM symbols containing the input data bits as shown in **Figure 3.31**.

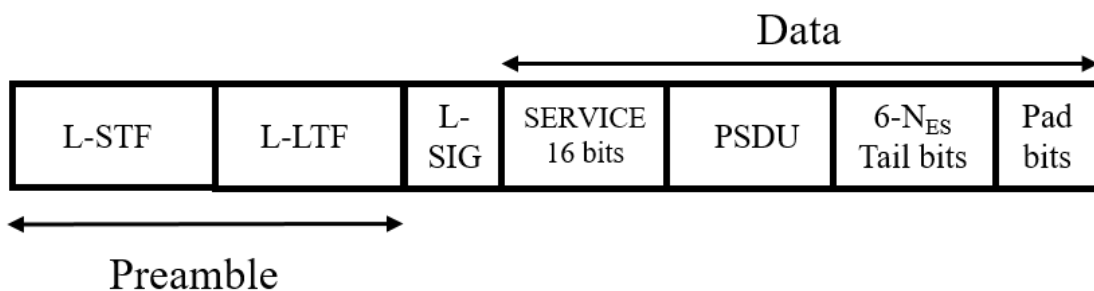


**Figure 3.29:** IEEE 802.11a OFDM frame structure.

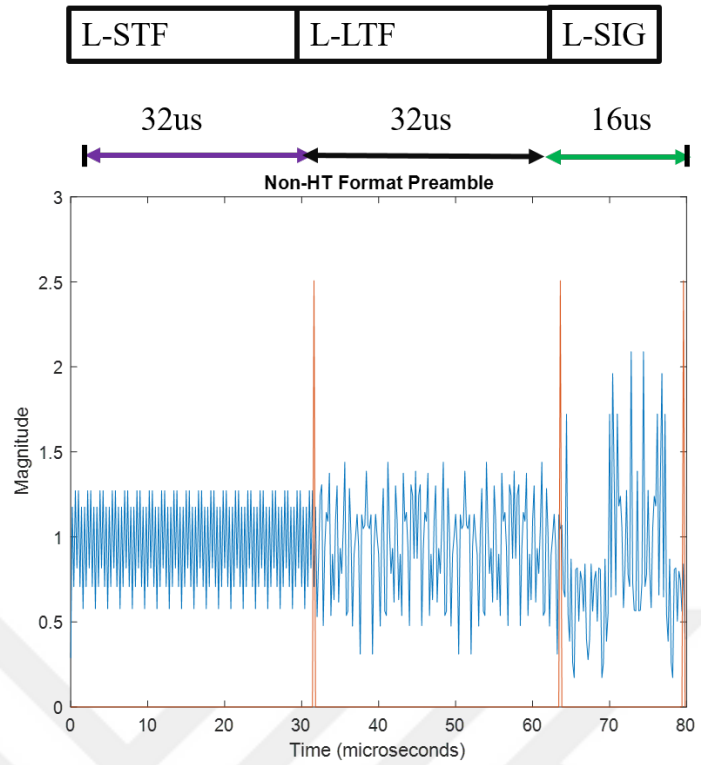


**Figure 3.30:** Generated preamble of WLAN OFDM packet.

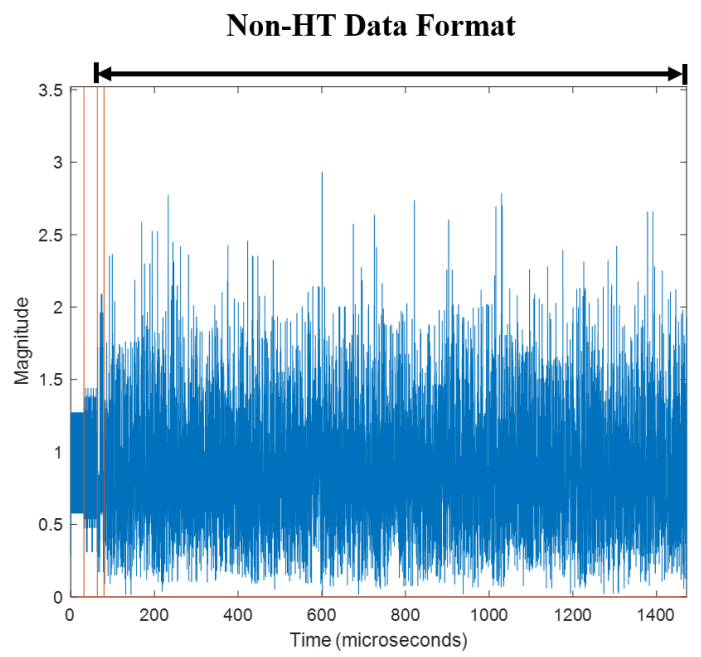


**Figure 3.31:** Generated Non-HT data format of WLAN OFDM packet.

Legacy Short Training Field (L-STF) has good correlation properties, therefore, it is used for start-of-packet detection, coarse frequency correction, and for setting the AGC. Channel estimation, fine frequency offset estimation, and fine symbol timing offset estimation rely on the Legacy Long Training Field (L-LTF). Legacy Signal Field (L-SIG) consists of 24 bits that contain rate, length, and parity information. It is transmitted using BPSK modulation, since its the most robust modulation, with rate 1/2 binary convolutional coding (BCC). Service field contains 16 zeros to initialize the data scrambler. PSDU is the main field which contains the data payload. Tail bits are required to terminate a convolutional code by using six zeros for the single encoding stream. In order to ensure that the non-HT data field contains an integer number of symbols the variable length Pad bits are used.

#### 3.4.2.2. Transmitter

The transmitted image is shown in **Figure 3.32** and the corresponding time and frequency domain of the WLAN packets are shown in **Figure 3.33**. This image is sent in 11 WLAN packets as can be seen from the time domain burst. Using OFDM Modulation and Coding Schemes (MCS) of 7 which uses modulation type of 64-QAM and coding rate of 3/4 supports a data rate of 13.5 Mbps [96] for a 5 MHz bandwidth as shown by the power spectrum plot in **Figure 3.33**.



**Figure 3.32:** Transmitted image using Pluto SDR.

#### 3.4.2.3. Receiver

At the receiver side we have a four element Quasi Yagi ULA which has a spacing  $d=0.24\lambda$ . The four channel receiver is working as a phased array therefore the calibration and synchronization process needs to be carried out before reception. Once the calibration procedure is completed the received WLAN packets are decoded in real-time using MATLAB.



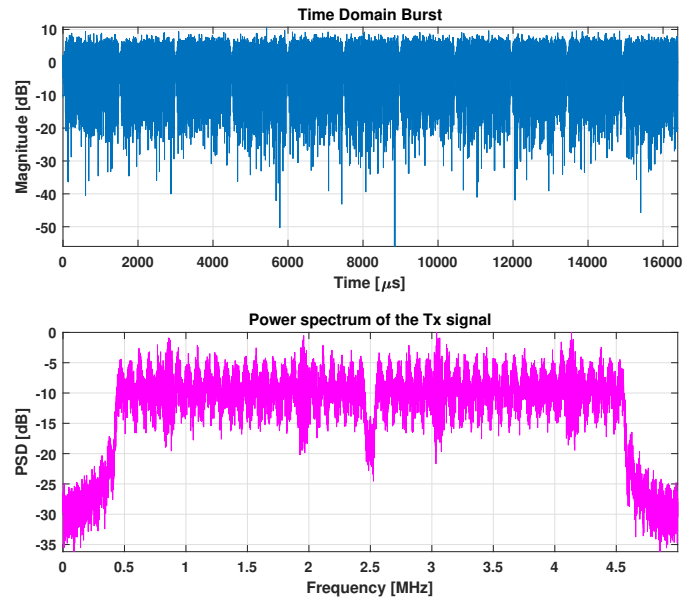


**Figure 3.33:** Time and frequency domain representation of the transmitted image of the WLAN packets.

The system specifications are mentioned in **Table 3.4**. The complete transceiver system is shown in **Figure 3.34**. Details of the hardware and calibration procedure are mentioned in **Subsection 3.3.2**.

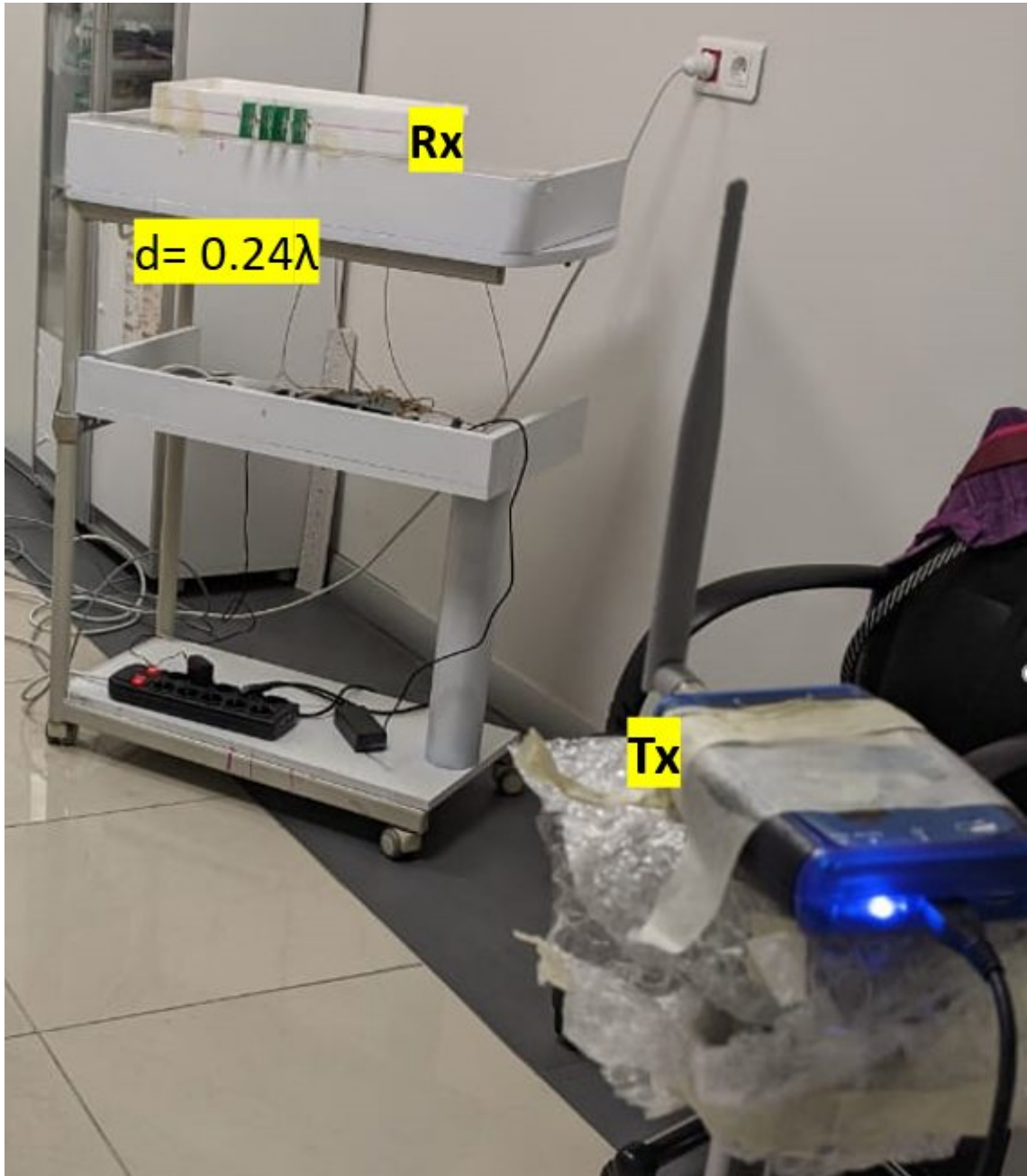


**Figure 3.34:** The receiving setup consists of a four-element Quasi Yagi array with  $0.24\lambda$  spacing connected to Xilinx Zynq ZC706 FPGA with Analog Devices FMCOMMS5 RFFE Module. The transmitter is an ADALM-PLUTO SDR connected to a TPLink WiFi antenna.

**Table 3.4:** System specifications for SIMO transceiver system.

Category	Item	Details
<b>Hardware</b>	SDR	ADALM-Pluto
	Antenna	TP-Link WiFi dipole
	Gain/Attenuation	Rx AGC slow attack / Tx 0 dB
	Sampling Rate	5 MHz
	Over Sampling Factor	1.5 ~ 7.5 MHz
<b>IEEE 802.11a OFDM</b>	Center Frequency	2.468 GHz
	Bandwidth	5 MHz
	MCS	7
	Modulation	64 – QAM OFDM
	Coding Rate	3/4
	OFDM PHY	Nsc= 52 Ndsc=48 Npsc=4 Tsym=16 us Tnsym=92
	Time Duration 1 packet	1472 us
	Guard Window	20 us
	11 WLAN Packets	16392 us

### **3.4.3. Mutual Coupling Compensation Algorithm**

The formulation of mutual coupling compensation algorithm for receiving antenna arrays and derivation of the decoupling matrix has been discussed in the previous chapters. In this experiment, the decoupling matrix is calculated using a mathematical model which needs the number of antennas, the spacing of the ULA and incident angle as an input only. Previously, measurements were required for different incident angles for coupled and isolated voltages and then the decoupling matrix was computed in run-time. However, the accurate mathematical modelling has relieved us of the pain-staking measurements and now these matrices can be calculated before hand. It should be mentioned that the complexity is only one matrix multiplication. The received data from the RFFE is first down-converted to base-band IQ data and then it is multiplied with the decoupling matrix. After that, the receiver algorithm is implemented. This shows that the method is easily implementable on any receiver system that incorporates antenna arrays. The ease and simplicity of this method for removing coupling and its accuracy can be seen in the following sections.

## CHAPTER 4

### 4. RESULTS AND DISCUSSION

#### 4.1. Algorithm I: An Experimental Study Of DoA Estimation With Mutual Coupling Compensation

##### 4.1.1. Experimental Results

As mentioned earlier, practical measurements are difficult since  $P \times 2N$  measurements are required. For this experiment with  $N = 7$  and  $P = 12$  the total measurements for the single source alone comprised of 128 measurements. In addition to the above, the

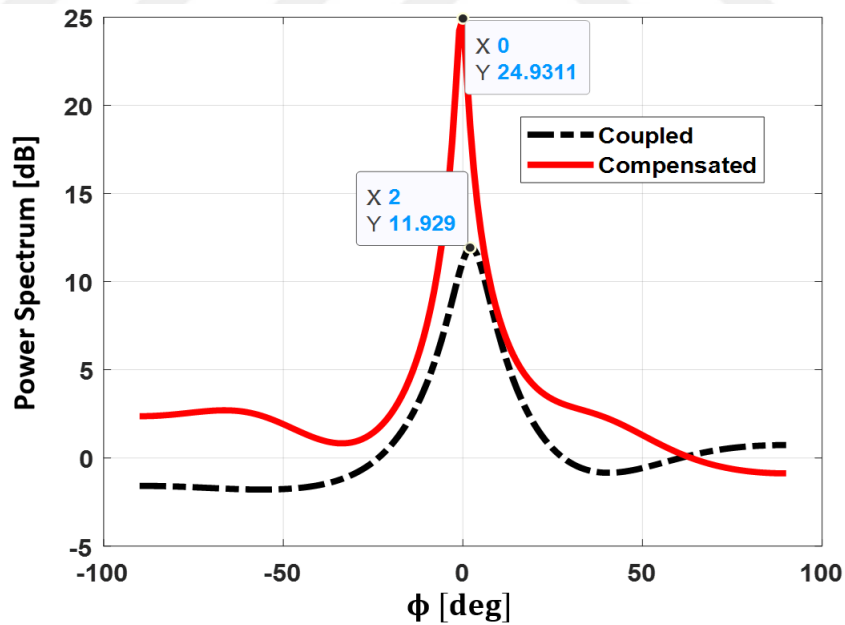


**Figure 4.1:** Spatial spectrum of the MUSIC algorithm for DoA detection of a single source signal  $\phi = 0^\circ$  and  $\theta = 90^\circ$  for seven-element monopole ULA with  $d = 0.2\lambda$ .

complete S-parameters were also measured for the array. The MUSIC spectrum for the experimentally measured DoA for a few angles can be seen in **Figure 4.1**, **Figure 4.2** & **Figure 4.3**. When incident angle was from boresight or  $\phi = 0^\circ$  the angle was estimated

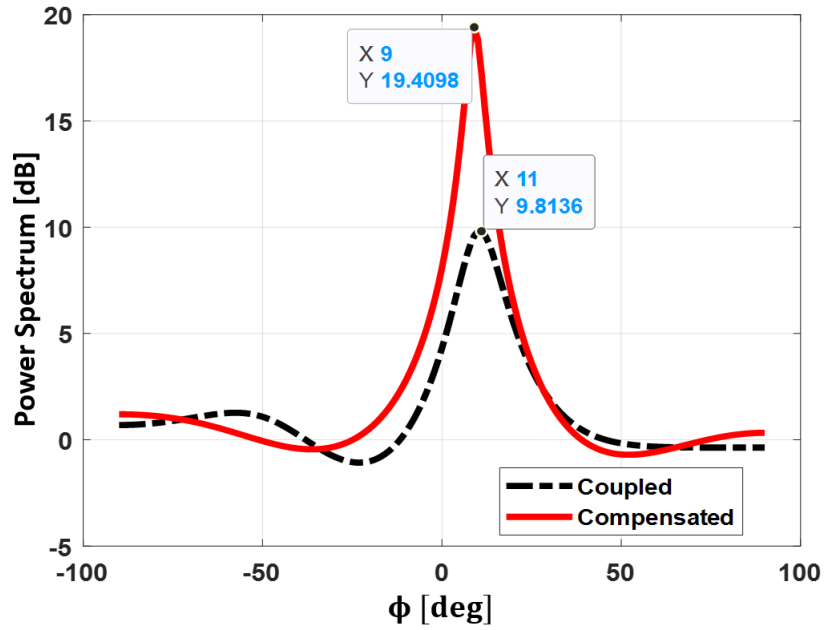


**Figure 4.2:** Spatial spectrum of the MUSIC algorithm for DoA detection of a single source signal  $\phi = 10^\circ$  and  $\theta = 90^\circ$  for seven-element monopole ULA with  $d = 0.2\lambda$ .

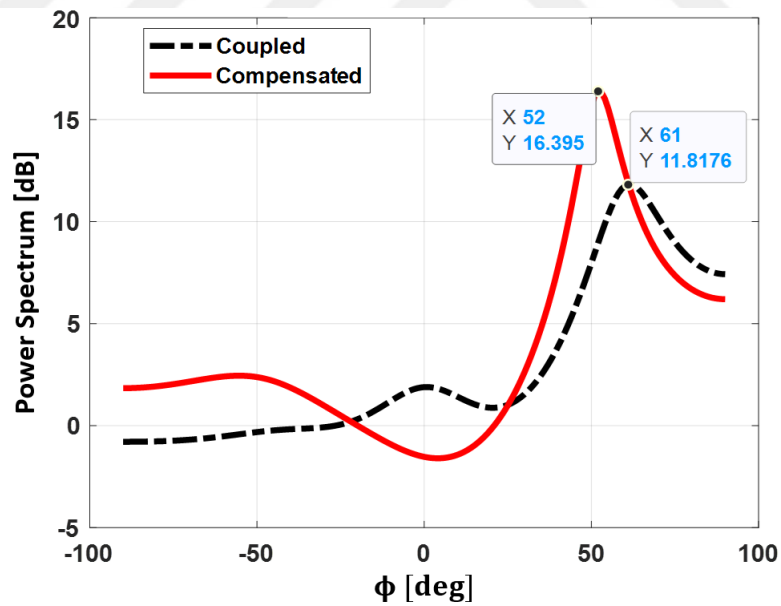


**Figure 4.3:** Spatial spectrum of the MUSIC algorithm for DoA detection of a single source signal  $\phi = 50^\circ$  and  $\theta = 90^\circ$  for seven-element monopole ULA with  $d = 0.2\lambda$ .

accurately as compared to  $\phi = 10^\circ$  where there was one degree error. The error was increased when the incident angle was  $\phi = 50^\circ$ . The tabular form of various azimuth angles for a single source can be seen in **Table 4.1**. It can be see that for some angles highlighted in yellow the error was more than 10 degrees whereas for others the error was within +/-5 degrees. Similarly, for multiple coherent sources the results can be seen in **Table 4.2**. When the two sources are separated by a large angle then DoA was able to be detected however when separation was decreased to 30 degrees only one peak could be detected.

**Table 4.1:** Measured results for DoA estimation of a single source using a seven-element monopole array in an anechoic chamber.

Sr.	Incident angle	Detected angle with coupling (a)	Compensated angle (b)	Error (a)	Error (b)
1	-90	-90	-90	0	0
2	-70	-83	-81	13	11
3	-50	-52	-53	2	3
4	-30	-34	-32	4	2
5	-10	-9	-9	1	1
6	0	2	0	2	0
7	10	11	9	1	1
8	15	23	22	8	7
9	30	33	34	3	4
10	50	61	52	11	2
11	70	81	75	11	5
12	90	90	90	0	0

**Table 4.2:** Measured results for DoA estimation of multiple coherent sources using a seven-element monopole array in an anechoic chamber.

Sr.	Incident angles 0 to 180	Incident angles -90 to 90	Incident angle (2) -90 to 90	Detected Inc1, Inc2 with MC (a)	Compensated angle (b)	Error (a)	Error (b)	Two sources separation
1	62, 112	28	-22	22, -33	29, -29	6, 10	1, 7	50
2	62, 103	28	-13	7, -26	19, -34	21, 13	9, 21	40
3	81, 112	9	-22	41, -58	NP, -18	32, 36	NP, 4	30
4	68, 123	22	-33	64, -12	42, -15	42, 21	20, 18	55

#### 4.1.2. Conclusion

In general, Algorithm I gives encouraging results for MCC in receiving antenna arrays as compared to its predecessors because of the main assumption of working in the receiving mode and terminating the antenna elements in a load impedance  $Z_L$  in order to take into account the re-radiation effect from other array elements. The simulation results showed that for tightly spaced antennas this method is favorable however one major drawback is the dependence on  $\theta$  of the  $Z$  matrix. In general, for an omni-directional antenna, we expect that the mutual impedances should be independent of the incident DoA and be a property of the structure alone. Due to this incorrect assumption, the author needs to carry out a lot of measurements for computing the  $Z$  matrix which in real-life is not very practical. For this experiment alone 168 measurements were taken for only a single source and MIMO BS has 64 to 128 antennas thus resulting in massive measurement requirements. The experimental results presented here although agreed with [59] for single source, in some parts for example multiple coherent sources the results were erroneous especially when the angular spacing between the sources was limited to 30 degrees. The limitations of this method are as follows:

1. Limited to omni-directional antennas only.
2.  $Z$  is a function of  $\theta$  and independent of  $\phi$ .



3. Multiple coherent sources detection depend on the angular separation between the sources. Practically require even higher separation.
4. Requires at least 10 different incident angles for measurements ( Isolated + Array ) to solve  $N(N-1)$  unknowns. In other words,  $P \times 2N$  total measurements are required.



## 4.2. Algorithm II: Mutual Coupling Compensation In Receiving Arrays And Its Implementation On Software Defined Radios For DoA Estimation Application

### 4.2.1. Experimental Results

First, the general case of  $d = \lambda/2$  was considered and DoA was calculated for angles  $0^\circ$  to  $60^\circ$  in steps of  $5^\circ$ . Without using a decoupling matrix, the target signal is directly fed to the MUSIC algorithm. Next, the ULA with  $d = \lambda/4$  is used and DoA is estimated without using the decoupling matrix. Finally, the mutual coupling is compensated by using the decoupling matrix and the DoA is estimated. The results are shown in **Figure 4.4** and **Figure 4.5**. In the presence of coupling the accurate range of DoA is limited to  $\pm 25^\circ$  with  $1^\circ$  deviation however after compensation the range was increased to  $40^\circ$  for  $d = \lambda/4$ . In [80], [97], it was shown experimentally that for  $d = \lambda/2$  ULA the average deviation depends on the distance of the transmitter with errors ranging from  $0.5^\circ$  to  $6^\circ$  for certain angles. The MUSIC spectrum for the case when DoA is from  $\phi = 60^\circ$  is shown in **Figure 4.5**. It can be seen that the compensated results for  $d = \lambda/4$  are in close proximity to those measured when ULA with  $d = \lambda/2$  is used. The estimated DoA in real-time for two separate angles of  $\phi = 45^\circ$  and  $\phi = 60^\circ$  can be seen in **Figure 4.6**. In the first case,  $d = \lambda/2$  ULA is used for incident angle  $\phi = 45^\circ$  but an error of  $6.5^\circ$  is observed which shows the effect of MC on the optimally spaced array. In the second case,  $d = \lambda/4$  ULA is used to detect the incident angle of  $\phi = 60^\circ$  which has been accurately detected after compensation.

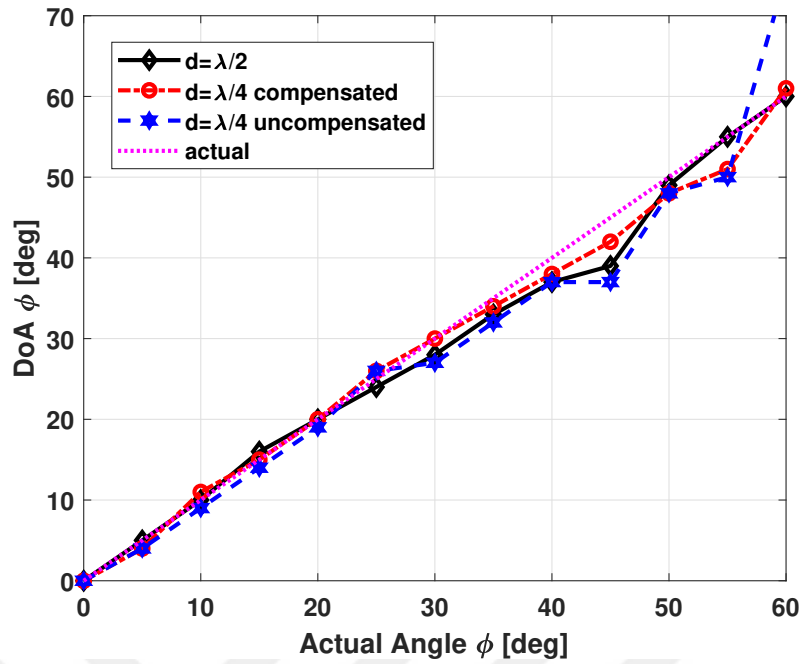


**Figure 4.4:** Estimated DoA vs Actual DoA for  $\theta = 90^\circ$ . DoA estimation for a four element ULA with  $d=\lambda/2$  and  $d=\lambda/4$  (with and without mutual coupling compensation).

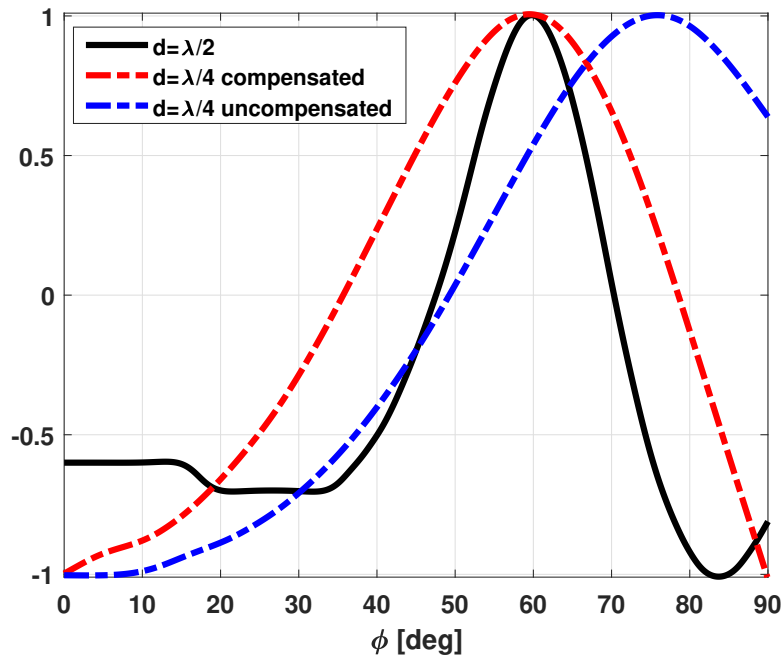
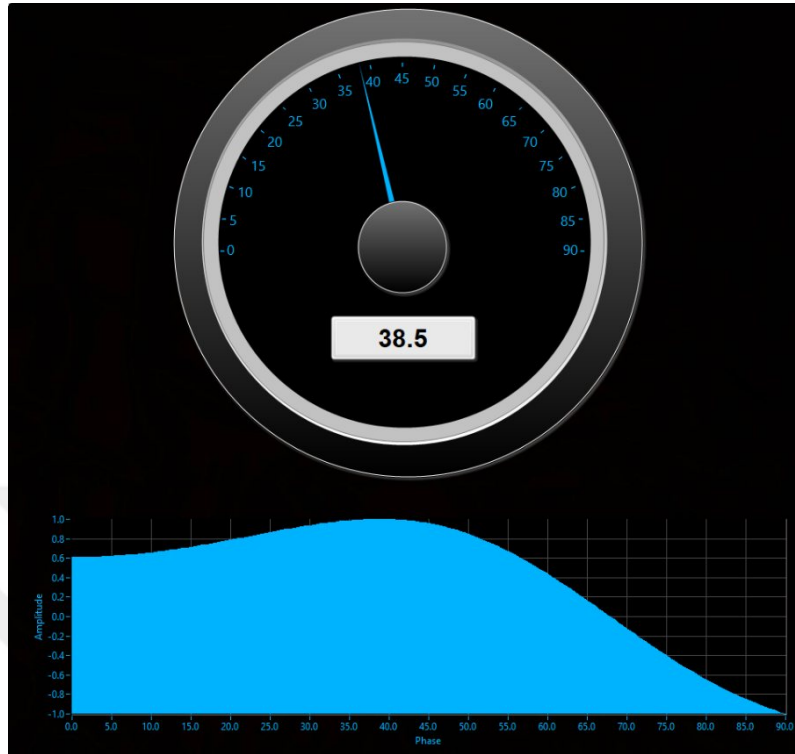


**Figure 4.5:** DoA estimation for a four element ULA with  $d=\lambda/2$  and  $d=\lambda/4$  (with and without mutual coupling compensation). Spatial spectrum of MUSIC algorithm for DoA detection of signal from  $\theta = 90^\circ$ ,  $\phi = 60^\circ$ .

a)



b)

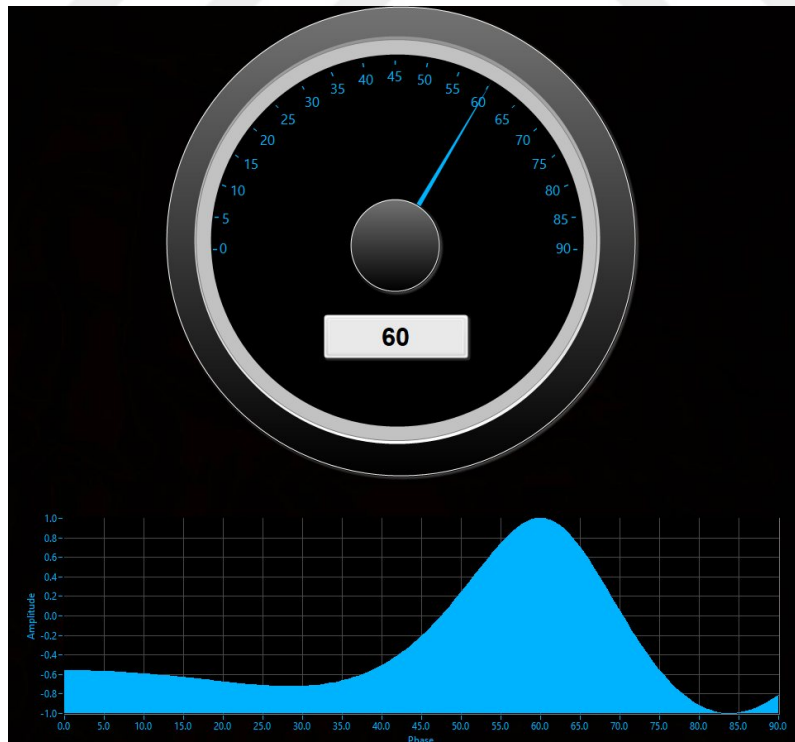


**Figure 4.6:** Estimated DoA using Labview for the incident angle (a)  $45^\circ$  for  $d=\lambda/2$  in the presence of coupling (b)  $60^\circ$  for  $d=\lambda/4$  after compensation.

#### 4.2.2. Conclusion

Mutual coupling is compensated in a four element receiving ULA using SDR. Two ULAs were studied to see the effect of coupling using a general case of  $d = \lambda/2$  and coupled case of  $d = \lambda/4$  inter-element spacing. The decoupling matrix was measured for the case of coupled ULA and then used to decouple the received voltages in real-time. The initial results show promising improvement in DoA estimation. Some limitations for this test setup can be addressed as below:

1. For a four element ULA the test setup required 6 USRPs and an external Clock system which makes it an expensive setup as well as bulky with all the cables and wiring involved.
2. For every re-tune command the array needs to be calibrated again.
3. The possible error sources include reflections in the environment, phase drift of the LOs over time, antenna gain and phase mismatch, positioning of antenna elements in the array as well as software implementation errors.
4. The software platform requires a good PC with enough memory and SSD for real-time data acquisition.

This was the first time real-time MCC and DoA estimation was implemented using SDRs. Due to the above limitations, further testing using different antennas such as directional antennas, as well as UCA and arbitrary geometry arrays using a compact experimental test-bed needs to be carried out.

#### 4.3. Algorithm III: An Experimental Setup For Mutual Coupling Compensation In Receiving Antenna Arrays Using Xilinx® Zynq®-Based FPGA And An Analog Devices™ FCOMMS5 Radio For DoA Application

Different experiments were performed and their results are presented in this section. In the first experiment, the results of two different ULAs are compared for MCC and DoA measurements in real-time for a fixed spacing  $d=0.24\lambda$ . The first array consists of directional antennas of quasi yagi array as shown in **Figure 3.18** with transmitter placed at  $20\lambda$  whereas the second array is an omni-directional array using commercial antennas, TPLink WiFi antennas, as shown in **Figure 4.7** with transmitter placed at  $10\lambda$ . Although, the transmitter was placed at these two different distances the gain for the LNA in the receiver was adjusted so that equal power levels for both cases are observed.



**Figure 4.7:** Omni-directional four element ULA using TPLink WiFi antennas with spacing  $0.24\lambda$  with a directional antenna as transmitter.

The second experiment shows the results for commercial directional antennas using a different set of quasi yagi antennas as shown in **Figure 4.18** with spacing varied from  $0.4\lambda$  to  $0.6\lambda$  to show the effect of MC and DoA estimation.

### 4.3.1. Experiment I: Comparison of directional and omni-directional arrays with $0.24\lambda$ spacing for mutual coupling compensation and DoA estimation

Here, we discuss the results for two different antenna arrays namely directional and omnidirectional antenna arrays. The results are shown for two different incident angles  $\phi_1 = -20^\circ$  and  $\phi_2 = 40^\circ$ . It should be mentioned here, that in the presence of the coupling the DoA detection range for the quasi yagi array is  $\pm 25^\circ$  when the spacing is  $0.24\lambda$  however after the coupling is compensated the full range is recovered.

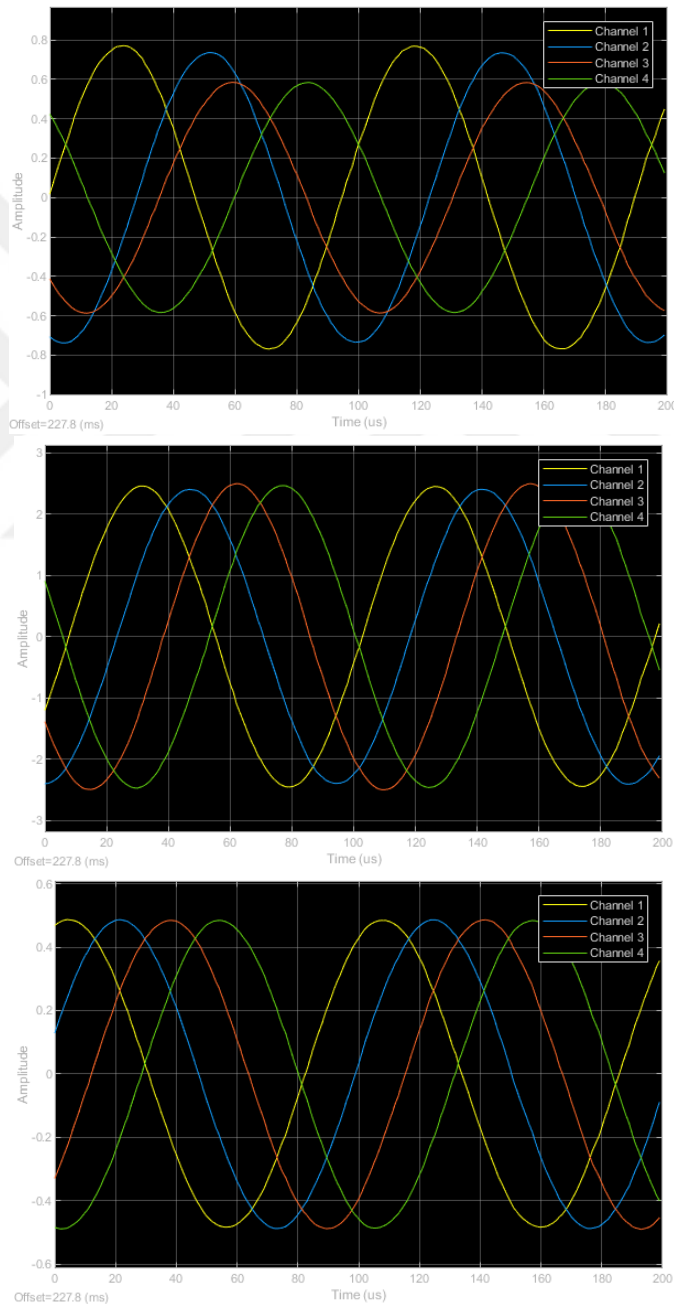


**Figure 4.8:** Received coupled (top) , compensated (center) and isolated (bottom) voltages for quasi yagi array from  $\phi = 40^\circ$ .

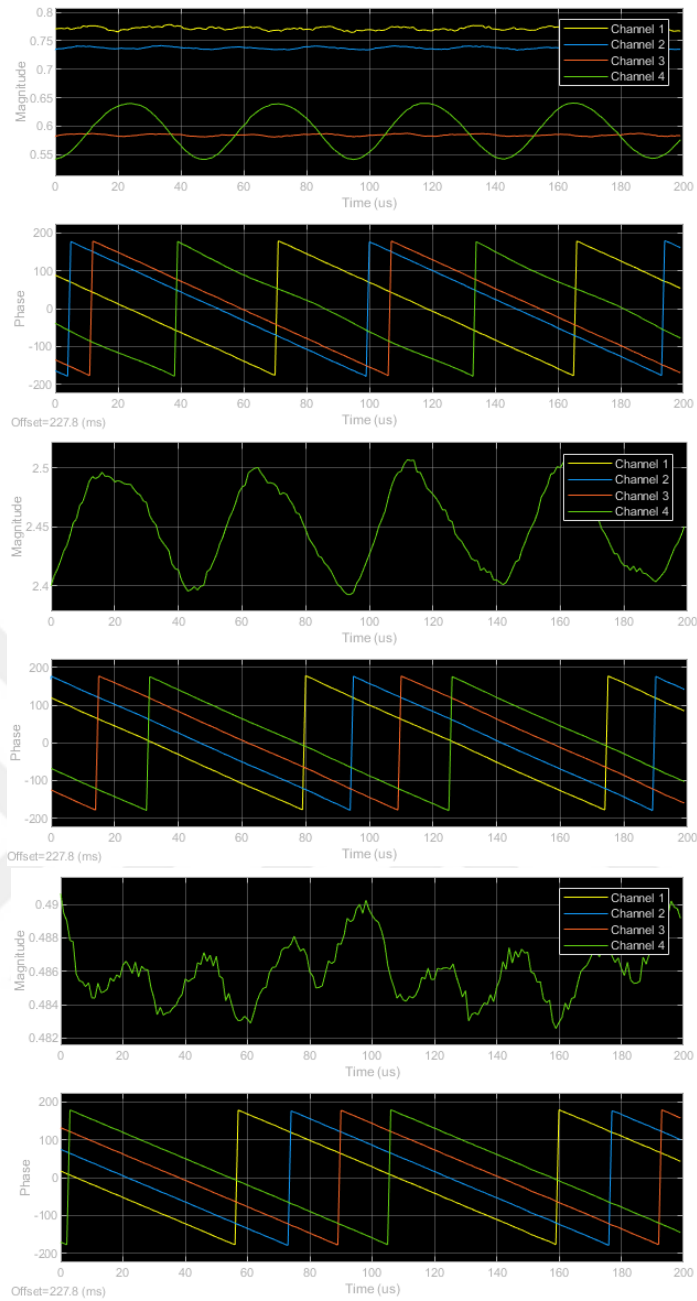


**Figure 4.9:** Magnitude and phase of received coupled (top) , compensated (center) and isolated (bottom) voltages for quasi yagi array from  $\phi = 40^\circ$ .

**Figure 4.8** shows the received signal in time domain for the coupled, compensated and isolated voltages for the quasi yagi array shown in **Figure 3.18**. It can be seen that the compensated voltages have the same amplitude and have a constant offset between different antennas as compared to the coupled voltages.

**Figure 4.9** shows the magnitude and phase of the received signal for the coupled, compensated and isolated voltages for the quasi yagi array. In the coupled case, it can be seen four different magnitudes are observed and the phase difference is not constant either whereas



in the compensated case its evident that all four magnitudes are exactly the same therefore we see one plot and the phase offset is constant.

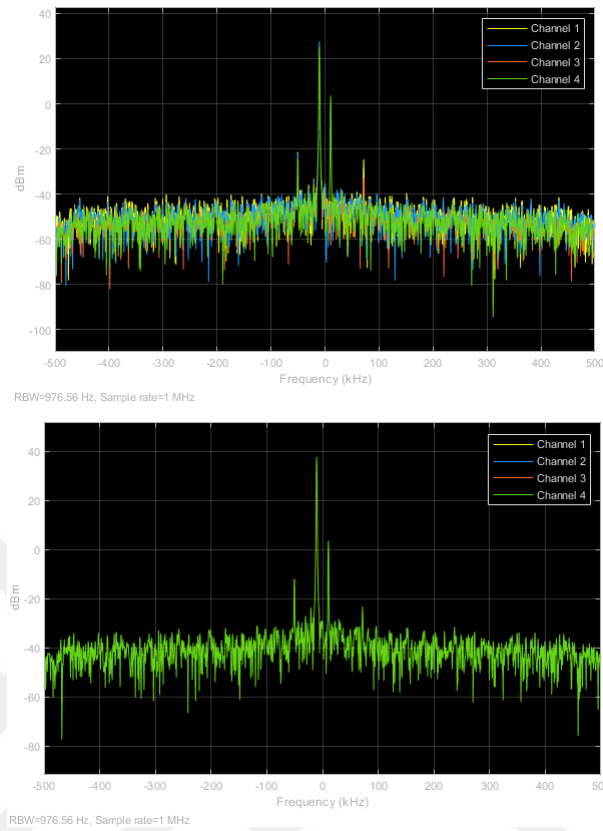


**Figure 4.10:** Spectrum of coupled (top) and compensated (bottom) received signal for quasi yagi array from  $\phi = 40^\circ$ .

**Figure 4.10** shows the received signal spectrum for the coupled and compensated voltages for the quasi yagi array shown in **Figure 3.18**. Since we expect a 10 kHz signal the peak has been observed at 10.42 kHz since AD936x uses a direct zero-IF down conversion. The spectrum plot for the coupled case shows four distinct plots whereas the compensated case shows four identical plots. Hence, the above plots verify the accuracy and superiority of the decoupling method used by showing the different aspects of the same data in time and spectrum domain and the phase of the received signals is of particular importance for DoA applications.

Furthermore, real-time DoA can be estimated which can be seen in the application developed in **Figure 4.11**. Here, six different estimation techniques have been used to find the DoA as described in the previous section. The results show that the DoA in the presence of coupling is off by 8 degrees whereas after coupling compensation the accurate result is obtained.

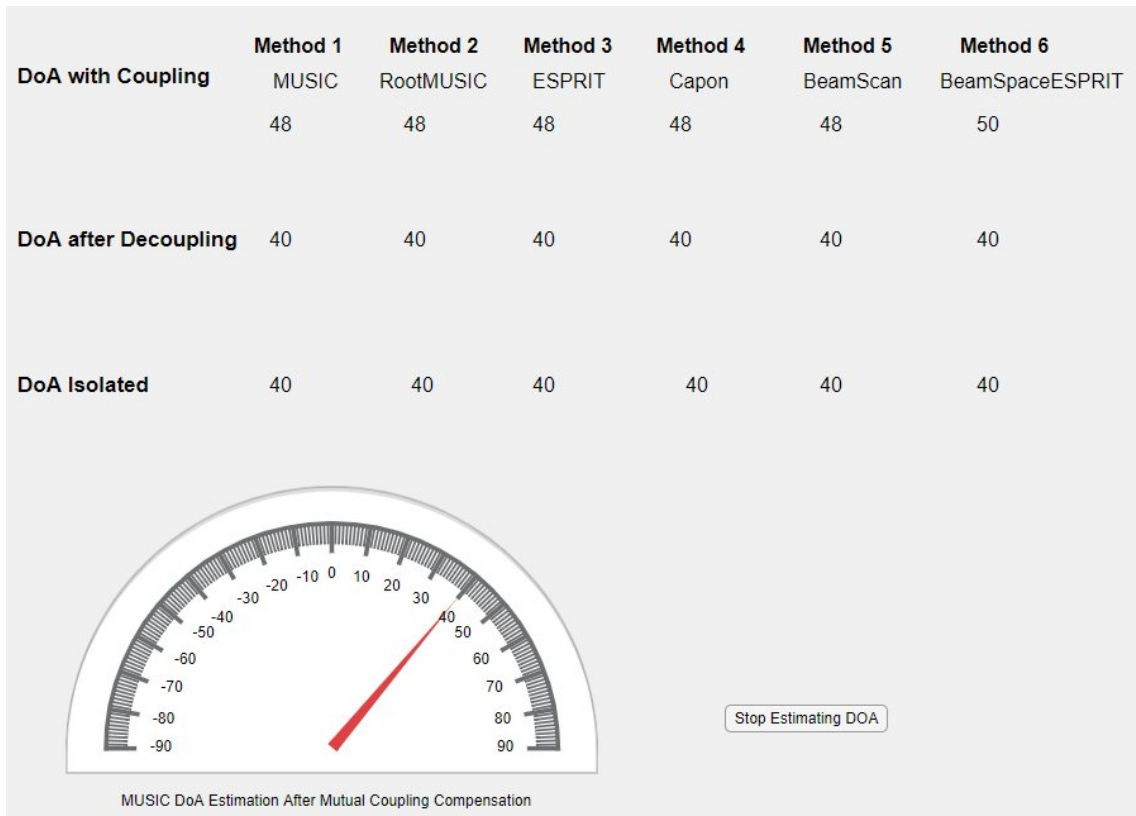


**Figure 4.11:** Real time DoA estimation App showing results for four element quasi yagi array with  $0.24\lambda$  spacing with incident angle from  $\phi = 40^\circ$ .

Here, the results for the commercial omnidirectional antennas, TPLink WiFi dipole antenna, as shown in **Figure 4.7** are presented for an incident angle of  $\phi = -20^\circ$ . **Figure 4.12** shows the received signal in time domain for coupled, compensated and isolated case. Since the angle is from  $\phi = -20^\circ$  then we expect antenna 1 (channel 1) to receive the signal first with maximum amplitude and the maximum phase to be on antenna 4 (channel 4).

**Figure 4.13** shows the magnitude and phase for the same data and the four distinct magnitudes in the coupled case and four identical magnitudes for compensated case can be observed as well as the phase is in order as expected with antenna 4 having maximum phase followed by antennas 3, 2 and 1. Similarly, **Figure 4.14** shows the spectrum of the coupled and compensated signals which again shows that after decoupling identical spectrum is observed. Here, it should be noted that the only difference between this case and the quasi yagi array is the different transmitter distance as well as the use of different types of antennas, the rest of the system specifications ( sampling rate, sample size, frequency, transmitting tone etc) is kept the same. Furthermore, it should be mentioned

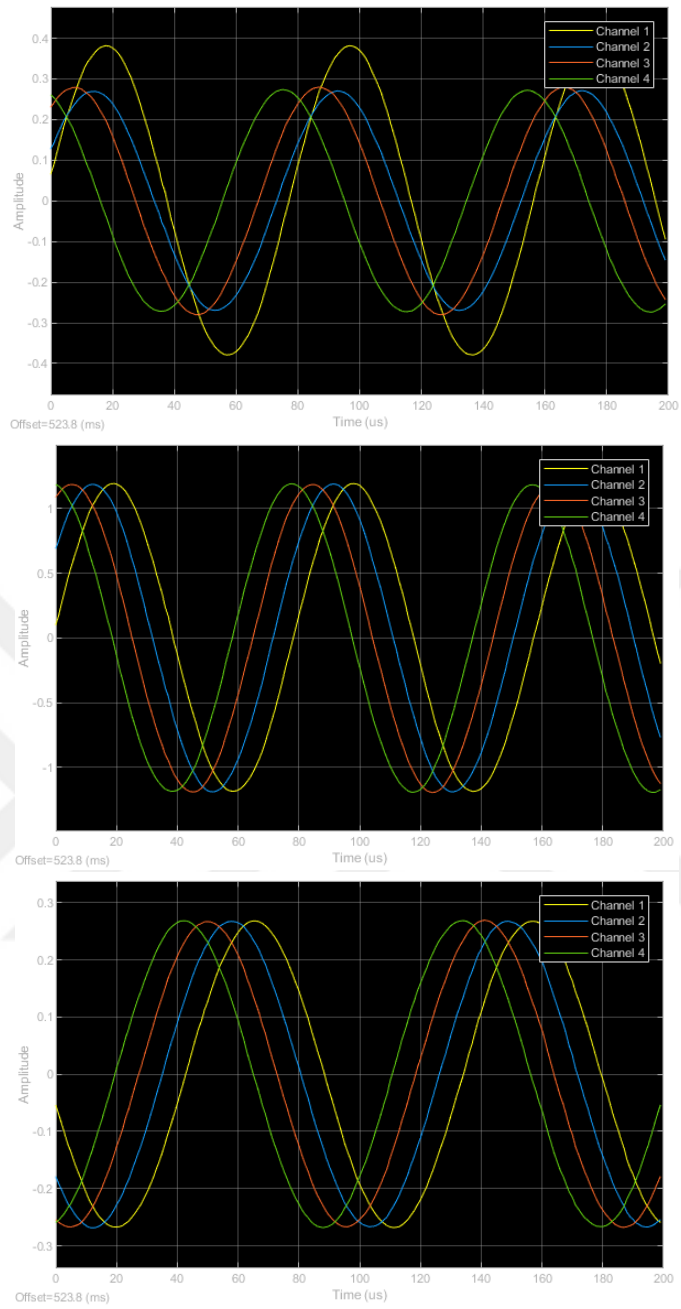


**Figure 4.12:** Received Coupled (top), Compensated (center) and Isolated (bottom) voltages for TPLink dipole array from  $\phi = -20^\circ$ .

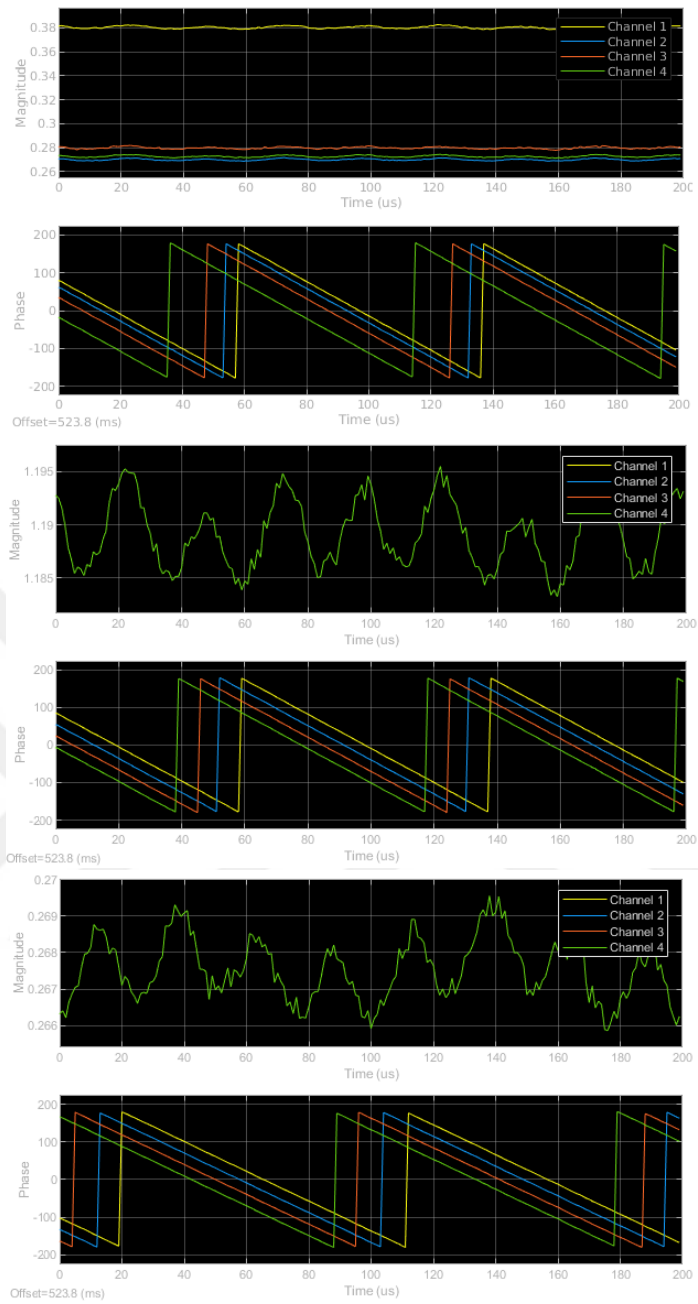


**Figure 4.13:** Magnitude and phase of received coupled (top), compensated (center) and isolated (bottom) voltages for TPLink dipole array from  $\phi = -20^\circ$ .

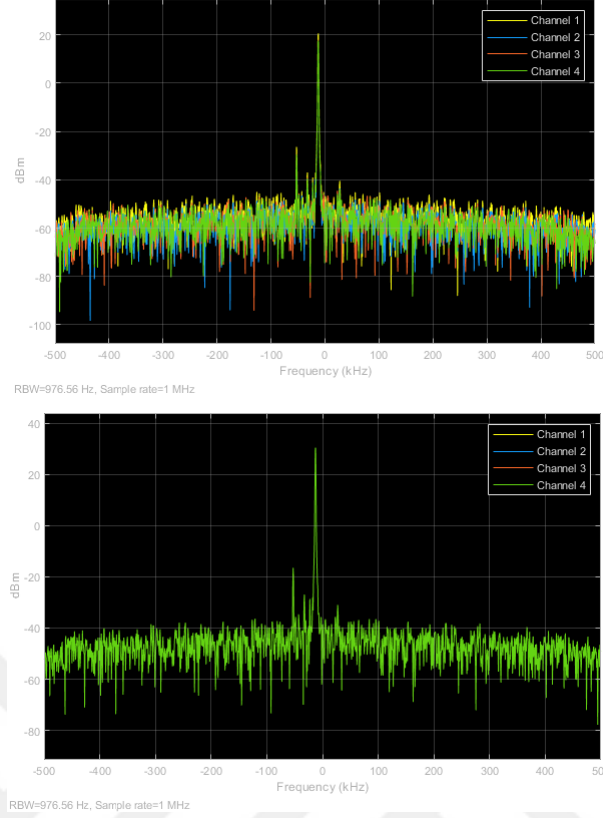


**Figure 4.14:** Spectrum of coupled (top) and compensated (bottom) received signal for TPLink dipole array from  $\phi = -20^\circ$ .

that this experiment was carried out in two different locations at Istanbul Medipol University Campus. In the first case, it was carried out at the end of the corridor which was a wider area and in the second case it was carried out inside the RF Lab where the space was limited. From the results, we can conclude that despite different experimental conditions, accurate MCC was observed which shows the superiority of the proposed technique.

In the presence of coupling the omni-directional antennas were able to detect the DoA accurately, this is because the detecting range for these arrays for  $0.24\lambda$  spacing is  $\pm 25^\circ$ . The real-time estimated DoA is shown in **Figure 4.15**.

However, when the incident angle was  $\phi = -40^\circ$ , then the estimated DoA for the dipole array was off by  $3^\circ$  as shown in **Figure 4.16** below.

Similarly, for the quasi yagi array when the incident angle was  $\phi = 20^\circ$ , the resultant DoA is observed to be erroneous by  $3^\circ$  as shown in **Figure 4.17**. This shows, that the detection is different for different arrays as well as in real-time since the measurement can be affected by other parameters such as interference, doppler effect etc therefore there are

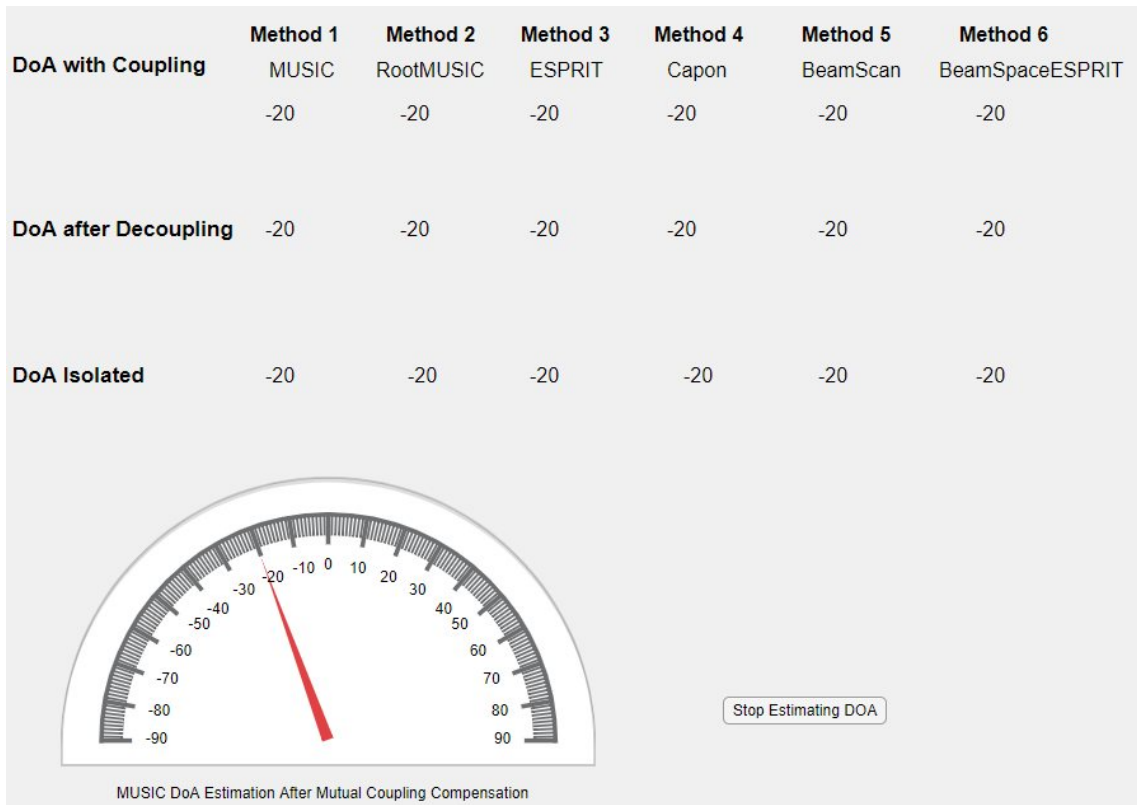


**Figure 4.15:** Real time DoA estimation App showing results for four element TPLink dipole array with  $0.24\lambda$  spacing with incident angle from  $\phi = -20^\circ$ .

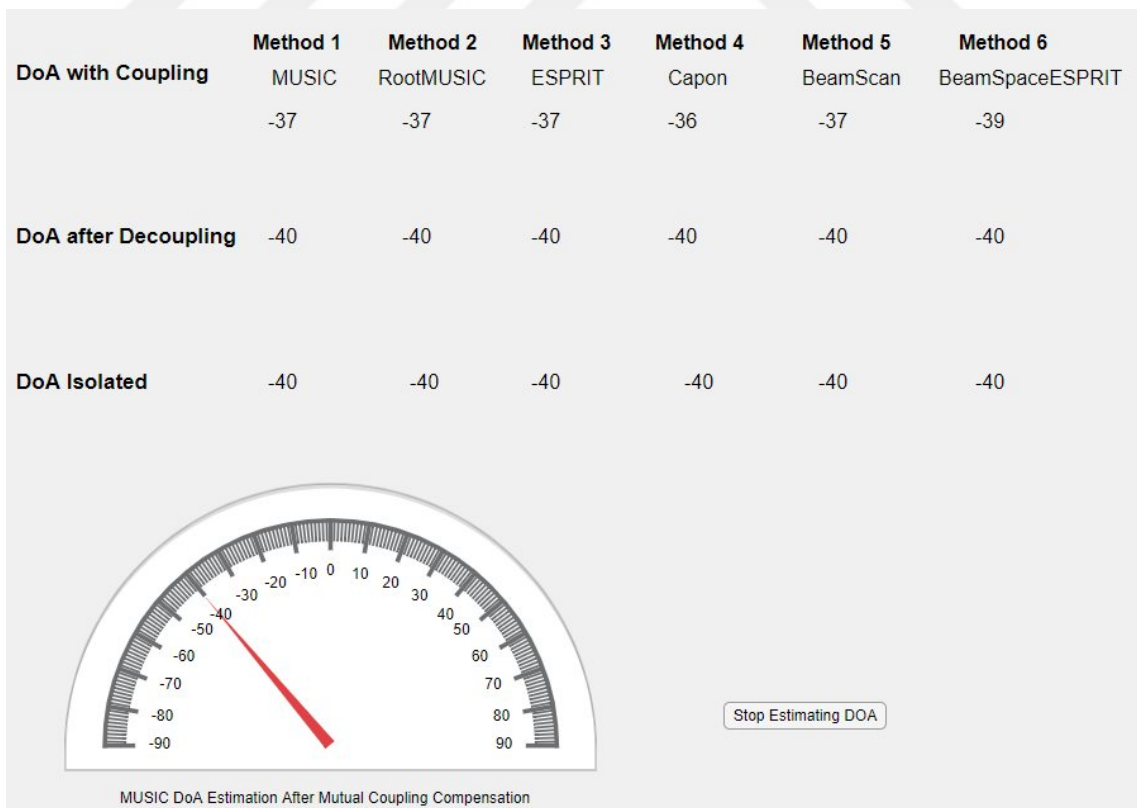


**Figure 4.16:** Real time DoA estimation App showing results for four element TPLink dipole array with  $0.24\lambda$  spacing with incident angle from  $\phi = -40^\circ$ .

fluctuations in the DoA estimation in the coupled case  $\pm 5^\circ$  however the uncoupled case is consistent throughout and is not affected by any fluctuations.

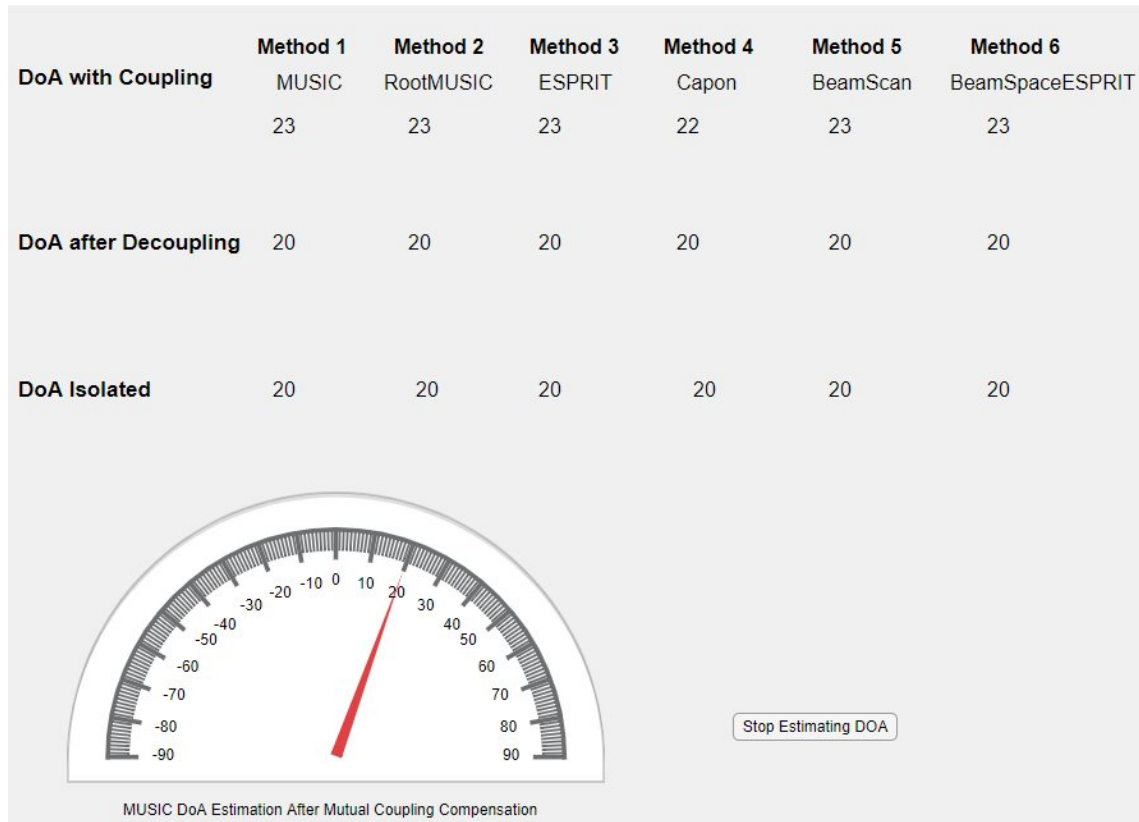


**Figure 4.17:** Real time DoA estimation App showing results for four element quasi yagi array with  $0.24\lambda$  spacing with incident angle from  $\phi = 20^\circ$ .

### 4.3.2. Experiment II: A study on DoA estimation vs spacing for a commercial quasi yagi array

A commercial quasi yagi ULA has been used for this experiment and the received voltages have been measured and compensated for various spacing and the comparison is discussed in this section. The setup is shown in **Figure 4.18** and **Figure 4.19**

The DoA experiment was carried out with the above array with three different spacings  $0.6\lambda$ ,  $0.5\lambda$  and  $0.4\lambda$ . The estimated DoA for these 3 different spacings are shown in **Figure 4.20**.

The results show that in the presence of coupling  $0.5\lambda$  is the optimum spacing which gives a range of  $\pm 60^\circ$  with less than  $5^\circ$  of error. For  $0.4\lambda$ , the optimum detection range is  $\pm 40^\circ$  for a  $5^\circ$  error whereas for  $0.6\lambda$ , the best range is  $\pm 35^\circ$  for a threshold of  $5^\circ$  error. The error plot is shown in **Figure 4.21**. The decoupling method is accurate in all cases which



**Figure 4.18:** A commercial quasi yagi ULA of four-elements with different spacing.





**Figure 4.19:** A commercial quasi yagi array for estimating DoA for different spacings.

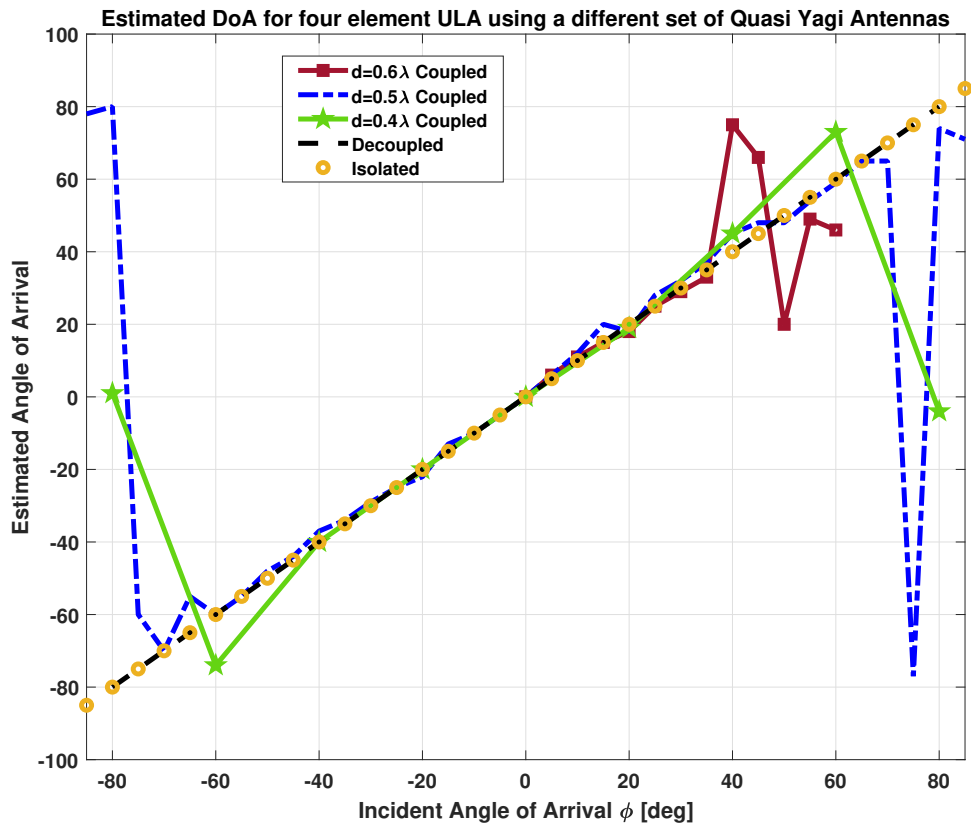


Figure 4.20: Estimated DoA in the presence of coupling for 3 different spacings  $0.6\lambda$ ,  $0.5\lambda$  and  $0.4\lambda$  for commercial quasi yagi ULA.

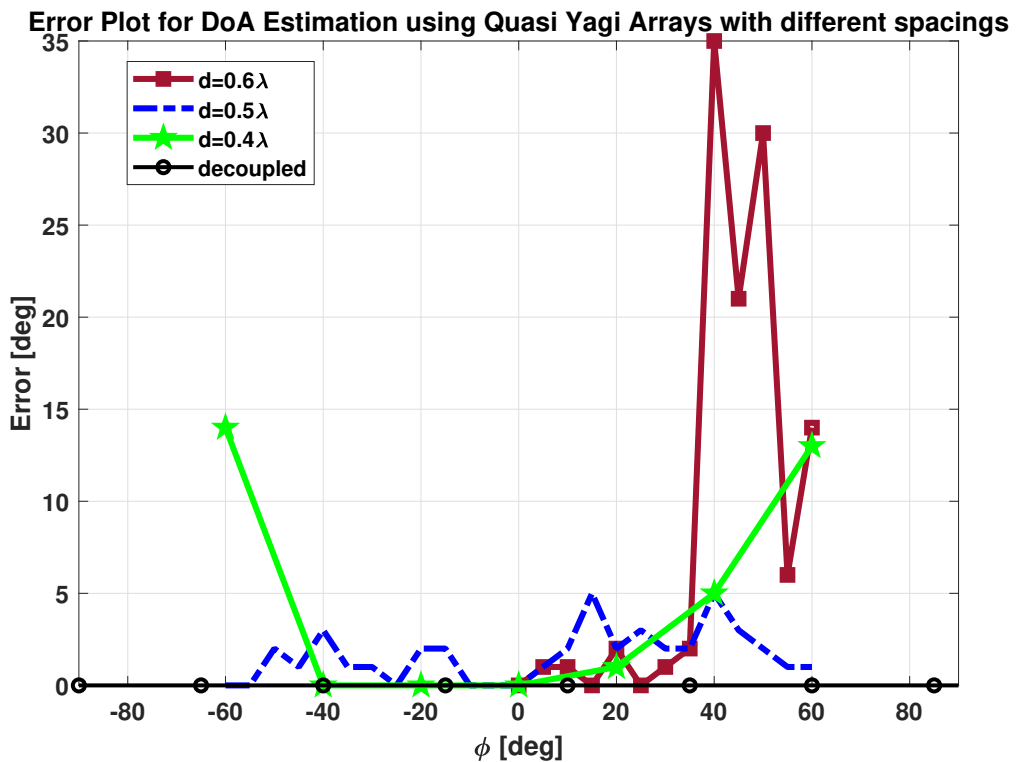
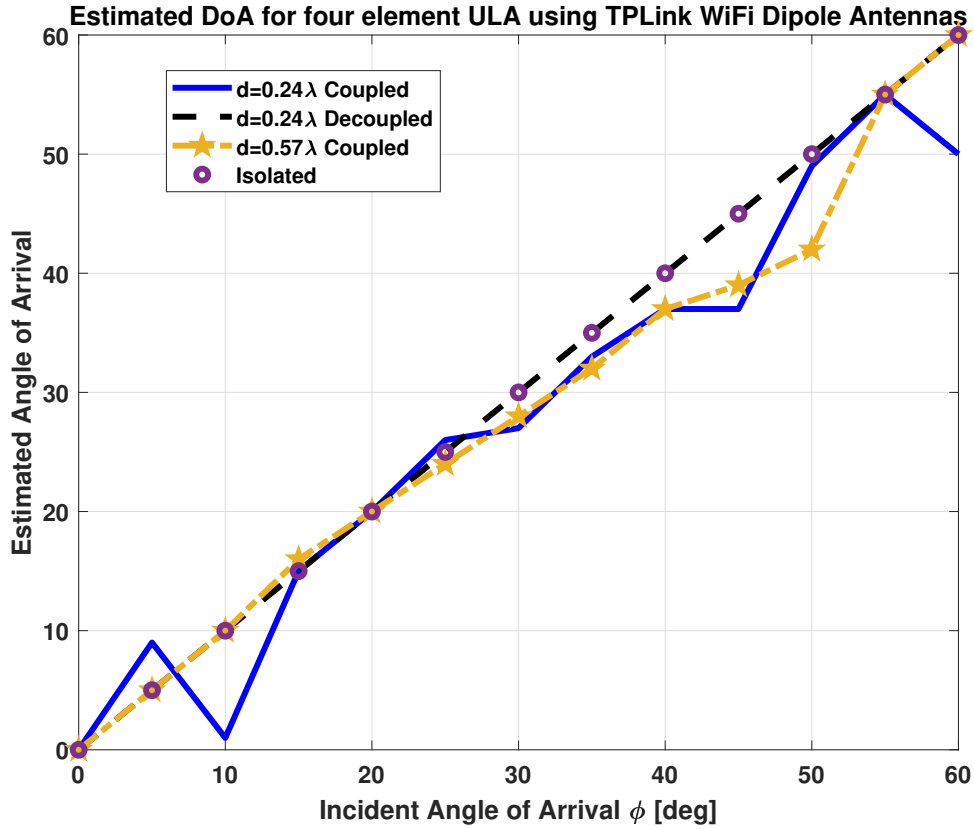


Figure 4.21: Error plot for estimated DoA in the presence of coupling for 3 different spacings  $0.6\lambda$ ,  $0.5\lambda$  and  $0.4\lambda$  for quasi yagi array.

is evident by the error plot which is zero degrees.

Similarly, for TPLink array shown in **Figure 4.7**, two different spacings  $0.24\lambda$  and  $0.57\lambda$  were considered. The estimated DoAs are shown in **Figure 4.22**.



**Figure 4.22:** Estimated DoA in the presence of coupling for two different spacings  $0.24\lambda$  and  $0.57\lambda$  for TPLink dipole array.

For the quasi yagi array shown in **Figure 3.18**, a similar plot is shown in **Figure 4.23**. It is seen that the detection range in the presence of coupling is limited to  $\pm 20^\circ$  when the spacing is  $0.24\lambda$  as compared to the compensated voltages which has a full range.

The system specifications for this experiment are shown in **Table 4.3**.

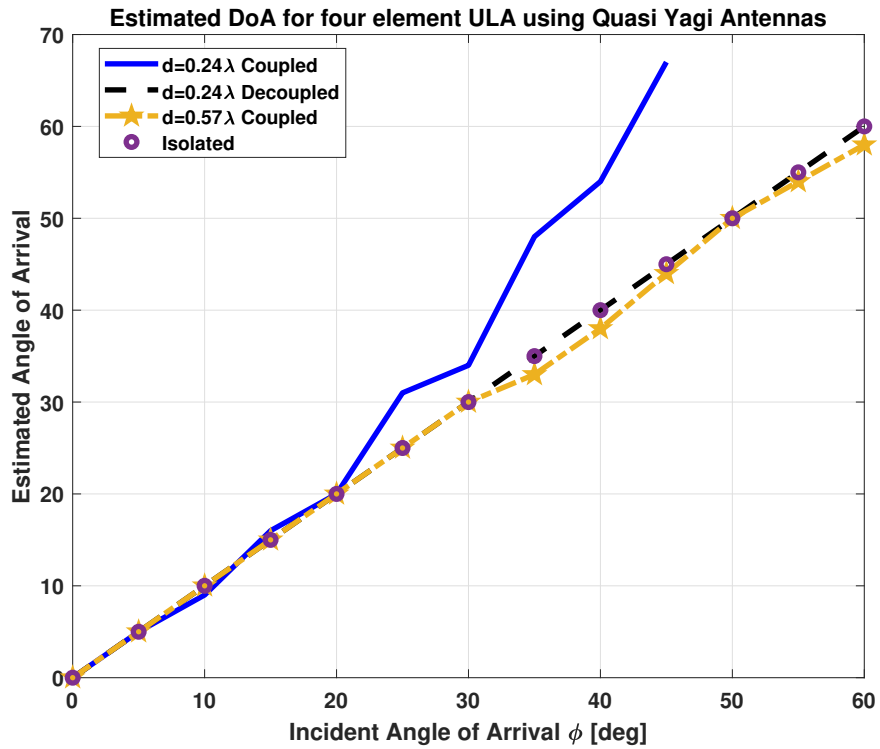


**Figure 4.23:** Estimated DoA in the presence of coupling for two different spacings  $0.24\lambda$  and  $0.57\lambda$  for printed quasi yagi array.

**Table 4.3:** System specifications for the receiver array for study of DoA vs. different antenna spacing.

Item	Details
SDR	AD FMCOMMS5 Radio + ZC706 Xilinx FPGA
Antenna array	Printed quasi yagi, TP-Link dipole, commercial quasi yagi
Array spacing	$0.24\lambda$ $0.57\lambda$ , $0.24\lambda$ $0.57\lambda$ , $0.4\lambda$ $0.5\lambda$ $0.6\lambda$
Samples per frame	4000
Frame time	4 ms
Total frames	1251
AGC Mode	Manual 30 dB Range = -10 to 76 dB
Platform	MATLAB GbE LAN

### 4.3.3. Conclusion

In this study, a compact experimental system was designed to measure DoA for different ULA spacings and antenna types after real-time MCC. A total of 3 different antenna array setups were used in which two were directional quasi yagi antenna arrays and one was omni-directional dipole antenna array. Similarly, for the transmitting source directional and omni-directional antenna were used. We conclude that for omni-directional or directional antennas mutual coupling can be compensated accurately and the DoA can be estimated in run time. A study of DoA vs spacing was also conducted for the above array setups. After decoupling the received voltages it is observed that the estimation range of DoA is increased as expected for all array setups. Also, it has been shown that  $0.5\lambda$  is the optimum spacing in the presence of coupling for directional antennas since it gives the best estimation range and minimum error which is a reason for most DoA applications this spacing is recommended. However, in this work we have successfully shown that any antenna type, directional or omni-directional, with any spacing can be made optimum for the application at hand by compensating for mutual coupling using the aforementioned methodology.

#### 4.4. Algorithm III: IEEE 802.11a SIMO End-to-End Transceiver Implementation On Xilinx® Zynq® FPGA And An Analog Devices™ FCOMMS5 Radio With Mutual Coupling Compensation For Spectral Efficiency Application

##### 4.4.1. Experimental Results

Here, we will be discussing the experimental results for the SIMO end-to-end transceiver implementation on SDR. In this setup we will transmit an image using PLUTO SDR implementing WLAN with a single transmit antenna and receive it on FCOMMS5 SDR with four receiver antennas. Since the ULA is spaced at  $d=0.24\lambda$  the coupling is high and therefore we expect that the Packet Error Rate (PER) will be high. However, after implementing the compensation algorithm, the PER should decrease and the image should be recovered. In this section three different scenarios would be discussed and the performance metrics will be shown for each case.

##### 4.4.2. Received WLAN waveform for a ULA with spacing $d=0.24\lambda$

The received signal for the coupled case can be seen in **Figure 4.24**. This is the real-time signal that has been captured which shows one of the received WLAN packets randomly. There are a total of three subplots in this figure. The top subplot shows the received WLAN packet in frequency domain. The spectrum shows that four distinct signals have been received since there are four channels and the maximum power received is of channel 1 at -70 dBm and minimum power level is of channel 4 at -85 dBm approximately whereas the noise floor is around -110 dBm. The different levels of the signal indicate the noisy environment and the presence of coupling. The subplot to the right with yellow scrambled points show the constellation diagram for one of the received channels. In this case, channel 1 is being shown. It can be observed that due to coupling the signal could not be recovered therefore the 64-QAM equalized symbols cannot be received. Also the time domain I/Q signals are shown for the four channels in the subplot to the left with multi color plots. There are a total of eight I/Q plots in this figure ( two for each channel ). The amplitude of these signals are varying with maximum at +/- 0.06 V and minimum at +/- 0.01 V. After applying the compensation algorithm, it was observed that the received signal had an SNR increase and therefore was able to recover the image entirely. The result can be seen in **Figure 4.25**. The power spectrum of the signal shows four equal amplitude signals

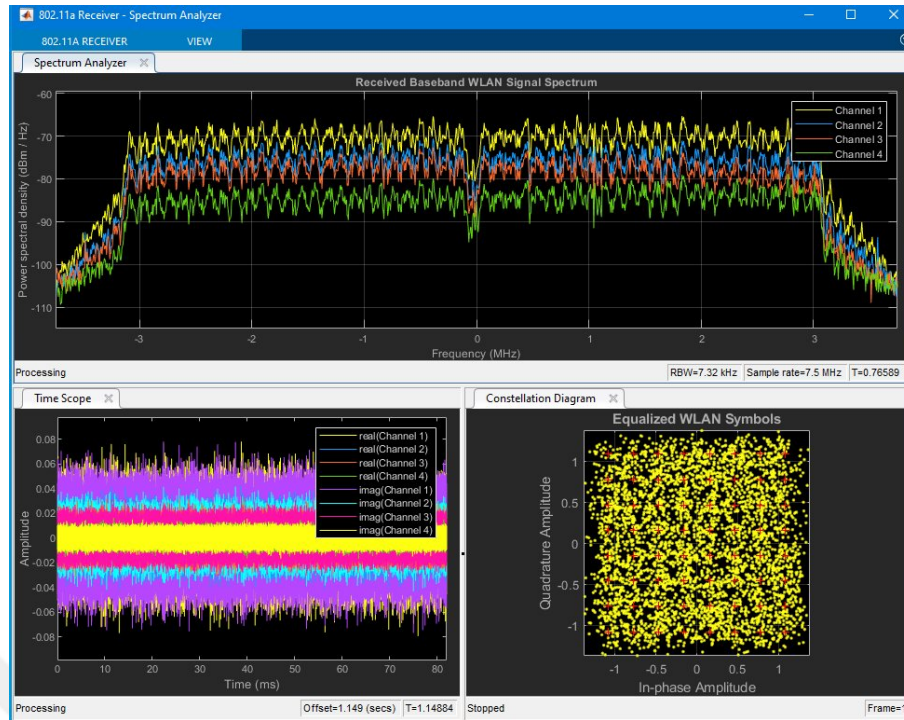


**Figure 4.24:** Received WLAN packet in the presence of coupling for four-element Quasi Yagi ULA with spacing  $d=0.24\lambda$ .

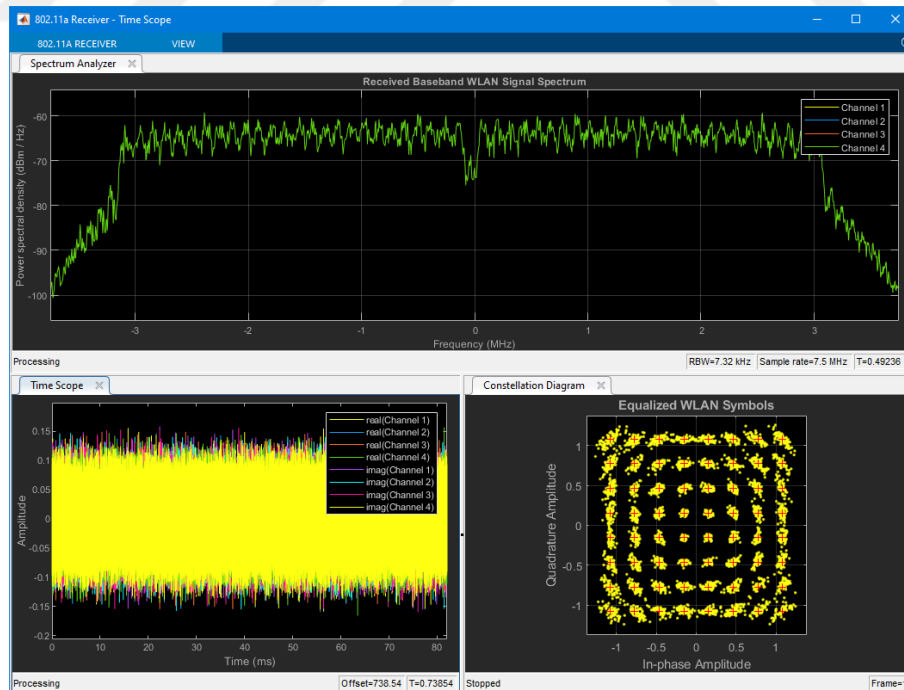


**Figure 4.25:** Received WLAN packet after compensation for four-element Quasi Yagi ULA with spacing  $d=0.24\lambda$ .

whereas in the coupled case we could distinctly see the four different amplitudes. In other words, the four signals are on top of each other with maximum power level around -60 dBm approximately and noise floor at -100 dBm. Here it should be mentioned that even though the SNR for both cases is the same since the difference is 40 dB between the signal power level and noise floor, it is clearly evident that channels 4, 3 and 2 had a boost in power levels as compared to the coupled case. The constellation can be observed clearly in the right subplot showing the 64-QAM being recovered as opposed to the coupled case where it was completely abstruse. Furthermore, the time domain I/Q signal amplitude has been increased to  $\pm 0.1$  V for all the eight I/Q signals instead of randomly varying amplitudes in the coupled case. All these representations of the received WLAN packet in **Figure 4.25** determine the accuracy and the superiority of this algorithm.

#### **4.4.2.1. Performance analysis of the received WLAN signal before and after compensation**

Here, we will observe the different performance metrics for the received signal such as SNR, EVM, channel capacity, PER and the received image itself. Since the transmitted WLAN packets for the image are 11 in number we transmit five times this data which is repeated continuously therefore at the receiver 55 packets are received at one RF capture. These received packets are then given as an input to the decoder which decodes and then sequences these packets in the correct order in order to reproduce the transmitted image. Therefore, the same image is sent five times in one transmit RF burst and this process is continued till the receiver captures the intended length of RF signal. Furthermore, in order to visualize the effect of MC and compensation the contents of each packet are analyzed and its metrics are computed. Here, for a random packet the constellation along with the time and frequency domain representations of the decoded WLAN packet will be presented for the coupled and compensated case.

#### **4.4.2.2. SNR and PER**

The channel estimation, fine frequency offset estimation, and fine symbol timing offset estimation rely on the L-LTF. Using this field, for every packet we can estimate the signal power as well as noise power. L-LTF has two OFDM symbols. In order to estimate the mean noise power in Watts we use the demodulated L-LTF symbols assuming 1 ohm



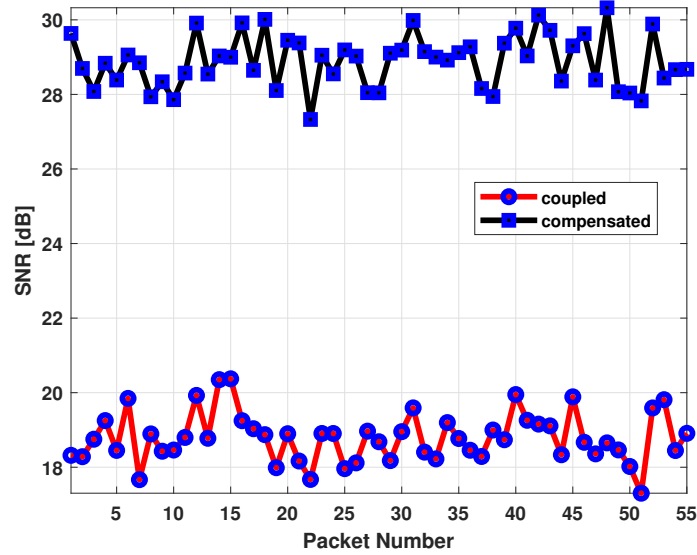


**Figure 4.26:** SNR comparison of received coupled and compensated WLAN packets.

resistance. The estimated noise power in non-HT packet is averaged over the number of receive antennas. It should be noted here that the demodulated L-LTF corresponds to the frequency-domain signal. There are total 52 subcarriers in each OFDM symbol therefore L-LTF will be a  $52 \times 2$  matrix. The signal power is calculated using the L-LTF again but using the corresponding time-domain signal. In our case, the number of samples in one OFDM symbol are 80 therefore we have 160 samples for L-LTF. Hence, SNR is computed after estimating the signal power and noise power. This process is done for every WLAN packet received. **Figure 4.26** shows the SNR vs received packets for coupled and compensated case. Since there are 55 packets in one burst we can see that x-axis corresponds to received packets. The results show a clear 10 to 12 dB of increase in SNR. By using Shannon's capacity theorem in order to calculate the maximum data rate for a noisy channel:

$$Capacity = BW * \log_2(1 + SNR) \quad (4.1)$$

Here, BW is the bandwidth of the channel and SNR is the signal to noise ratio in linear scale. Since the BW is a fixed quantity, therefore it is evident that the capacity is directly proportional to the power of the signal. The PER is shown for the coupled and compensated case in **Figure 4.27**. In the coupled case the image could not be received from the received equalized symbols whereas after compensation we were able to receive the image as shown in **Figure 4.28**.

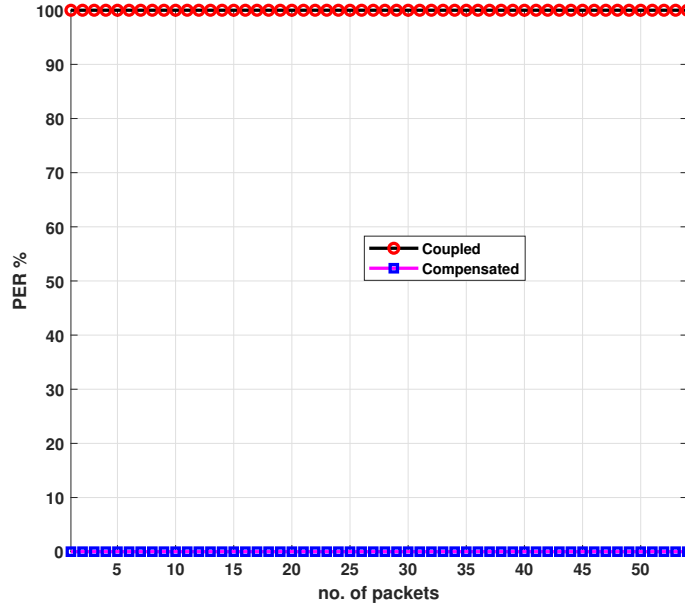


**Figure 4.27:** PER comparison of received coupled and compensated WLAN packets.

#### 4.4.2.3. EVM

Since OFDM modulation is being used we have total 52 subcarriers amongst which 48 of them are data subcarriers and 4 of them are pilot subcarriers. EVM helps us to measure the deviation of the received equalized constellation symbols from their ideal location. **Figure 4.29** shows EVM in dB scale vs. data subcarriers for a single WLAN packet. The lower the value of EVM the better is the performance of the receiver and hence lower the deviation. A 10 dB difference can be observed between the coupled and compensated case. Similarly, in time domain, we have a total of 92 OFDM symbols in every WLAN packet in which 5 are preamble symbols and 87 are data symbols. For packet 33 the EVM vs symbols in time domain is plotted in **Figure 4.30** which also shows the same 10 dB improvement. Overall EVM of a receiver can be defined by combining all contributions of error sources. Thus EVM can be defined as a function of SNR, Image Rejection Ratio (IRR) and LO Leakage Suppression (LLS).

$$EVM = \sqrt{\frac{1}{SNR} + \sigma_{\theta}^2(1 + LLS.X) + LLS + IRR^2} \quad (4.2)$$

The relationship between EVM and SNR for a 64-QAM signal is given by

$$SNR = - \left( 3.7 + 20 \times \log_{10} \left( \frac{EVM}{100\%} \right) \right) \quad (4.3)$$

a)



b)

No Sequence Found : PER 100 % !  
Could not receive the image !

**Figure 4.28:** Received decoded Image **a)** after compensation, **b)** in presence of coupling.

Here, 3.7 represents the peak to average power ratio (PAPR) in dB, EVM is voltage ratio therefore we use  $20 \log_{10}$  to get power ratio. Since SNR is signal to noise ratio and EVM is noise to signal ratio therefore we use the minus sign.

#### 4.4.2.4. Channel Capacity

As mentioned in **Subsection 4.4.2.2**, the channel capacity is directly proportional to the SNR of the received signal. In this experiment, we observe that there is an increase in channel capacity by around 3.5 bps/Hz. In [95], we presented an increase in channel capacity by 2 bps/Hz using EM simulation for NOMA whereas here we have demonstrated an experimental verification of a SIMO transceiver using OFDM with 64-QAM modulation. The theoretical channel capacity can be observed in **Figure 4.32** for different systems such as SISO, SIMO, MISO and MIMO. It can be observed that for a SIMO system the channel capacity increase is 3.5 bps/Hz when the SNR is increased by 10 dB from

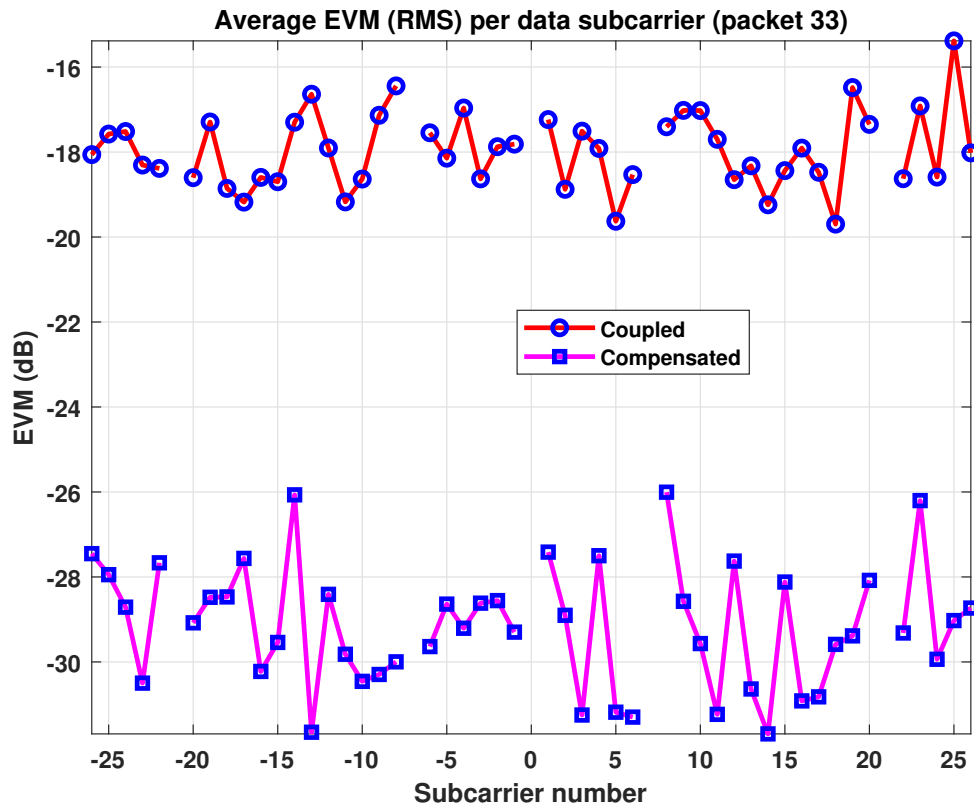


**Figure 4.29:** EVM vs subcarriers comparison of received coupled and compensated WLAN packets.

20 to 30 dB for the coupled and compensated cases respectively as shown in **Figure 4.26**.

#### 4.4.2.5. Comparison of a random WLAN packet for coupled and compensated case

Here, we will randomly pick one of the WLAN packets and analyze it to observe the effect of compensation and coupling. A random packet 33 has been picked out of the 55 packets and the signal metrics have been compared for the coupled and compensated case. The time domain burst, Power Spectral Density (PSD), and constellation can be seen in **Figure 4.33**, **Figure 4.34**, and **Figure 4.35**. The time domain packet shows -15 dBm of received power whereas after compensation it is around 5 dBm of received power. Similarly, for the PSD we can see power level of -50 dBm for the coupled case and -30 dBm for the compensated case. The received equalized data symbols cannot be determined in the coupled case whereas after compensation we can observe a clear 64-QAM constellation. It can be seen clearly from all these plots that after compensation there is a gain achieved resulting in the recovery of the data received. The image has

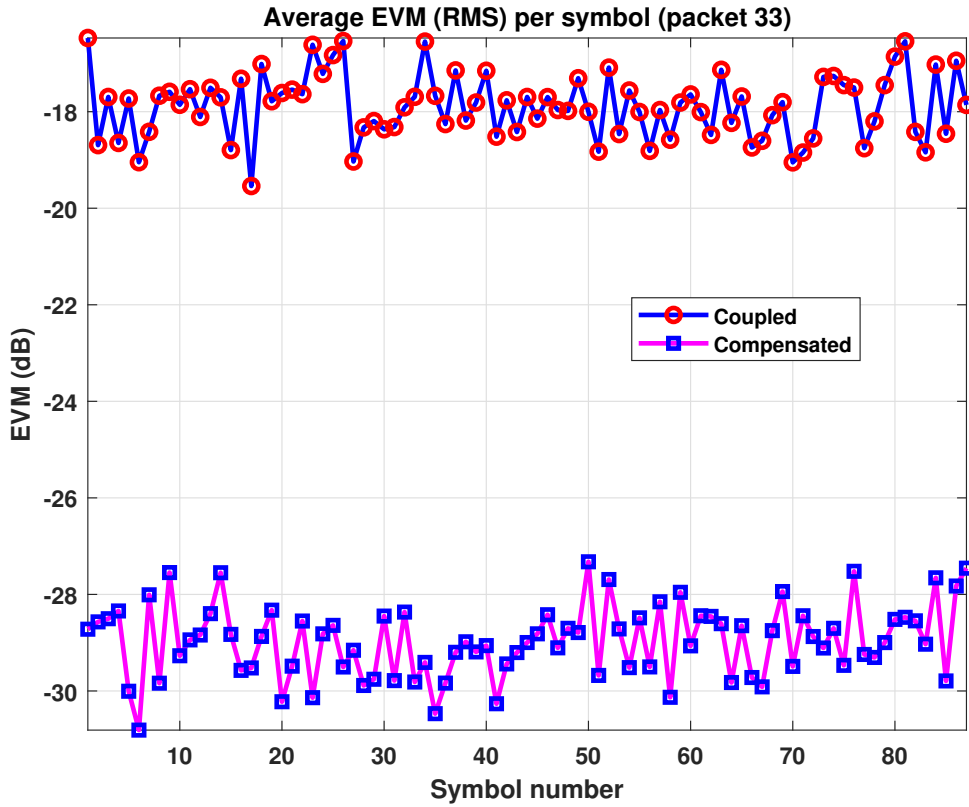


**Figure 4.30:** EVM vs symbols comparison of received coupled and compensated WLAN packets.

been successfully recovered after the compensation algorithm has been applied where as in the presence of coupling there was a 100% PER due to which none of the packets were decoded and thus image was not received for the coupled case as showed in **Figure 4.28**.

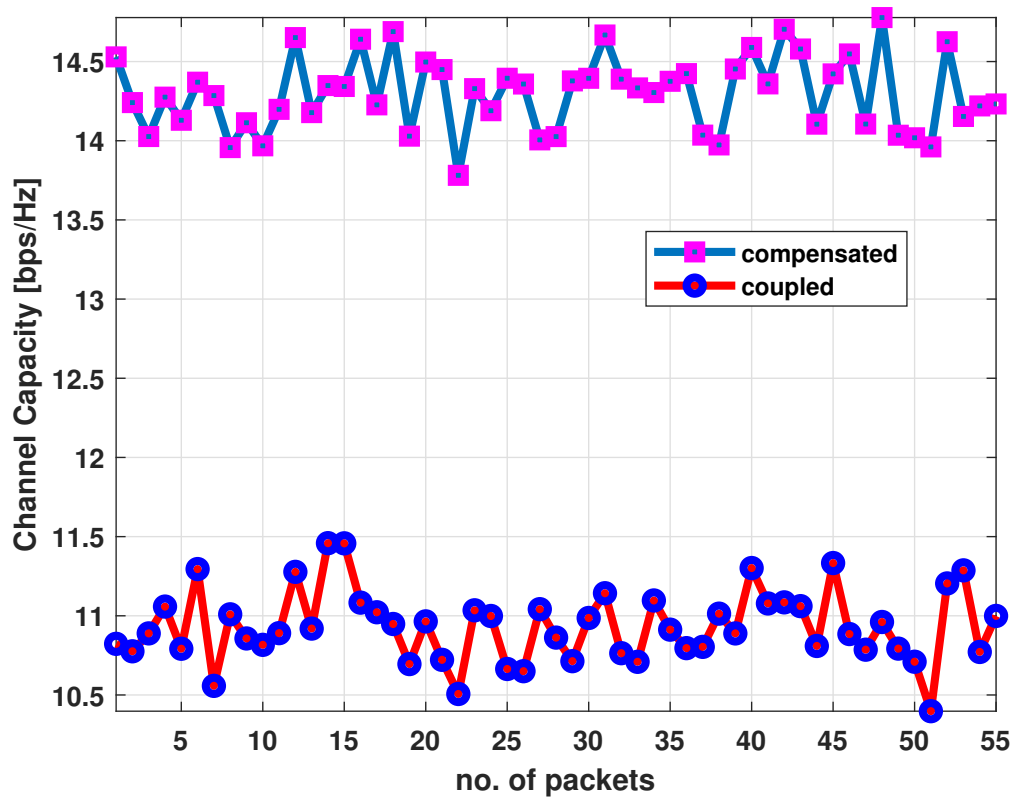


Figure 4.31: Channel capacity comparison of received coupled and compensated WLAN packets.

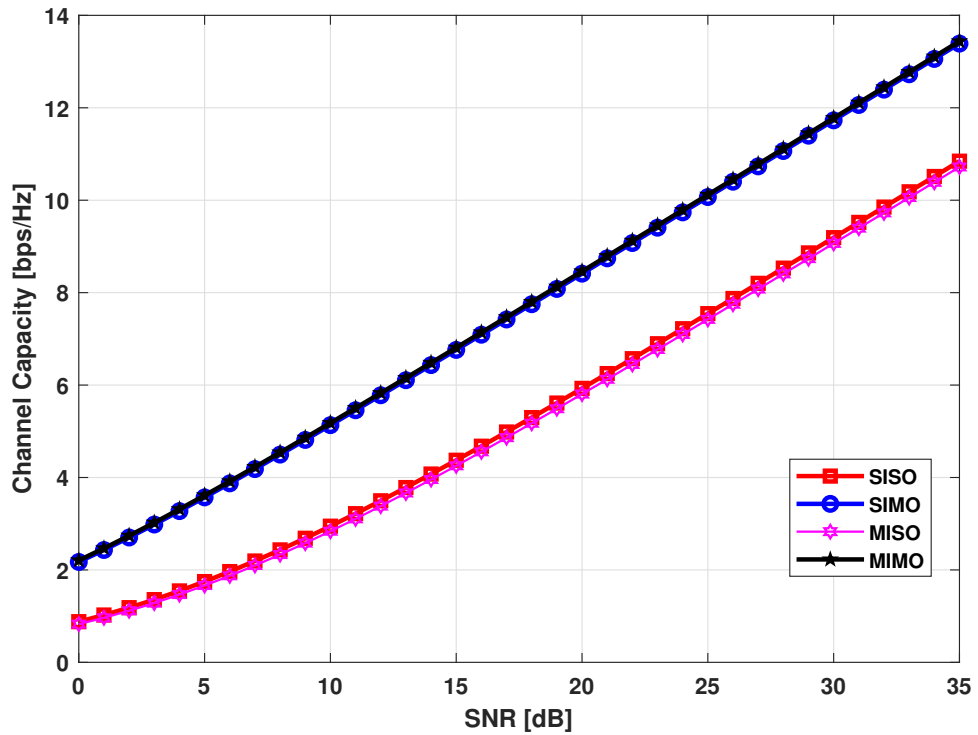
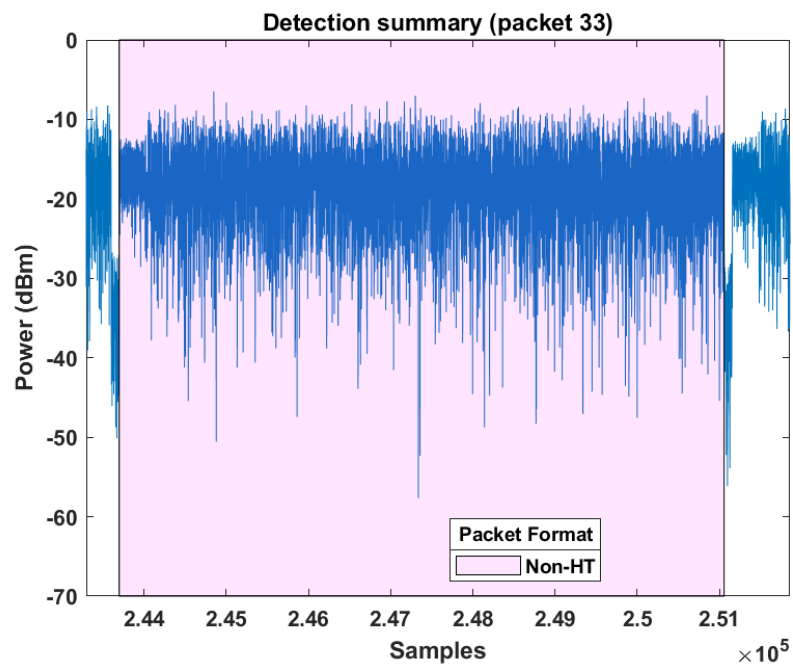


Figure 4.32: Theoretical channel capacity for SISO, MISO, SIMO and MIMO systems.

a)



b)

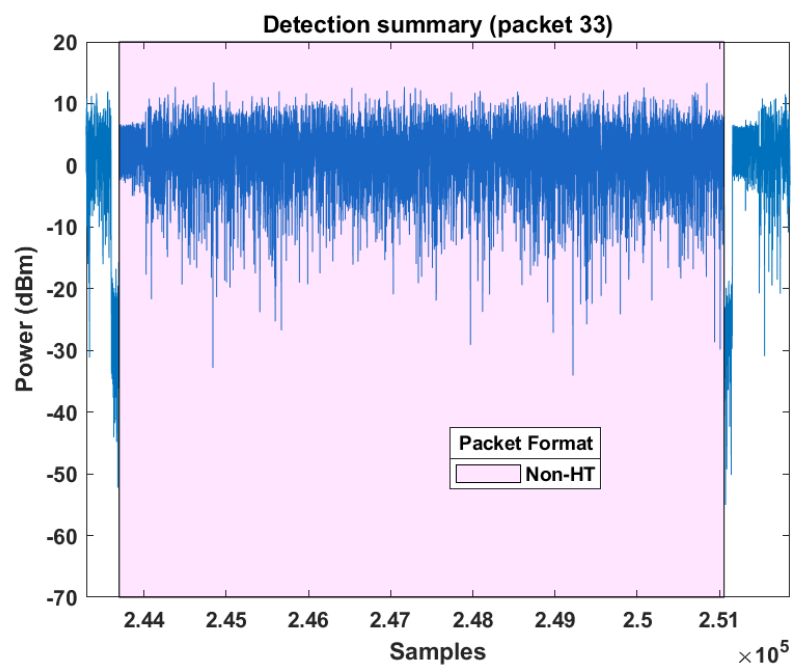
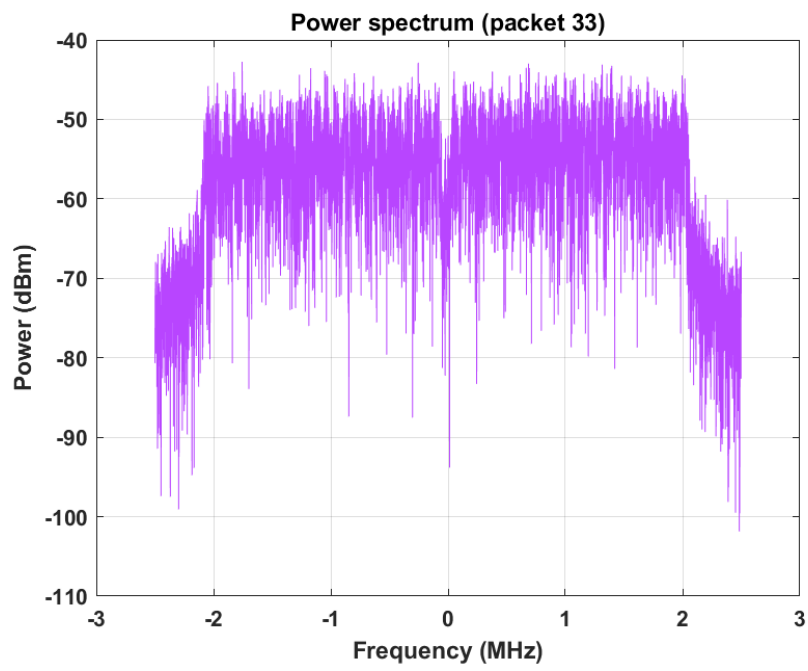


Figure 4.33: Time domain burst of received packet no. 33: a) coupled, b) compensated.

a)



b)

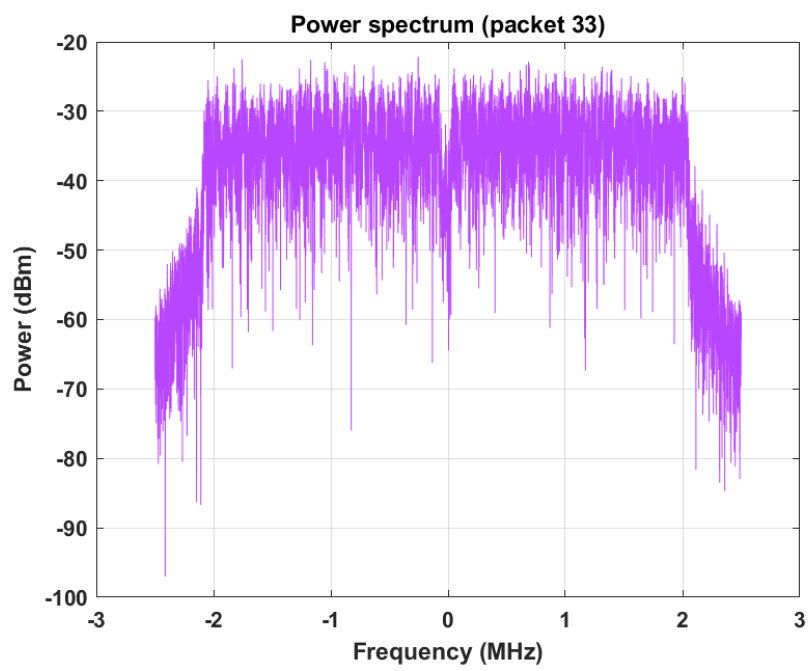
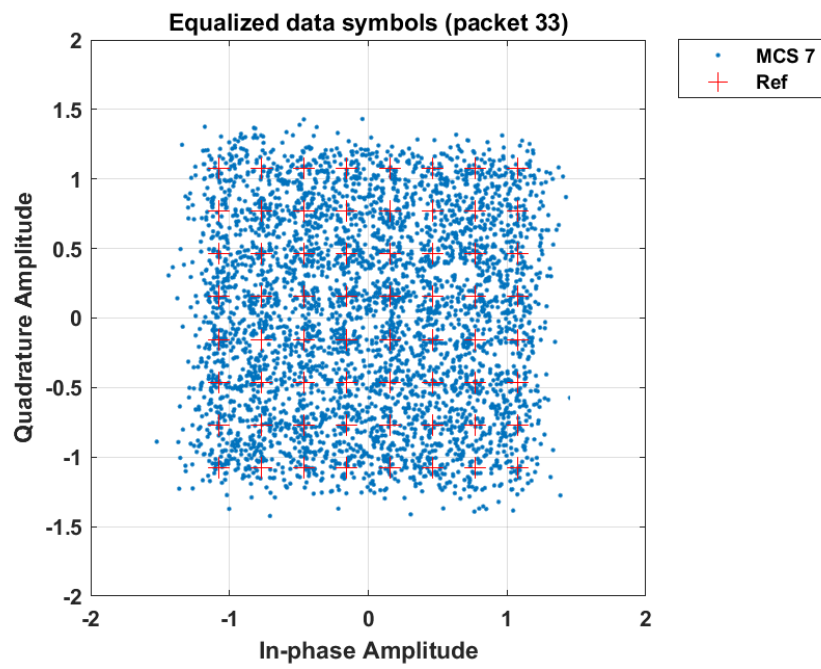


Figure 4.34: Power spectrum of received packet no. 33: (a) coupled, b) compensated.



a)



b)

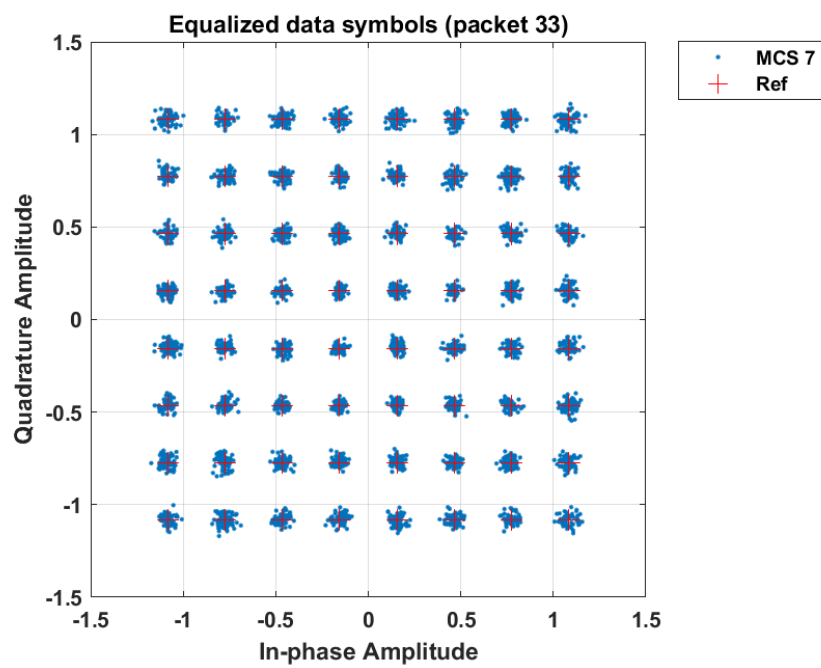


Figure 4.35: Constellation of received packet no. 33: a) coupled, b) compensated.

#### 4.4.3. Comparison of optimally spaced vs. coupled spaced ULA

In this section, we compare the received signals for optimally spaced i.e.,  $d = 0.5\lambda$  ULA and coupled ULA with  $d = 0.24\lambda$  spacing. In the literature, most of the antenna arrays are spaced with  $d = 0.5\lambda$  spacing since MC is considered to be weak at this spacing therefore it is the optimal or standard spacing. Due to this assumption, MC is mostly neglected and not compensated for however it can be shown that compensation can provide better results than neglecting it. When the spacing is reduced, the effect of MC is more pronounced.

When the transmit power is fixed to -15 dB and the receiver gain is fixed for the setup **Table 4.4:** Comparison of  $d = 0.5\lambda$  and  $d = 0.24\lambda$  spaced ULA in presence of coupling with Tx power -15 dB.

Spacing	SNR [dB]	EVM Sym [dB]	EVM dsc [dB]	PER %	Channel Capacity [bps/Hz]	Image De-coded	Rx Gain Mode
0.5 $\lambda$	25	-23	-23	14.54	14.54	Yes	AGC Fast Attack -12dBFS fixed
0.24 $\lambda$	17	-18	-18	100	11.5	No	AGC Fast Attack -12dBFS fixed

shown in **Figure 3.34**, the received signal metrics for the optimal spacing and coupled spacing can be observed in **Table 4.4**. In order to reduce repetition by displaying all the plots as shown in **Subsection 4.4.2**, the results have been tabulated and the mean value is displayed for the various performance metrics. The results are presented in the presence of coupling for both cases. The highlighted green shows that the results are satisfactory and the red one shows that results are erroneous. In other words, when the spacing is half a wavelength which is the case for most of the commercial applications like WiFi routers, the SNR, EVM, channel capacity all are acceptable values since that is the reason why these systems work. However, for the same array, when the spacing is decreased and received signal is compared we can see that SNR, EVM and channel capacity all have

been degraded as compared to the optimal spacing. Furthermore, the PER which shows the packet error rate is a 100 % in the case when the coupling is high and for optimal spacing we still have 14 % PER. This shows that even in optimal spacing coupling factor is still there however it is not very high therefore we are able to decode the image whereas in the latter case we are unable to decode the received image. This is a compromise we accept since we are able to recover the data but the received data deteriorates when the Received Signal Strength Indicator (RSSI) is low.

#### 4.4.4. Comparison of optimally spaced ULA at low RSSI

In the previous section it was observed that when the spacing is  $d = 0.5\lambda$  for the ULA the received signal can be recovered although many packets need to be received in order to mitigate for the errors as observed in the PER. However, when the RSSI is low the compensation algorithm works better for such signals because it gives a signal boost by increasing the amplitude of the signal. In this case, the transmitted power is fixed to -20 dB and again the receiver gain is fixed. For the optimal spacing, we have the coupled case and compensated case as shown in **Table 4.5**. A comparison of the tabulated results show that after compensation the performance metrics have increased significantly.

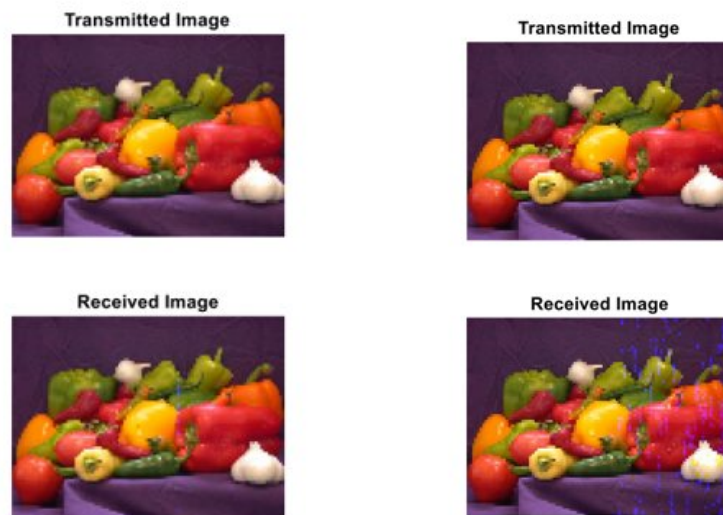


**Figure 4.36:** Comparison of received images **a)** compensated case, **b)** coupled case for  $d = 0.5\lambda$  ULA with low RSSI.

It can be observed that not only was the SNR increased but the channel capacity as well as PER was improved significantly although both were able to recover the image. There

is an increase of about 6 dB for the SNR and EVM whereas the PER has been decreased from 30 % to 16 % and an increase in channel capacity by 2 bps/Hz. The received image in **Figure 4.36** shows that even though the coupled image was received but due to packet errors some data is missing which is visible due to the blue marks.

**Table 4.5:** Comparison of  $d = 0.5\lambda$  ULA with low RSSI and Tx power -20 dB.

Category	SNR [dB]	EVM Sym [dB]	EVM dsc [dB]	PER %	Channel Capacity [bps/Hz]	Image De-coded	Rx Gain Mode
<b>Compensated</b>	26.78	-26	-26	16.81	14.59	Yes	AGC Fast Attack -12 dBFS fixed
<b>Coupled</b>	21.17	-20	-20	30	12.7	Yes	AGC Fast Attack -12 dBFS fixed

The RSSI indicates the power present in the received signal therefore in such scenarios when the user is away from the coverage area of the Base Station (BS), then other techniques such as Reconfigurable Intelligent Surfaces (RIS) systems can be deployed as discussed in [1]. Since the basic idea of an RIS system is to collect wireless signals from a transmitter and passively beamform them towards the receiver without adding extra input power using complex RIS structures. The compensation technique mentioned in this work has similar results to that of an RIS system since it also involves passive beamforming of the received signal in the software domain thus eliminating the expense and use of complex RIS systems and therefore this method can be proposed as an alternative.

#### 4.4.5. Different Array Setup Types

Apart from the setups discussed, we also tested the setup for different sets of antennas and geometrical configurations. Up till now, we have been using ULA only but we also

tested UCA. However, the  $Z$  matrix for UCA is different than the ULA thus a different predefined mathematical model can be derived. In this section, we would be showing the different types of antennas that were used in both UCA and ULA geometry.

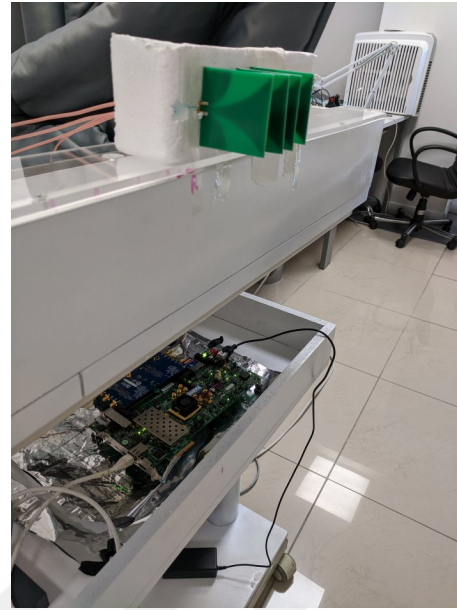
#### 4.4.5.1. ULA

The hardware allows us to work at wide band RF with frequencies ranging from 70 MHz to 6 GHz. This gave us the opportunity to test a multitude of antennas for MCC with different spacings. A total of five different array setups were tested including fractal antennas, circular patch antennas, elliptical patch antennas, vivaldi antennas, quasi yagi antennas and TPLink dipole antennas. The setups are shown in **Figure 4.37**. Different transmitter antennas were used as shown in **Figure 4.38** which included directional as well as omni-directional antennas namely log periodic, vivaldi, dipole and teardrop antenna. The teardrop antenna was fabricated at IMU whereas all the rest were commercial antennas.

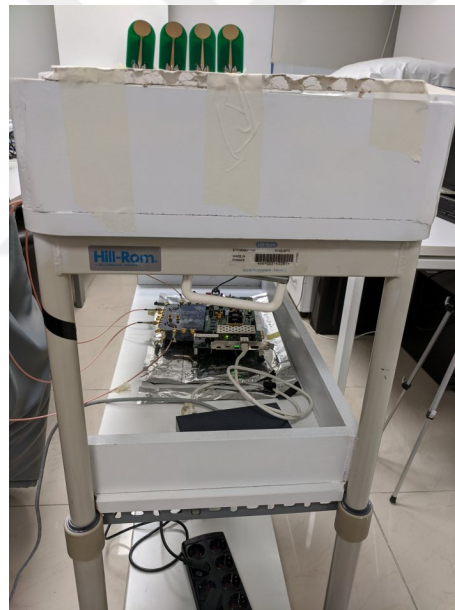
a)



b)



c)



d)



**Figure 4.37:** Different antenna arrays used for this experiment **a)** fractal antennas at  $f=1$  GHz and  $d = 0.33\lambda$ , **b)** vivaldi antennas at  $f=3.7$  GHz and  $d = 0.28\lambda$ , **c)** circular patch antennas at  $f=4.55$  GHz and  $d = 0.37\lambda$ , **d)** wideband vivaldi antenna at  $f=5.95$  GHz and  $d = 0.4\lambda$  ULA.

a)



b)



c)



**Figure 4.38:** Different transmitting antennas used for this experiment **a)** log periodic, **b)** tear drop, **c)** vivaldi.

#### 4.4.6. UCA

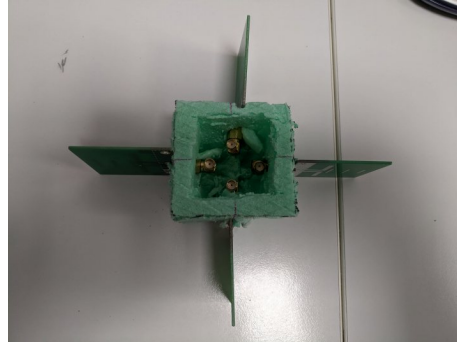
A four element UCA of Quasi Yagi antennas arranged at a radius of  $\lambda/4$  mounted on a styrofoam board can be seen in **Figure 4.39**. The complete setup can be seen in **Figure 4.39c** which was designed using off-the-shelf material so a UCA could be realized. A simple styrofoam material was first cut in a cube shape and then the bottom side was hollowed as seen in **Figure 4.39b**. The antennas were connected to 90 degree SMA connectors. The frequency was 2.468 GHz and the distance between the transmitter and receiver was kept greater than  $40\lambda$  to be in the far-field. Due to the versatility of the test-bed different array geometries could be realized easily. Since the RFFE has four receivers thus only four SMA cables are required to mount the new setup. In terms of the algorithm, since this is UCA the Z matrix will no longer be similar to that calculated for a ULA however the computation steps are similar. Thus, we are able to compute the predefined Z matrix which was derived as a result of experiment and then model-fitted to a set of equations such that they can be computed on the go. The input to the function is the radius and the number of antennas which will result in the output Z matrix for different incident angles. The same application of image reception using WiFi standard was applied in order to test this algorithm. After receiving the RF burst, MCC was applied and then the data was given as an input to the decoder. The results for the coupled and compensated received signals can be seen in **Figure 4.40**. Since all elements in a UCA experience similar coupling with their neighbours as expected due to symmetry thus the coupled signals in power spectrum show almost equal power levels. However, after compensation a recovery of the equalized symbols show the efficacy of the algorithm.



a)



b)

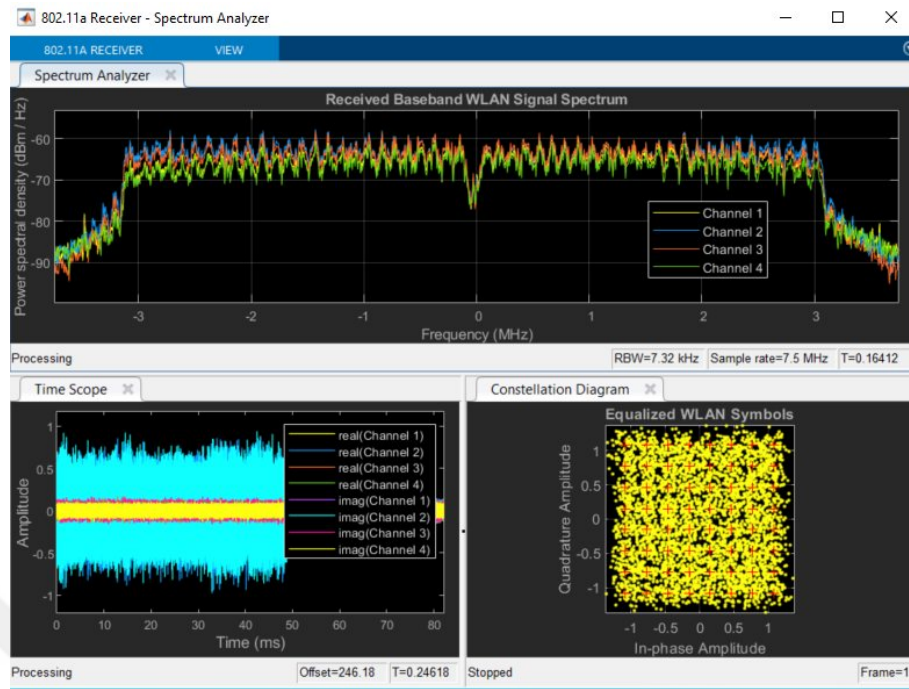


c)



**Figure 4.39:** UCA of quasi yagi antennas arranged at radius  $\lambda/4$  **a)** top view, **b)** bottom view, **c)** complete setup.

a)



b)

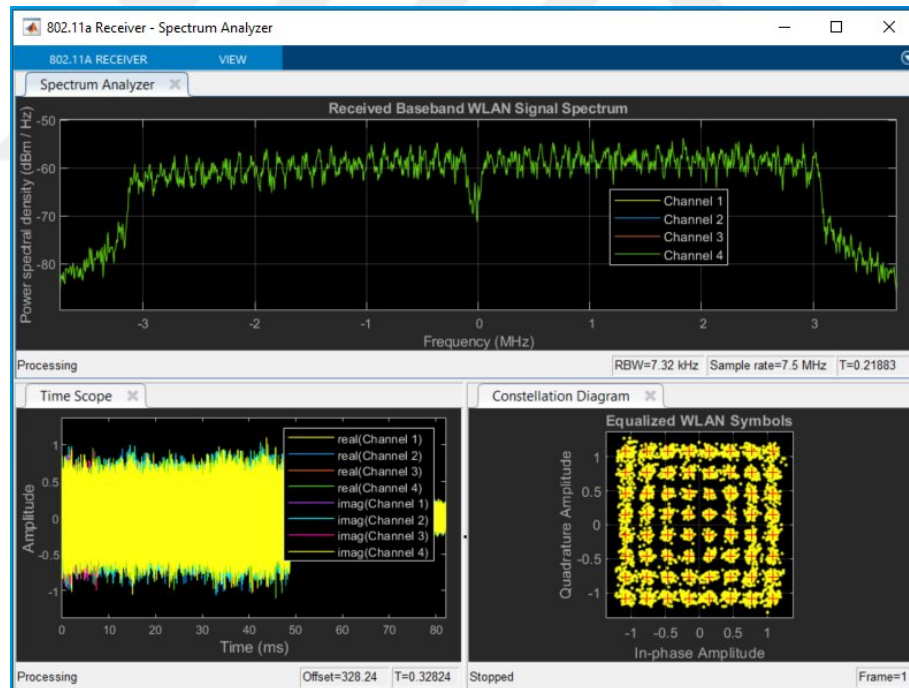


**Figure 4.40:** Received signal for an IEEE 802.11a SIMO transceiver implementation for a UCA of quasi yagi antennas arranged at radius  $\lambda/4$ . (a) in presence of coupling, (b) after compensation.

#### **4.4.7. Conclusion**

A SIMO End-to-End Transceiver using IEEE 802.11a WiFi standard was implemented on SDRs with four channel array and mutual coupling compensation algorithm was applied in real-time DSP. An image was transmitted using WLAN and the ULA with different spacings were used to receive the image. It was observed that in the presence of coupling the image could not be recovered due to 100% PER however after compensation the same received data could not only recover the image but there was an SNR increase of 10 dB. Different performance metrics such as channel capacity, EVM, SNR and PER were shown for individual WLAN packets. A study was shown on the effect of mutual coupling on optimally spaced arrays at high and low RSSI. Different antenna arrays with different antenna spacings were tested to confirm the validity of the algorithm thus concluding that antenna distance is not a limitation. After conformity of the results using ULA, a UCA was designed and tested for MCC. A mathematical model was developed for the ULA and UCA geometries which results in pre-calculated decoupling matrices. In conclusion, all the experiments proved that the compensation algorithm is superior to other algorithms due to its simplicity in computation and applicability at any receiver array.

## CHAPTER 5

### 5. CONCLUSION AND FUTURE WORK

Mutual Coupling in antenna arrays is a problem that has been studied for decades and different solutions have been developed in the course of this research. This thesis also addresses the same problem but with an experimental approach where coupling can be compensated in real-time for different applications. A formulation for mutual coupling compensation is presented for Uniform Linear Array (ULA) and Uniform Circular Array (UCA) along with experimental verification of the formulation using phased array test-beds utilizing Software Defined Radios (SDR). Two different formulations and two different experimental test-beds were developed for the verification of mutual coupling compensation and Directional of Arrival (DoA) estimation. The new setup increased mobility by reducing the hardware involved and also reduced the cost of the overall system. It was shown experimentally that mutual coupling can be compensated for antenna arrays that are placed as close as  $0.24\lambda$  in an indoor environment without the use of an anechoic chamber using the test-bed setup developed. Directional and omni-directional antennas in ULA or UCA were tested. The antenna arrays were used with spacing that varied from  $0.24\lambda$  to  $0.6\lambda$  to study the effect of DoA with spacing. Direction finding was estimated using well known algorithms such as MUSIC, Root MUSIC, ESPRIT, MVDR (Capon), Beam Scan and Beam Space ESPRIT Estimator. The results showed that DoA can be estimated with full accuracy in an indoor environment after coupling is removed using a decoupling matrix which can be calculated both online and offline methods. Another application to observe the effect of coupling and compensation on data rates and channel capacity was implemented using IEEE 802.11a WiFi standard for a SIMO (single Input Multiple Output) End-to-End Transceiver Implementation on SDR with mutual coupling compensation. The transmitter sends an HD picture using the 802.11a standard and the

receiver decodes the data in the presence of mutual coupling and after compensation in real-time. Different signal metrics like SNR, PER, EVM, Channel Capacity are discussed along with the visualization of the effects of mutual coupling and its compensation in both time and frequency domain. The results show that at low SNR values the received signal can have a 10 dB SNR gain after using the compensation algorithm. A mathematical model using a closed-form equation for the coupling has been developed for ULA and UCA geometries which can be pre-calculated for any system irrespective of the antenna type in the array. Commercial WiFi routers and military systems such as radars which use huge number of arrays or MIMO BS coupling compensation can be easily implemented without modifying the system in anyway. The computational complexity is only a single matrix multiplication. The effect of MC which is usually neglected during array processing was emphasized in this thesis with various experiments including direction finding and spectral efficiency computations. The result of all experiments deduce the undesirable effect of MC and excellent performance after compensation. A comparison of different techniques for real-time compensation which was not limited to simulations but was backed up with experimental verification using a multitude of hardware test-beds provide a complete RF system design approach. This kind of approach is usually lacking in many dissertations where all emphasis is placed on the theoretical and simulations part only. In conclusion, a simplistic and hands-on approach was presented for real-time MCC that can be easily implemented for different antenna arrays and configurations.

### **5.1. Future Work**

The study performed in this work can be applied to the following problems:

1. *Testing for transmitting case:* Initial testing for transmitting case was performed which showed favorable results. A general formulation for the transmitting case similar to the receiving case needs to be developed.
2. *Generalizing for arbitrary arrays:* The experimental and simulation results have been done only for ULA and UCA. This method needs to be extended for arbitrary arrays where a closed form generalized decoupling matrix can be derived.

3. *Reducing array measurements*: The decoupling matrix is direction dependent therefore applications where DF is required measurements are required for the array. Closed form expressions for array patterns being incorporated in the generalized decoupling matrix maybe one of the methods for reducing the measurements. Another method could be bringing the simulation measurements close to the real-time measurements using AI and analyzing the performance.
4. *Comparing the performance with an RIS-aided communication system*: RIS systems require complex passive array structures for beamforming to increase the gain of the antenna array. From our experimental results, it was observed this can be done digitally without using complex structures therefore an experimental comparison of the two techniques could determine the performance metrics.
5. *Testing on a WiFi router*: The 6<sup>th</sup> generation WiFi routers or WiFi 6 utilize at least 8 antennas in a constricted spacing resulting in strong coupling therefore deteriorating the pattern. Incorporating the algorithm on such routers could be an easy solution for compensating for coupling effects.
6. *Compact radar system*: A portable radar system which is modular based can be easily realized using the SDRs such as ADALM-PLUTO. The main problem are huge antenna array structures where spacing is a constraint. Using this method, a whole new system can be designed which is portable and due to its modular nature can be assembled easily using a plug n play SDR.

Apart from the above mentioned problems, the details provided in this thesis can result in many more applications and development of such systems.

## BIBLIOGRAPHY

- [1] L. Dai, B. Wang, M. Wang, X. Yang, J. Tan, S. Bi, S. Xu, F. Yang, Z. Chen, M. D. Renzo, C. B. Chae, and L. Hanzo, "Reconfigurable Intelligent Surface-Based Wireless Communications: Antenna Design, Prototyping, and Experimental Results," *IEEE Access*, vol. 8, pp. 45 913–45 923, 2020.
- [2] L. Connectivity, "Antenna Considerations for WiFi 6," 2020.
- [3] X. Chen, S. Zhang, and Q. Li, "A Review of Mutual Coupling in MIMO Systems," *IEEE Access*, vol. 6, pp. 24 706–24 719, 2018.
- [4] C. Craeye and D. González-Ovejero, "A Review on Array Mutual Coupling Analysis," *Radio Science*, vol. 46, no. 2, 2011. [Online]. Available: <http://dx.doi.org/10.1029/2010RS004518>
- [5] H. M. Aumann, A. J. Fenn, and F. G. Willwerth, "Phased Array Antenna Calibration and Pattern Prediction using Mutual Coupling Measurements," *IEEE Transactions on Antennas and Propagation*, vol. 37, no. 7, pp. 844–850, 1989.
- [6] H. Wei, D. Wang, H. Zhu, J. Wang, S. Sun, and X. You, "Mutual Coupling Calibration for Multiuser Massive MIMO Systems," *IEEE Transactions on Wireless Communications*, vol. 15, no. 1, pp. 606–619, Jan 2016.
- [7] S. Khan, H. Sajjad, M. K. Ozdemir, and E. Arvas, "Mutual Coupling Compensation in Transmitting Arrays of Thin Wire Antennas," *Appl. Comput. Electromagn. Soc. J. (ACES Journal)*, vol. 33, no. 11, pp. 1182–1189, Nov 2018.
- [8] S. Henault and Y. M. M. Antar, "Comparison of various Mutual Coupling Compensation Methods in Receiving Antenna Arrays," *2009 IEEE Antennas and Propagation Society International Symposium*, pp. 1–4, June 2009.
- [9] I. J. Gupta and A. A. Ksienski, "Effect of Mutual Coupling on the Performance of Adaptive Arrays," *IEEE Trans. Antennas Propag.*, vol. 31, no. 5, pp. 785–791, 1983.
- [10] K. W. Lo and T. B. Vu, "Simple S-parameter Model for Receiving Antenna Array," *Electronics Letters*, vol. 24, pp. 1264–1266, Sep. 1988.
- [11] C. Yeh, M. Leou, and D. R. Ucci, "Bearing Estimations with Mutual Coupling Present," *IEEE Transactions on Antennas and Propagation*, vol. 37, no. 10, pp. 1332–1335, 1989.
- [12] Kun-Chou Lee and Tah-Hsiung Chu, "A Circuit Model for Mutual Coupling Analysis of a Finite Antenna Array," *IEEE Transactions on Electromagnetic Compatibility*, vol. 38, no. 3, pp. 483–489, 1996.
- [13] E. M. Friel and K. M. Pasala, "Effects of Mutual Coupling on the Performance of STAP Antenna Arrays," *IEEE Transactions on Aerospace and Electronic Systems*, vol. 36, no. 2, pp. 518–527, 2000.
- [14] O. E. Allen and W. Wasyliwskyj, "Comparison of Mutual Coupling of Blade Antennas with predictions based on Minimum-Scattering Antenna Theory," *IEEE Transactions on Electromagnetic Compatibility*, vol. 42, no. 4, pp. 326–329, 2000.

- [15] M. C. Leifer, "Mutual Coupling Compensation Accuracy," in *IEEE Antennas and Propagation Society International Symposium, USNC/URSI*, vol. 3, 2001, pp. 804–807 vol.3.
- [16] P. Ioannides and C. A. Balanis, "Mutual Coupling in Adaptive Circular Arrays," in *IEEE Antennas and Propagation Society Symposium, 2004.*, vol. 1, 2004, pp. 403–406 Vol.1.
- [17] S. Durrani and M. E. Bialkowski, "Effect of Mutual Coupling on the Interference Rejection Capabilities of Linear and Circular Arrays in CDMA Systems," *IEEE Transactions on Antennas and Propagation*, vol. 52, no. 4, pp. 1130–1134, 2004.
- [18] Kun-Chou Lee and Tah-Hsiung Chu, "Mutual Coupling Mechanisms within Arrays of Nonlinear Antennas," *IEEE Transactions on Electromagnetic Compatibility*, vol. 47, no. 4, pp. 963–970, 2005.
- [19] H. T. Hui, "Compensating for the Mutual Coupling Effect in Direction Finding based on a New Calculation Method for Mutual Impedance," *IEEE Antennas and Wireless Propagation Letters*, vol. 2, pp. 26–29, 2003.
- [20] Hon Tat Hui, Kam Yuen Chan, and E. K. N. Yung, "Compensating for the Mutual Coupling Effect in a Normal-Mode Helical Antenna Array for Adaptive Nulling," *IEEE Transactions on Vehicular Technology*, vol. 52, no. 4, pp. 743–751, 2003.
- [21] Hon Tat Hui, "A Practical approach to Compensate for the Mutual Coupling Effect in an Adaptive Dipole Array," *IEEE Transactions on Antennas and Propagation*, vol. 52, no. 5, pp. 1262–1269, 2004.
- [22] H. T. Hui, H. P. Low, T. T. Zhang, and Y. L. Lu, "Antenna Designer's Notebook - Receiving Mutual Impedance between two Normal-Mode Helical Antennas (NMHAs)," *IEEE Antennas and Propagation Magazine*, vol. 48, no. 4, pp. 92–96, 2006.
- [23] Tong Zhang, Hon Tat Hui, and Y. L. Lu, "Compensation for the Mutual Coupling Effect in the ESPRIT Direction Finding Algorithm by using a more Effective Method," *IEEE Transactions on Antennas and Propagation*, vol. 53, no. 4, pp. 1552–1555, 2005.
- [24] Hon Tat Hui, "An Effective Compensation Method for the Mutual Coupling Effect in Phased Arrays for Magnetic Resonance Imaging," *IEEE Transactions on Antennas and Propagation*, vol. 53, no. 11, pp. 3576–3583, 2005.
- [25] H. T. Hui, B. K. Li, and S. Crozier, "A New Decoupling Method for Quadrature Coils in Magnetic Resonance Imaging," *IEEE Transactions on Biomedical Engineering*, vol. 53, no. 10, pp. 2114–2116, 2006.
- [26] D. Segovia-Vargas, R. Martín-Cuerdo, and M. Sierra-Pérez, "Mutual Coupling Effects Correction in Microstrip Arrays for Direction-of-Arrival (DOA) Estimation," *IEE Proceedings - Microwaves, Antennas and Propagation*, vol. 149, pp. 113–118(5), April 2002. [Online]. Available: [https://digital-library.theiet.org/content/journals/10.1049/ip-map\\_20020232](https://digital-library.theiet.org/content/journals/10.1049/ip-map_20020232)
- [27] J. W. Wallace and M. A. Jensen, "Mutual Coupling in MIMO Wireless Systems: A Rigorous Network Theory Analysis," *IEEE Transactions on Wireless Communications*, vol. 3, no. 4, pp. 1317–1325, 2004.



- [28] K. M. Pasala and E. M. Friel, "Mutual Coupling Effects and their Reduction in Wideband Direction of Arrival Estimation," *IEEE Transactions on Aerospace and Electronic Systems*, vol. 30, no. 4, pp. 1116–1122, 1994.
- [29] Hao Yuan, K. Hirasawa, and Yimin Zhang, "The Mutual Coupling and Diffraction Effects on the Performance of a CMA Adaptive Array," *IEEE Transactions on Vehicular Technology*, vol. 47, no. 3, pp. 728–736, 1998.
- [30] R. S. Adve and T. K. Sarkar, "Compensation for the Effects of Mutual Coupling on Direct Data Domain Adaptive Algorithms," *IEEE Transactions on Antennas and Propagation*, vol. 48, no. 1, pp. 86–94, 2000.
- [31] C. K. E. Lau, R. S. Adve, and T. K. Sarkar, "Minimum Norm Mutual Coupling Compensation with Applications in Direction of Arrival Estimation," *IEEE Transactions on Antennas and Propagation*, vol. 52, no. 8, pp. 2034–2041, 2004.
- [32] S. Henault and Y. M. M. Antar, "On the Interpolation of Radiation Patterns in the Calibration of Antenna Arrays," in *2011 IEEE International Symposium on Antennas and Propagation (APSURSI)*, 2011.
- [33] S. Henault and Y. M. M. Antar, "Wideband Analysis of Mutual Coupling Compensation Methods," *IEEE International Journal of Antennas and Propagation*, 2011.
- [34] S. Henault, Y. M. M. Antar, S. Rajan, R. Inkol, and S. Wang, "Effects of Mutual Coupling on the Accuracy of Adcock Direction Finding Systems," *IEEE Transactions on Aerospace and Electronic Systems*, vol. 48, no. 4, pp. 2990–3005, Oct 2012.
- [35] S. Henault, S. K. Podilchak, S. M. Mikki, and Y. M. M. Antar, "A Methodology for Mutual Coupling Estimation and Compensation in Antennas," *IEEE Transactions on Antennas and Propagation*, vol. 61, no. 3, pp. 1119–1131, March 2013.
- [36] S. Henault and Y. Antar, "Unifying the Theory of Mutual Coupling Compensation in Antenna Arrays," *IEEE Antennas and Propagation Magazine*, vol. 57, no. 2, pp. 104–122, April 2015.
- [37] H. Steyskal and J. S. Herd, "Mutual Coupling Compensation in Small Array Antennas," *IEEE Transactions on Antennas and Propagation*, vol. 38, no. 12, pp. 1971–1975, 1990.
- [38] P. Darwood, P. Fletcher, and G. Hilton, "Mutual Coupling Compensation in Small Planar Array Antennas," *IEE Proceedings - Microwaves, Antennas and Propagation*, vol. 145, pp. 1–6(5), February 1998.
- [39] Shuguang Chen and R. Iwata, "Mutual Coupling Effects in Microstrip Patch Phased Array Antenna," in *IEEE Antennas and Propagation Society International Symposium, USNC/URSI*, vol. 2, 1998, pp. 1028–1031 vol.2.
- [40] T. Su and H. Ling, "On Modeling Mutual Coupling in Antenna Arrays using the Coupling Matrix," *Microwave and Optical Technology Letters*, vol. 28, no. 4, pp. 231–237, 2001.
- [41] P. Fletcher, M. Dean, and A. Nix, "Mutual Coupling in Multi-Element Array Antennas and its Influence on MIMO Channel Capacity," *Electronics Letters*, vol. 39, pp. 342–344(2), February 2003. [Online]. Available: [https://digital-library.theiet.org/content/journals/10.1049/el\\_20030219](https://digital-library.theiet.org/content/journals/10.1049/el_20030219)

- [42] D. F. Kelley and W. L. Stutzman, "Array Antenna Pattern Modeling Methods that include Mutual Coupling Effects," *IEEE Transactions on Antennas and Propagation*, vol. 41, no. 12, pp. 1625–1632, 1993.
- [43] J. E. Fernandez del Rio, O. M. Conde-Portilla, and M. F. Catedra, "Estimating Azimuth and Elevation Angles when Mutual Coupling is Significant [Direction Finding]," in *IEEE Antennas and Propagation Society International Symposium, USNC/URSI*, vol. 1, 1998, pp. 215–218 vol.1.
- [44] Xin Li and Zai-Ping Nie, "Mutual Coupling Effects on the Performance of MIMO Wireless Channels," *IEEE Antennas and Wireless Propagation Letters*, vol. 3, pp. 344–347, 2004.
- [45] B. Friedlander and A. J. Weiss, "Direction Finding in the presence of Mutual Coupling," *IEEE Transactions on Antennas and Propagation*, vol. 39, no. 3, pp. 273–284, March 1991.
- [46] Kyungjung Kim, T. K. Sarkar, and M. S. Palma, "Adaptive Processing using a Single Snapshot for a Nonuniformly spaced Array in the presence of Mutual Coupling and Near-Field Scatterers," *IEEE Transactions on Antennas and Propagation*, vol. 50, no. 5, pp. 582–590, 2002.
- [47] K. R. Dandekar, Hao Ling, and Guanghan Xu, "Experimental Study of Mutual Coupling Compensation in Smart Antenna Applications," *IEEE Transactions on Wireless Communications*, vol. 1, no. 3, pp. 480–487, 2002.
- [48] Yan Wang and Shanjia Xu, "Mutual Coupling Calibration of DBF Array with Combined Optimization Method," *IEEE Transactions on Antennas and Propagation*, vol. 51, no. 10, pp. 2947–2952, 2003.
- [49] Yongxi Qian, W. R. Deal, N. Kaneda, and T. Itoh, "A Uniplanar Quasi-Yagi antenna with Wide Bandwidth and Low Mutual Coupling Characteristics," in *IEEE Antennas and Propagation Society International Symposium, USNC/URSI*, vol. 2, 1999, pp. 924–927 vol.2.
- [50] J. D. Fredrick, Yuanxun Wang, and T. Itoh, "Smart Antennas based on Spatial Multiplexing of Local Elements (SMILE) for Mutual Coupling reduction," *IEEE Transactions on Antennas and Propagation*, vol. 52, no. 1, pp. 106–114, 2004.
- [51] H. Sajjad, S. Khan, and E. Arvas, "Mutual Coupling reduction in Array elements using EBG structures," in *2017 International Applied Computational Electromagnetics Society Symposium - Italy (ACES)*, 2017, pp. 1–2.
- [52] A. G. Demeryd, "Compensation of Mutual Coupling Effects in Array Antennas," in *IEEE Antennas and Propagation Society International Symposium. 1996 Digest*, vol. 2, July 1996, pp. 1122–1125 vol.2.
- [53] S. Zhang and G. F. Pedersen, "Mutual Coupling Reduction for UWB MIMO Antennas with a Wideband Neutralization Line," *IEEE Antennas and Wireless Propagation Letters*, vol. 15, pp. 166–169, 2016.
- [54] Y. Yu, X. Liu, Z. Gu, and L. Yi, "A Compact Printed Monopole Array with Neutralization Line for UWB Applications," in *2016 IEEE International Symposium on Antennas and Propagation (APSURSI)*, 2016, pp. 1779–1780.

- [55] H. Jiang, L. m. Si, G. Cheng, and X. Lv, "A Wideband Close-spaced 5G MIMO Antenna with Mutual Coupling Reduction Using Combined Decoupling Networks," in *2019 International Conference on Microwave and Millimeter Wave Technology (ICMMT)*, 2019, pp. 1–3.
- [56] M. M. Albannay, J. C. Coetzee, X. Tang, and K. Mouthaan, "Dual-Frequency Decoupling for Two Distinct Antennas," *IEEE Antennas and Wireless Propagation Letters*, vol. 11, pp. 1315–1318, 2012.
- [57] J. Zhu and G. V. Eleftheriades, "A Simple Approach for Reducing Mutual Coupling in Two Closely Spaced Metamaterial-Inspired Monopole Antennas," *IEEE Antennas and Wireless Propagation Letters*, vol. 9, pp. 379–382, 2010.
- [58] H. Lui and H. T. Hui, "Mutual Coupling Compensation of Compact Antenna Array for Direction-of-Arrivals Estimations," in *2010 4th International Conference on Signal Processing and Communication Systems*, 2010, pp. 1–10.
- [59] Y. Yu, H. Lui, C. H. Niow, and H. T. Hui, "Improved DOA Estimations Using the Receiving Mutual Impedances for Mutual Coupling Compensation: An Experimental Study," *IEEE Transactions on Wireless Communications*, vol. 10, no. 7, pp. 2228–2233, 2011.
- [60] H. T. Hui, M. E. Bialkowski, and H. S. Lui, "Mutual Coupling in Antenna Arrays," *International Journal of Antennas and Propagation*, vol. 2010, pp. 1–2, 2010. [Online]. Available: <https://doi.org/10.1155/2010/736701>
- [61] H. Hui, "Improved Mutual Coupling Compensation in Compact Antenna Arrays," *IET Microwaves Antenna and Propagation*, vol. 4, pp. 1506–1516(10), October 2010. [Online]. Available: <https://digital-library.theiet.org/content/journals/10.1049/iet-map.2009.0200>
- [62] Hoi-Shun Lui, H. T. Hui, and Mook Seng Leong, "A Note on the Mutual-Coupling Problems in Transmitting and Receiving Antenna Arrays," *IEEE Antennas and Propagation Magazine*, vol. 51, no. 5, pp. 171–176, 2009.
- [63] C. H. Niow and H. T. Hui, "Improved Noise Modeling with Mutual Coupling in Receiving Antenna Arrays for Direction-of-Arrival Estimation," *IEEE Transactions on Wireless Communications*, vol. 11, no. 4, pp. 1616–1621, April 2012.
- [64] H.-S. Lui and H. T. Hui, "Mutual Coupling Compensation for Direction Finding using Receiving Mutual Impedance," in *2014 International Symposium on Antennas and Propagation (ISAP)*, 2014, pp. 61–62, International Symposium on Antennas and Propagation (ISAP), Kaohsiung, Taiwan, Dec 02-04, 2014.
- [65] H.-S. Lui and H. T. Hui, "Direction-of-Arrival Estimation Measurement using Compact Antenna Arrays under the influence of Mutual Coupling," *IEEE Antennas and Propagation Magazine*, vol. 57, no. 6, pp. 62–68, Dec 2015.
- [66] Y. Yu, C. H. Niow, and H. T. Hui, "Mutual Coupling Compensation for a Compact Array in Direction Finding," ser. Progress in Electromagnetics Research Symposium, 2012, pp. 1338–1340.
- [67] H.-S. Lui and H. T. Hui, "Direction-of-Arrival Estimation of Closely Spaced Emitters Using Compact Arrays," *IEEE International Journal of Antennas and Propagation*, vol. 2013, 2013.

- [68] R. Schmidt, "Multiple Emitter Location and Signal Parameter Estimation," *IEEE Transactions on Antennas and Propagation*, vol. 34, no. 3, pp. 276–280, 1986.
- [69] A. Paulraj, R. Roy, and T. Kailath, "Estimation Of Signal Parameters Via Rotational Invariance Techniques- Esprit," in *Nineteenth Asilomar Conference on Circuits, Systems and Computers, 1985.*, 1985, pp. 83–89.
- [70] J. Capon, "High-resolution frequency-wavenumber Spectrum Analysis," *Proceedings of the IEEE*, vol. 57, no. 8, pp. 1408–1418, 1969.
- [71] H. Cox, R. Zeskind, and M. Owen, "Robust Adaptive Beamforming," *IEEE Transactions on Acoustics, Speech, and Signal Processing*, vol. 35, no. 10, pp. 1365–1376, 1987.
- [72] B. D. Rao and K. V. S. Hari, "Performance analysis of Root-MUSIC," *IEEE Transactions on Acoustics, Speech, and Signal Processing*, vol. 37, no. 12, pp. 1939–1949, 1989.
- [73] H. L. V. Trees, *Optimum Array Processing*. New York: Wiley-Interscience, 2002.
- [74] S. Khan and E. Arvas, "Compensation for the Mutual Coupling in Transmitting Antenna Arrays," in *2016 IEEE Asia-Pacific Conference on Applied Electromagnetics (APACE)*, 2016, pp. 84–88.
- [75] Tie-Jun Shan, M. Wax, and T. Kailath, "On Spatial smoothing for Direction-of-Arrival Estimation of Coherent Signals," *IEEE Transactions on Acoustics, Speech, and Signal Processing*, vol. 33, no. 4, pp. 806–811, 1985.
- [76] B. Friedlander, "On the Accuracy of Array Manifold Models," in *2017 51st Asilomar Conference on Signals, Systems, and Computers*, 2017, pp. 1168–1172.
- [77] B. Friedlander, "Antenna Array Manifolds for High-Resolution Direction Finding," *IEEE Transactions on Signal Processing*, vol. 66, no. 4, pp. 923–932, 2018.
- [78] B. Friedlander, "The Extended Manifold for Antenna Arrays," *IEEE Transactions on Signal Processing*, vol. 68, pp. 493–502, 2020.
- [79] B. Rares, C. Codau, A. Pastrav, T. Palade, H. Hedesiu, B. Balauta, and E. Pus-chita, "Experimental Evaluation of AoA Algorithms using NI USRP Software Defined Radios," in *2018 17th RoEduNet Conference: Networking in Education and Research (RoEduNet)*, 2018, pp. 1–6.
- [80] N. Tayem, "Real Time Implementation for DoA Estimation Methods on NI-PXI Platform," *Progress In Electromagnetics Research B*, vol. 59, pp. 103–121, 2014. [Online]. Available: <https://doi.org/10.2528/pierb14012307>
- [81] S. A. Alawsh, O. A. Al Khazragi, A. H. Muqaibel, and S. N. Al-Ghadhban, "Sparse Direction of Arrival Estimation using Sparse Arrays based on Software-Defined-Radio Platform," in *2017 10th International Conference on Electrical and Electronics Engineering (ELECO)*, 2017, pp. 671–675.
- [82] Z. M. Abu-Shaban, "Localisation Testbed using Software-Defined Radio," Master's thesis, Imperial College, London, 2010.

- [83] J. Pawlan, “An introduction to Software Defined Radio,” in *2015 IEEE International Conference on Microwaves, Communications, Antennas and Electronic Systems (COMCAS)*, Nov 2015, pp. 1–1.
- [84] D. A. Clendenen, “A Software Defined Radio Testbed for Research in Dynamic Spectrum Access,” Master’s thesis, Purdue University, Indiana, USA, 2012.
- [85] T. F. Collins, “Enabling 5g technologies,” Ph.D. dissertation, Worcester Polytechnic Institute, USA, 2017.
- [86] “[https://wiki.analog.com/resources/eval/user-guides/ad-fmcomms2-ebz/iq\\_rotation](https://wiki.analog.com/resources/eval/user-guides/ad-fmcomms2-ebz/iq_rotation).” [Online]. Available: [https://wiki.analog.com/resources/eval/user-guides/ad-fmcomms2-ebz/iq\\_rotation](https://wiki.analog.com/resources/eval/user-guides/ad-fmcomms2-ebz/iq_rotation)
- [87] “<https://wiki.analog.com/resources/eval/user-guides/ad-fmcomms5-ebz/multi-chip-sync>.” [Online]. Available: <https://wiki.analog.com/resources/eval/user-guides/ad-fmcomms5-ebz/multi-chip-sync>
- [88] G. J. Foschini and M. J. Gans, “On Limits of Wireless Communications in a Fading Environment when Using Multiple Antennas,” *Wireless Personal Communications*, vol. 6, no. 3, pp. 311–335, Mar 1998. [Online]. Available: <https://doi.org/10.1023/A:1008889222784>
- [89] M. K. Ozdemir, H. Arslan, and E. Arvas, “Mutual Coupling Effect in Multi-antenna Wireless Communication Systems,” in *GLOBECOM '03. IEEE Global Telecommunications Conference (IEEE Cat. No.03CH37489)*, vol. 2, 2003, pp. 829–833 Vol.2.
- [90] H. Li, G. Zhaozhi, M. Junfei, J. Ze, Li ShuRong, and Z. Zheng, “Analysis of Mutual Coupling Effects on Channel Capacity of MIMO Systems,” in *2008 IEEE International Conference on Networking, Sensing and Control*, 2008, pp. 592–595.
- [91] X. Liu and M. E. Bialkowski, “Effect of Antenna Mutual Coupling on MIMO Channel Estimation and Capacity,” *International Journal of Antennas and Propagation*, vol. 2010, p. 306173, Mar 2010. [Online]. Available: <https://doi.org/10.1155/2010/306173>
- [92] K. Chen and J. Kiang, “Effect of Mutual Coupling on the Channel Capacity of MIMO Systems,” *IEEE Transactions on Vehicular Technology*, vol. 65, no. 1, pp. 398–403, 2016.
- [93] M. Gustafsson, J. Aulin, M. Högberg, M. Alm, and B. Sihlbom, “Impact of Mutual Coupling on Capacity in large MIMO Antenna Arrays,” in *The 8th European Conference on Antennas and Propagation (EuCAP 2014)*, 2014, pp. 2723–2727.
- [94] X. Mei and K. Wu, “How Low Does Mutual Coupling Need to Be for MIMO Antennas,” in *2018 IEEE International Symposium on Antennas and Propagation USNC/URSI National Radio Science Meeting*, 2018, pp. 1579–1580.
- [95] N. W. M. Thet, S. Khan, E. Arvas, and M. K. Özdemir, “Impact of Mutual Coupling on Power-Domain Non-Orthogonal Multiple Access (NOMA),” *IEEE Access*, vol. 8, pp. 188 401–188 414, 2020.
- [96] “IEEE Standard for Information technology–Telecommunications and information exchange between systems Local and metropolitan area networks–Specific

requirements Part 11: Wireless LAN Medium Access Control (MAC) and Physical Layer (PHY) Specifications,” *IEEE Std 802.11-2012 (Revision of IEEE Std 802.11-2007)*, pp. 1–2793, 2012.

- [97] B. Rares, C. Codau, A. Pastrav, T. Palade, H. Hedesiu, B. Balauta, and E. Pus-chita, “Experimental Evaluation of AoA Algorithms using NI USRP Software Defined Radios,” in *2018 17th RoEduNet Conference: Networking in Education and Research (RoEduNet)*, 2018, pp. 1–6.



## **CURRICULUM VITAE**

Name Surname : Sana Khan

### **EDUCATION:**

B.Sc. : 2013, Ghulam Ishaq Khan Institute of Engineering Sciences and Technology (GIKI), Faculty of Engineering Sciences (FES), Lasers and Optoelectronics.

M.Sc. : 2017, Istanbul Medipol University (IMU), Graduate School of Engineering and Natural Sciences, Electric-Electronic and Cyber Systems.

### **PROFESSIONAL EXPERIENCE AND REWARDS:**

- 2017, Graduate Scholarship for PhD, IMU.
- 2015, Graduate Scholarship for MS, IMU.
- 2013, Electronic Engineer, FES, GIKI.
- 2013, Semi-finalist at Siemens Student Award Middle East amongst 78 teams worldwide.
- 2013, Ranked 1<sup>st</sup> in senior design project at Open House Career Fair, GIKI.
- 2013, Ranked 3<sup>rd</sup> in Faculty of Engineering Sciences, GIKI.
- 2009, Listed on the school honour board for securing 1<sup>st</sup> position in High School, GIKI.
- 2007, Listed on the school honour board for securing 1<sup>st</sup> position in Secondary School, GIKI.

### **PUBLICATIONS, PRESENTATIONS, AND PATENTS ON THE THESIS:**

- S. Khan, Hassan Sajjad, M. K. Ozdemir, and E. Arvas, "Mutual Coupling Compensation in Receiving Arrays and Its Implementation on Software Defined Radios," *Applied Computational Electromagnetics Society Journal (Special issue) (ACES)*, vol. 35, no. 11, pp. 1433-1434, November 2020.
- S. Khan, Hassan Sajjad, M. K. Ozdemir, and E. Arvas, "Mutual Coupling Compensation in receiving Antenna Arrays," *Applied Computational Electromagnetics Society Journal (Special issue) (ACES)*, vol. 35, no. 11, pp. 1316-1317, November 2020.

- N. W. M. Thet, S. Khan, E. Arvas and M. K. Özdemir, “Impact of Mutual Coupling on Power-Domain Non-Orthogonal Multiple Access (NOMA),” in *IEEE Access*, vol. 8, pp. 188401-188414, 2020, doi: 10.1109/ACCESS.2020.3030110.

#### **OTHER PUBLICATIONS, PRESENTATIONS, AND PATENTS:**

- S. H. Savci, Hassan Sajjad, S. Khan, and F. Kaburcuk, “A Compact Multi-Band Antenna on Textile for Wearable Body Area Network Devices,” in *Balkan Journal of Electrical and Computer Engineering*, 2021, Accepted.
- S. Khan, Hassan Sajjad, M. K. Ozdemir, and E. Arvas, “Mutual Coupling Compensation in Receiving Arrays and Its Implementation on Software Defined Radios,” *Applied Computational Electromagnetics Society (ACES)*, Monterey, California, USA, July 2020.
- S. Khan, Hassan Sajjad, M. K. Ozdemir, and E. Arvas, “Mutual Coupling Compensation in receiving Antenna Arrays,” *Applied Computational Electromagnetics Society (ACES)*, Monterey, California, USA, July 2020.
- A. Altaf, Hassan Sajjad, S. Khan, and E. Arvas, “Sheath Helix in a Metallic Envelope,” *International Conference on Electrical Engineering and Computer Science (ICECS)*, Sarajevo, Bosnia and Herzegovina, May 2019.
- S. Khan, Hassan Sajjad, M. K. Ozdemir, and E. Arvas, “Mutual Coupling Compensation in Transmitting Arrays of Thin Wire Antennas,” *Applied Computational Electromagnetics Society Journal (ACES)*, vol. 33, no. 11, pp. 1182-1189, November 2018.
- Hassan Sajjad, S. Khan, A. Altaf, L. Jan, “A Compact Hairpin Filter With Stepped Hairpin Defected Ground Structure,” *2018 International Multi-topic Conference (INMIC)*, Karachi, Pakistan, 2018.
- A. Altaf, Hassan Sajjad, S. Khan, M. Munir, “ISM Band 1:16 Wilkinson Power Divider,” *2018 International Multi-topic Conference (INMIC)*, Karachi, Pakistan, 2018.
- Hassan Sajjad, S. Khan, A. Altaf, S. Arvas, T. Baykas, M. K. Ozdemir and E. Arvas, “Direction Finding Using  $2 \times 2$  Horn Antenna Monopulse System,” *Computational Methods and Telecommunication in Electrical Engineering and Finance (CMTEEF)*, Sarajevo, Bosnia and Herzegovina, May 2018.
- Hassan Sajjad, W. Sethi, L. Jan, and S. Khan, “Compact dual-band implantable antenna for E-health monitoring,” *2017 International Symposium on Wireless Systems and Networks (ISWSN)*, Lahore, Pakistan, 2017, pp. 1-4, 2017.
- Hassan Sajjad, S. Khan, and E. Arvas, “Mutual coupling reduction in array elements using EBG structures,” *2017 International Applied Computational Electromagnetics Society Symposium (ACES)*, Florence, Italy, pp. 1-2, 2017.
- S. Khan and E. Arvas, “Compensation for the mutual coupling in transmitting antenna arrays,” *2016 IEEE Asia-Pacific Conference on Applied Electromagnetics (APACE)*, 2016, pp. 84-88, doi: 10.1109/APACE.2016.7916481.



- S. Arvas, Hassan Sajjad, A. Altaf, S. Khan, and E. Arvas, “Microwave heating of heavy oil and Bitumen,” *2016 IEEE Asia-Pacific Conference on Applied Electromagnetics (APACE)*, Langkawi, Malaysia, pp. 319-322, 2016.



# MUTUAL COUPLING COMPENSATION IN ARRAYS AND ITS IMPLEMENTATION ON SOFTWARE DEFINED RADIOS

## ORIGINALITY REPORT

14%

SIMILARITY INDEX

11%

INTERNET SOURCES

6%

PUBLICATIONS

2%

STUDENT PAPERS

## PRIMARY SOURCES

1	<a href="http://www.ece.nus.edu.sg">www.ece.nus.edu.sg</a> Internet Source	2%
2	<a href="http://fr.mathworks.com">fr.mathworks.com</a> Internet Source	1%
3	Hoi-Shun Lui. "Experimental study of mutual coupling compensation in direction finding using a compact antenna array", 2010 Asia-Pacific International Symposium on Electromagnetic Compatibility, 04/2010 Publication	1%
4	<a href="http://decibel.ni.com">decibel.ni.com</a> Internet Source	<1%
5	<a href="http://www.hindawi.com">www.hindawi.com</a> Internet Source	<1%
6	<a href="http://hdl.handle.net">hdl.handle.net</a> Internet Source	<1%
7	<a href="http://etd.lib.metu.edu.tr">etd.lib.metu.edu.tr</a> Internet Source	<1%